COMPOSITION AND PARTICLE-SIZE EVOLUTION OF KENTUCKY #9

Thomas Erickson, Christopher Zygarlicke, Murali Ramanathan, and Bruce Folkedahl
University of North Dakota Energy and Environmental Research Center
Box 8213, University Station
Grand Forks, ND 58202

INTRODUCTION

The size and composition of ash resulting during coal combustion involves both chemical and physical processes. Ash particles formed during coal combustion depend largely upon the association of the inorganic species in the coal. In order to accurately model the ash formation processes, detailed information on the distribution of minerals with respect to coal particles is essential.

The combustion of Kentucky #9 coal was analyzed through a three-step approach to track particle-size and compositional evolution. First, the coal was characterized with advanced analytical techniques to determine the original size and type of the minerals present. Second, the coal was combusted under carefully controlled conditions to produce fly ash. The fly ash was characterized with analytical techniques similar to those used with the coal. Third, two separate predictive methods were produced from comparison of the two data sets as well as previous investigations (1,2).

EXPERIMENTAL APPROACH

A utility-sized (70% -200 mesh) sample of Kentucky #9 coal was received from the coal sample bank at Foster Wheeler. The coal was characterized by computer-controlled scanning electron microscopy (CCSEM), x-ray fluorescence (XRF), proximate-ultimate analysis, and automated- and manual-imaging techniques in conjunction with the CCSEM technique. The above analysis combined to provide a wide base of knowledge on the coal in terms of the minerals present, their size distributions, and the bulk chemistry of the coal.

The coal was combusted in a vertically oriented laminar flow furnace (drop-tube furnace) at 1500°C, for approximately 2.5 seconds in an environment to simulate the fouling conditions present during combustion in a pulverized coal-fired furnace. The ash was immediately cooled and quenched with nitrogen upon leaving the furnace. The resultant ash was analyzed with CCSEM. The information obtained from the ash is particle size and particle composition.

COAL AND ASH CHARACTERIZATION

The CCSEM data for both the coal and the formed fly ash were analyzed with the use of a classification method, designed by UNDEERC, specifically for CCSEM data. The fly ash data was first corrected for the spherical orientation of the particles. Figure 1 is a SEM photograph of the fly ash produced and shows that a spherical (circular) orientation of the particles is predominant. When analyzing the size of spheres with a random, cross-sectional, two-dimensional technique, the average measured diameter is lower than the actual average diameter (3). The following equation was applied to correct for this underestimation:

$$D_A = D_M*4/Pi \qquad \text{[Eq. 1]}$$

where D_A is the actual diameter and D_M is the measured diameter. Table 1 shows the compositional classifications as determined from the CCSEM analysis for both the coal and fly ash. It is noted that the classification of CCSEM data is not specific to crystalline types; it classifies by composition only. Figure 2 shows the

particle-size distribution for the coal and fly ash (corrected for spherical orientation) as determined by CCSEM. The reason for the fly ash distribution being smaller than the mineral size distribution can only be from the fragmentation of mineral particles during combustion. Since pyrite is the only major mineral classified to undergo fragmentation under combustion conditions, and it comprises a substantial amount of the minerals, an "iron-free basis" may give a better understanding of the transformations that occur. Figure 3 shows both the mineral and fly ash distributions on an "iron-free basis." The mineral distribution is now smaller than the fly ash which shows evidence of coalescence of minerals during combustion. Table 2 shows the new classification of the two samples on an "iron-free basis."

The coal was also investigated for the inclusion of minerals inside coal particles (inherent) and the presence of minerals not associated inside a carbon structure (extraneous) (4). Figure 4 shows an SEM photograph of a cross section of the coal mounted in epoxy. The minerals (brighter areas) can be seen to exist in both the coal (grey areas) and epoxy (dark areas). Every particle classified with the CCSEM routine (>2000 particles) was also classified as inherent or extraneous.

PREDICTIVE METHOD 1

Method 1 uses the coal CCSEM results on an "iron-free basis" to predict fly ash formation on an "iron-free basis." The iron-containing species are omitted with the assumption that they lead primarily to the formation of iron oxide and small amounts of iron rich aluminosilicates and silicates. The two categories used in Method 1 are inherent and extraneous particles. The extraneous particles are assumed to not interact with other extraneous or inherent particles during the combustion process. The inherent particles are assumed to randomly coalesce during the process. A random number (with upper and lower limits) of the inherent particles is chosen at random and coalesced to form a single fly ash particle. The sizes and compositions of the coalescing particles are used to generate the size and composition of the resulting fly ash particles. 3000 particles are created from the inherent data and processed through the CCSEM classification program. The inherent and extraneous compositions are combined to form the resultant data. Table 3 shows the composition of the particles produced by Method 1, along with the experimental fly ash composition. Both compositions are similar with differences noted with aluminosilicate particles. A likely explanation for the difference is that the CCSEM classification program incorporates a large number of aluminosilicate classifications and thus must draw fine lines from classification to classification. The total aluminosilicates found for Method 1 and experimental ash are 54.8 and 55.3, respectively, which supports the above statement. The particle-size distributions for both the experimental data and predictive Method 1 are shown in Figure 5. The distributions are very close, and a slight modification in coalescence extremes would be expected to fit better with little change in composition.

PREDICTIVE METHOD 2

Method 2 does not involve the "iron-free basis" of the previous method. The entire data set is used, and predictions are on a total basis. The role in inherent and extraneous particles are similar to Method 1. The inherent pyrite is allowed to coalesce with a small loss in volume due to the release of sulfur during combustion. The extraneous pyrite is assumed to produce iron oxide in a reduced amount also due to the release of sodium. Table 4 shows the compositions predicted, along with those of the fly ash. The iron oxide composition appears to be very high and is believed to be a result of sampling error prior to CCSEM analysis. The pyrite analyzed here is almost double that of a previous reporting. By reducing the pyrite (→ iron oxide) and renormalizing the data, a much closer composition is achieved and is also shown in Table 4.

159

CONCLUSIONS

Method 1 shows very good agreement with the experimental fly ash data. The use of an iron-free basis allows the study of direct coalescence of minerals in the absence of mineral fragmentation. A proper algorithm for iron removal is essential, and previous results used assumptions that may induce limited amounts of error.

Method 2, with the correction in pyrite to fit previously reported values, also looks very good. At the current time, the investigation of pyrite fragmentation is crucial in determining the total size distribution of the ash; thus it has not been addressed here.

CCSEM analysis coupled together with inherent and extraneous classifications are showing great promise for predicting fly ash formation from coal data. The next step is a coal particle-by-coal particle analysis technique.

REFERENCES

1. Zygarlicke, C.J.; Toman, D.L.; Benson, S.A. "Trends in the Evolution of Fly Ash Size During Combustion," _Prepr. Pap.--Am. Chem. Soc., Div. Fuel Chem._ 1990, 35(3), 621-636.

2. Zygarlicke, C.J.; Steadman, E.N.; Benson, S.A. "Studies of Transformation of Inorganic Constituents in a Texas Legnite during Combustion," _Progress in Energy and Combustion. Science Review_, 1990, 16, 195-204.

3. Zygarlicke, C.J.; Toman, D.L.; Steadman, E.N.; Brekke, D.W.; Erickson, T.A. "Combustion Inorganic Transformation," Quarterly Technical Progress Report to United States Department of Energy on Contract No. DE-FC21-86MC10637; University of North Dakota Energy and Environmental Research Center, Grand Forks, ND, 1990.

4. Zygarlicke, C.J.; Steadmen, E.N. "Advanced SEM Techniques to Characterize Coal Minerals," _Scanning Microscopy_ 1990, 4(3), 579-590.

TABLE 1

CCSEM RESULTS FOR THE MAJOR COMPONENTS OF KENTUCKY #9 COAL AND FLY ASH

Classifications	Coal	Fouling Ash
Quartz	9.5	8.4
Iron Oxide	0.2	11.2
Calcite	1.0	2.2
Kaolinite	4.3	2.5
Montmorillonite	3.8	6.3
K-Aluminosilicate	13.6	15.2
Fe-Aluminosilicate	0.1	9.9
Aluminosilicate	0.5	6.7
Mixed Aluminosilicate	0.2	5.0
Pyrite	44.7	1.5
Si-Rich	2.4	8.7
Unknowns	16.2	17.5

TABLE 2

IRON-FREE MAJOR COMPONENTS OF KENTUCKY #9 COAL AND FLY ASH

Classifications	Coal	Fouling Ash
Quartz	17.70	10.9
Calcite	3.00	2.9
Kaolinite	8.00	6.0
Montmorillonite	10.50	14.4
K-Aluminosilicate	36.00	22.5
Aluminosilicate	2.45	10.7
Mixed Aluminosilicate	0.70	1.7
Si-Rich	6.20	11.9
Unknowns	8.30	9.7

TABLE 3

COMPARISON OF PREDICTIVE METHOD 1 AND EXPERIMENTAL FLY ASH DATA
ON AN IRON-FREE BASIS

Classifications	Method 1	Fouling Ash
Quartz	12.9	10.9
Calcite	2.7	2.9
Kaolinite	5.6	6.0
Montmorillonite	10.8	14.4
K-Aluminosilicate	33.9	22.5
Aluminosilicate	4.0	10.7
Mixed Aluminosilicate	0.5	1.7
Gypsum	2.3	1.9
Apatite	2.6	0.5
Si-Rich	8.2	11.9
Unknown	12.8	9.7

TABLE 4

COMPARISON OF PREDICTIVE METHOD 2 AND EXPERIMENTAL FLY ASH COMPOSITION
(A modification of Method 2 is also shown due to the inconsistency of pyrite.)

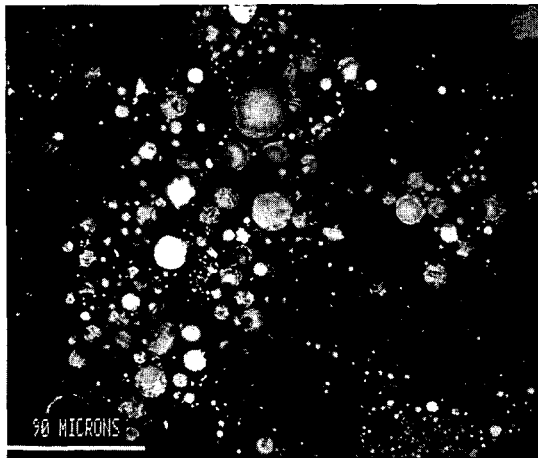| Classifications	Method 2	Fouling Ash	Modified
Quartz	8.0	8.4	9.3
Iron Oxide	30.0	11.2	15.6
Calcite	1.6	2.2	1.9
Kaolinite	2.6	2.5	3.0
Montmorillonite	4.4	6.3	5.1
K-Aluminosilicate	19.3	15.2	22.5
Fe-Aluminosilicate	4.7	9.9	5.4
Aluminosilicate	2.1	6.7	2.4
Mixed Aluminosilicate	0.4	5.0	0.4
Gypsum	1.4	1.5	1.6
Apatite	1.6	0.4	1.9
Si-Rich	4.7	8.7	5.5
Unknowns	17.7	17.5	19.9

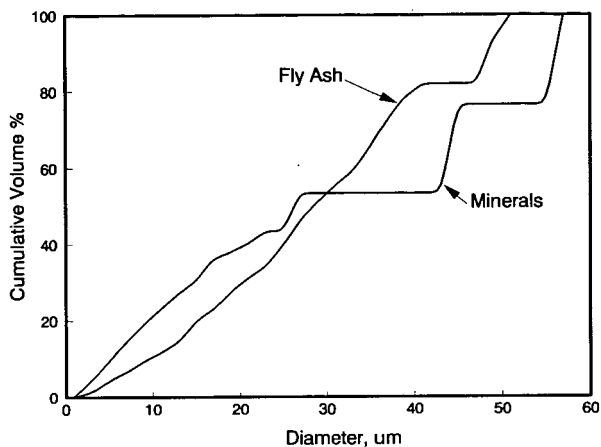Figure 1. SEM photograph of Kentucky #9 fly ash formed under fouling conditions at 1500°C for 2.5 seconds.

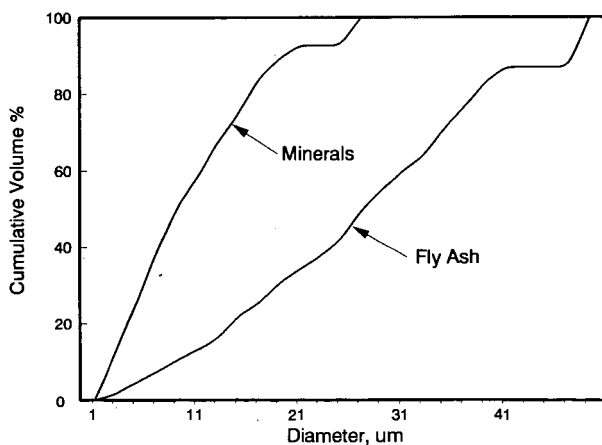Figure 2. CCSEM particle-size distributions for Kentucky #9 coal and fly ash.

Figure 3. Iron-free particle-size distribution for Kentucky #9 coal and fly ash.
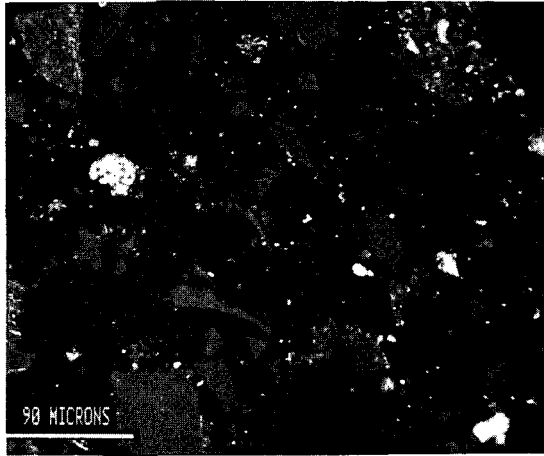
Figure 4. SEM (BEI) photograph of Kentucky #9 coal mounted in epoxy. Bright area-minerals, grey area - coal, dark area - epoxy.
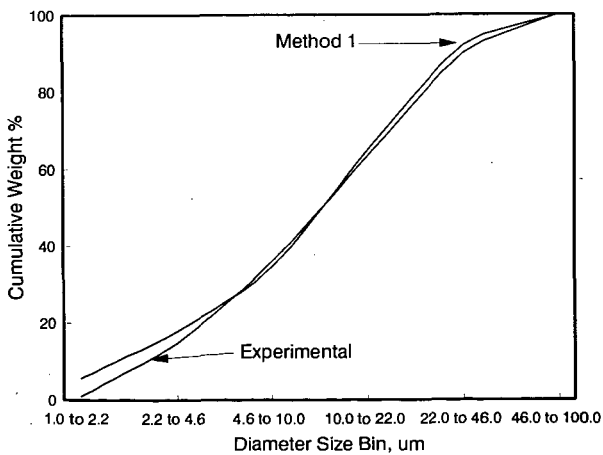

Figure 5. Particle-size distributions of experimental fly ash and predictive Method I particles on an iron-free basis.

GRAPHICAL REPRESENTATION OF CCSEM DATA FOR COAL MINERALS AND ASH PARTICLES.

Naresh Shah, G.P. Huffman, F.E. Huggins, Anup Shah
233 Mining and Mineral Resources Building
University of Kentucky, Lexington, KY 40506-0107.
W.J. Mershon , G. Casuccio
R.J. Lee Group, Inc.,
350 Hochberg Road, Monroeville, PA 15146.

Introduction:

Since its inception, Computer Controlled Scanning Electron Microscopy (CCSEM) has proved to be a powerful tool for materials science (1-4). In coal research, CCSEM has been used to obtain important physical mineralogical information about coal (5,6). Several factors make CCSEM the method of choice in this area. Bulk mineralogical and chemical methods are time consuming and limited. Furthermore, such methods are incapable of providing physical characteristics like size and shape of coal mineral particles which clearly play important roles in ash formation during combustion (7) and catalysis during liquefaction (8). Besides coal mineral analysis, CCSEM has been used to identify and characterize ash particles to gain insight into deposition and fouling characteristics of coals during the coal combustion phenomena. Recent research emphasis in the CCSEM field has been on investigating mineral-maceral associations (9).

CCSEM is basically a statistical analysis method. Thousands of individual particles are analyzed in the course of a single sample analysis and for every one of them chemical composition from X-ray EDS spectra and dimensional (size) parameters from back scattered electron imaging are obtained. These data are then statistically analyzed to infer mineralogical characteristics of the sample. Traditionally, all the statistical data thus obtained is listed in a tabular format. Although such information is very useful and can not be easily obtained by other means, some rather important information and relationships may be obscured in such typical statistical analysis. Graphical representation of CCSEM data provides the means for revealing this hidden complementary information. Though such information may not be easily quantifiable, it can provide the user with a completely different perspective about the sample. Graphical representation of CCSEM data often unveils trends and correlations in a very user friendly way and the information, which usually is difficult to extract from tables, can be easily displayed and understood. In this paper, we show some of the graphical representations our group has developed and used to analyze various problems in coal research.

Size distribution:

Determination of particle size distributions is one of the oldest applications of CCSEM. Bar and line charts make data presentation very user friendly. Stacked charts help in understanding size distribution trends of different minerals in the same sample or the same mineral in different samples. Commercial CCSEM instruments invariably provide software to display such trends. Figure 1 shows pyrite size distributions for some of the Argonne premium sample bank coals (6).

Binary diagrams:

To study the interaction between any two components, we have developed a binary diagram representation. Two component CCSEM data are plotted as a number or volume percentage frequency as a function of concentration of one of the components. Since the data is normalized to 100 percent to represent only two components, it also displays the same information with decreasing concentration of the second component. Figure 2 shows Fe-S binary diagrams for the Argonne Beulah coal. Figure 2a is a plot of number percentage distribution as a function of Fe and S concentrations for all the particles with more than 80% combined counts for Fe and S from EDS spectrum. Since the particles can have different sizes, number percentage representation alone is not quite adequate. We have also incorporated the size information in binary diagram (Figure 2b). If we know density as a function of the concentration, such plots can be easily converted to actual weight distribution.

In some cases, representing just two components is not sufficient and interactions of a single component with a combination of phases or a mineral with several elements (e.g. illite, kaolinite) is important. To display such interactions graphically, we have modified binary diagrams so that one of the ends can be a combination of components. Figure 3 shows several such diagrams for a series of Beulah ash samples collected by University of Arizona's combustor on a size segregating impactors. Graphical representation of such data clearly shows the trends in reaction mechanism. With increasing impactor number (smaller size ash particles), there is more interaction between the aluminosilicate phase with CaO forming a glassy phase.

Ternary diagram:

Pseudobinary diagrams like the one mentioned above (where two components are lumped together), do not provide the interactions between all the components in the ash chemistry. A true ternary diagram, as shown in Figure 4, displays individual particles with sum of x-ray counts for the three components > 80%. Figure 4 shows the same sample as in Figure 3a. Using such a ternary diagram representation, we were able to confirm the presence of a nepheline (NaAlSiO4) phase in ashes of low rank coals with large alkali content. Such a phase can play an important role in the fouling and deposition characteristics of the coal during combustion (10).

As a logical extension to ternary diagrams, we can also draw pseudoternary and higher order diagrams in one of two ways. Just like pseudobinary diagrams, we can represent several phases lumped together on one of the vertices of the ternary diagram. Such alumina-silica-base ternary diagrams, where base is a combination of several basic elements (viz. Na, Mg, K, Fe etc.) have been traditionally used by refractory engineers (11). We are currently working on extending such diagrams to include melting point and viscosity information for the ash particles. Such information should provide further insight into stickiness of the ash particles and thereby the fouling and deposition characteristics of such ashes. Alternatively, we can use a color display to represent a fourth dimension in the ternary diagrams. By assigning different colors or different symbols to different concentrations we can display the concentration of the fourth phase on the ternary diagram by different colors (or symbols).

To make this tool more user friendly, we have developed an interactive computer program. In this program, the user can display data in any combinations of components at the three vertices. The user can also select to display a fourth component by different

color or a combination of up to five components on one of the vertices. Using a mouse, the user can further select a subset of the data displayed by positioning a smaller variable size triangle on this ternary diagram. The size distribution information of the interactively selected data subset can then be displayed.

One of the major drawbacks of such a ternary diagram is its inability to show number distribution within the ternary diagram. If two particles have the same composition, they overlap giving only one point on the ternary diagram which can be quite misleading. To overcome this problem, we have added the fourth dimension in the ternary diagram by displaying it in a perspective view. Figure 5 is a number density distribution of Ca-Si-Al ternary diagram for Beulah ash collected on an impactor filter (#1) of University of Arizona combustor (Note the correspondence to Figures 3a and 4). As is clearly evident, the points at both the Ca and Si vertices on the ternary diagram actually represent a large number of particles. Such concentration information is not readily available on the simple ternary diagrams.

Often the physical size information provided by CCSEM is not enough as such information does not reveal anything about the morphology or the association of the particles. To resolve this problem, we have improved CCSEM data acquisition program by including real-time microimaging (12). Once the particle is identified and its x-ray spectrum is obtained, the SEM beam is controlled by the computer to raster the area bounded by a minimum rectangle totally surrounding the particle. The video image of the particle is then captured and stored on the computer with the EDS spectrum as well as the standard physical dimensions and X-ray counts. Since the raster is narrowed down from the entire frame to just the particle dimensions, we can also get a virtual magnification of the particle. These video images can be called up by a mouse driven selection of the particles on a ternary diagram. Figure 6 shows such a digitally stored backscattered electron image of a single coal particle sitting on a beryllium substrate. An experienced user can then deduce something about the morphology and juxtaposition of these particles. We are using such digital images to investigate mineral-maceral association.

Conclusions:

The amount of information generated by CCSEM is difficult to assimilate just by tabular presentations and some important trends have been obscured in conventional analysis. We are developing graphical tools to represent the standard information in a more friendly representation as well as to depict information previously hidden. Further progress in such CCSEM analysis will be carried out by including n-dimensional analyses and video image processing.

REFERENCES

1. R.J. Lee, F.E. Huggins, G.P. Huffman, Scanning Electron Microscopy, 1, (1978), 561-568.
2. F.E. Huggins, D.A. Kosmack, G.P. Huffman, R.J. Lee, Scanning Electron Microscopy, 1, (1980), 531-540.
3. R.J. Lee, J.F. Kelly, Scanning Electron Microscopy, 1, (1980), 303-310.
4. G.P. Huffman, F.E. Huggins, R.W. Shoenberger, J.S. Walker, F.W. Lytle, R.B. Greegor, Fuel, 65, (1986), 621-632.

5. W.E. Straszheim, J.G. Yousling, R. Markuszewski, in Mineral Matter and Ash in Coal (Ed.: K. Vorres), American Chemical Society, (1986), 449-461.
6. N. Shah, R.A. Keogh, F.E. Huggins, G.P. Huffman, A. Shah, B. Ganguly, S. Mitra, ACS Div. of Fuel Chem. Preprints, 35(3), (1990), 784-792.
7. G.P. Huffman, F.E. Huggins, N. Shah, A. Shah, Prog. Energy Combust. Sci., 16, (1990), 243-251.
8. F.V. Stohl, ACS Div. of Fuel Preprints, 34(3), 1989, 814-818.
9. W.E. Straszheim, R. Markuszewski, Energy & Fuels, 4, (1990), 748-754.
10. J. J. Helble, S. Srinivasachar, A. A. Boni, S. G. Kang, A. F. Sarofim, J. M. Beer, N. Gallagher, L. Bool, T. W. Peterson, J. O. L. Wendt, N. Shah, F. E. Huggins, and G. P. Huffman, Proc. Sixth Ann. Pitt. Coal Conf., 1, (1989), 81-89.
11. "Phase Diagrams for Ceramist", Volumes 1-5, American Ceramic Society, (1964).
12. B.C. Henderson, I.M. Stewart, G.S. Casuccio, American Lab., (Nov. 1989).
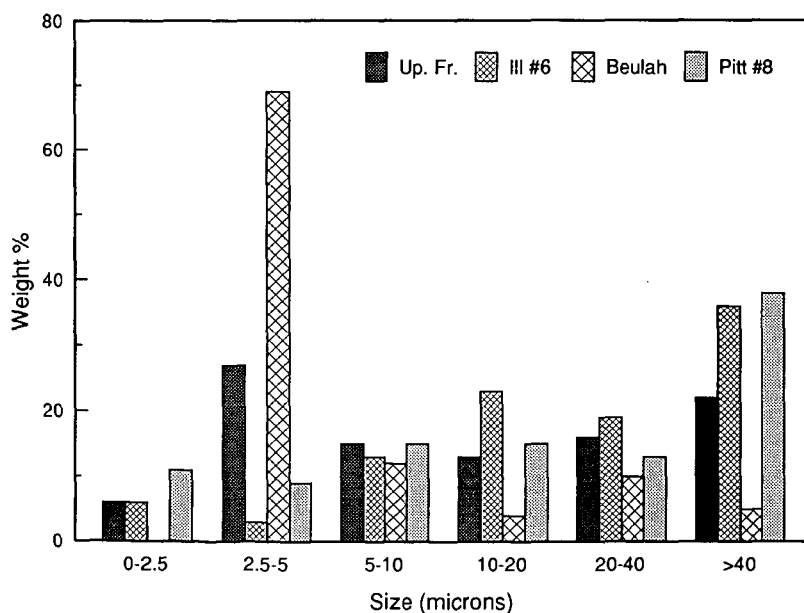
Fig. 1. Example of size distribution obtained by CCSEM for pyrite in several Argonne coals.
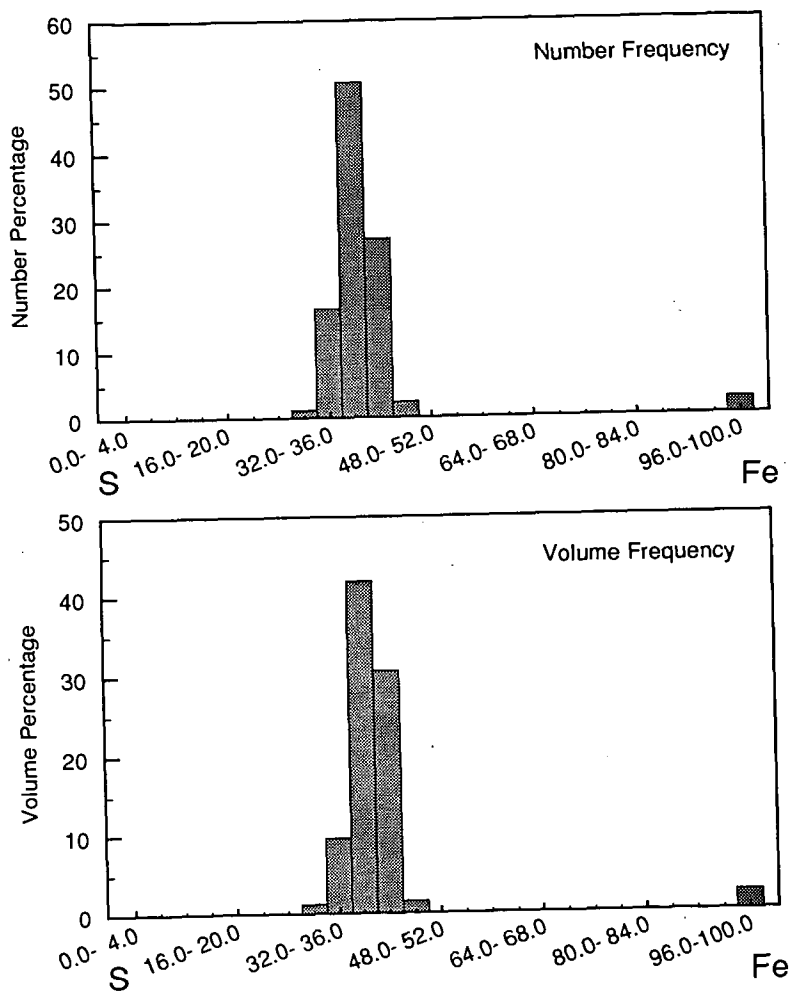
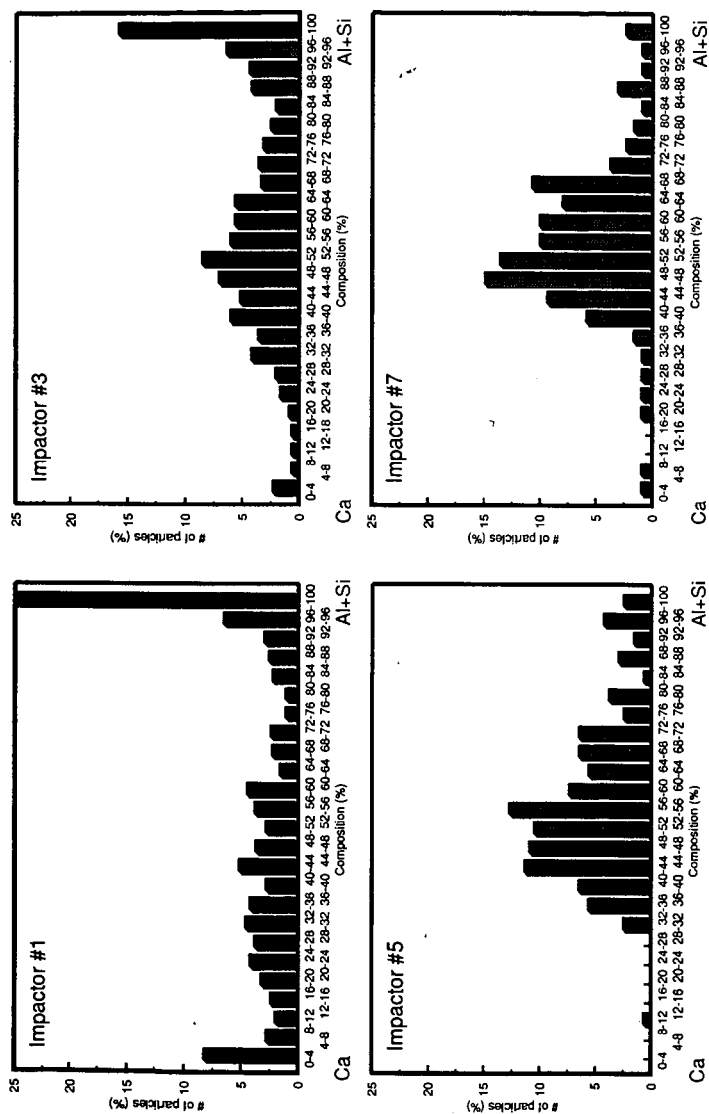Fig. 2. Examples of Fe-S binary composition diagrams for Beulah coal.

Fig. 3. Ca-Al+Si pseudo binary diagram for Beulah ash collected on size segregating impactor filters. Note the decrease in number of pure Ca and Al+Si particles and increase in glassy Ca+Al+Si mixture particles with increasing impactor number (decreasing size).
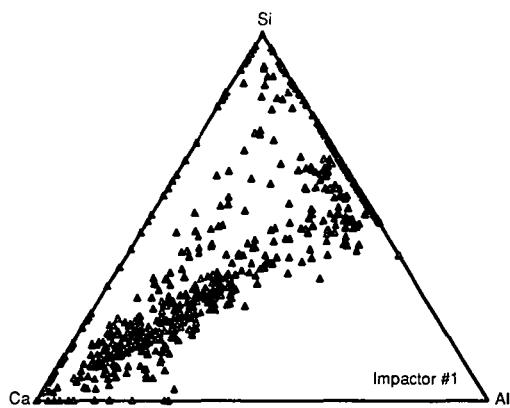
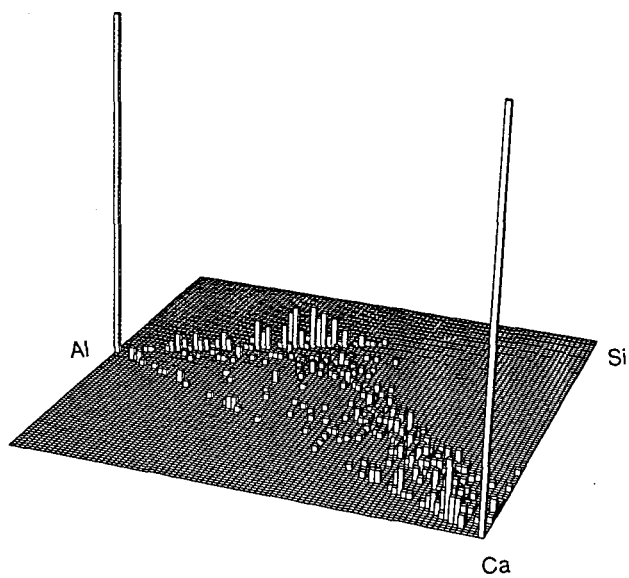Fig. 4. Ca-Al-Si ternary diagram for Beulah ash

Fig. 5. Ca-Al-Si ternary diagram for Beulah ash showing number frequency.

Fig. 6. Digitally stored backscattered electron image of a coal particle on a beryllium substrate. Note a bright mineral particle included within the dark coal matrix.

THE BEHAVIOR OF CLAY MINERALS UNDER COMBUSTION CONDITIONS

J.J. Helble, S. Srinivasachar, and A.A. Boni
PSI Technology Company
20 New England Business Center
Andover MA 01810

ABSTRACT

The mineral matter in pulverized coal contains a significant amount of clays such as kaolinite, illite, montmorillonite, and other aluminosilicates. During combustion, these minerals often melt and coalesce to form larger ash particles which, if their composition and viscosity are in the appropriate range, may stick to wall surfaces upon impact, leading to deposition. To assess the importance of these transformations in determining ash particle stickiness, combustion and deposit initiation experiments were conducted with montmorillonite, two forms of kaolinite, and several U.S. coals. For the montmorillonite, which contained calcium, magnesium, and iron as modifier ions, vitrification was evident upon exposure to 1500°C oxidizing atmospheres. For the kaolinites - essentially pure aluminosilicates - however, little morphological change was noted. As a result of the difference in modifier ions concentrations, the montmorillonite produced lower viscosity "stickier" particles more prone to adhere to tube surfaces. A comparison of these results with those obtained in a pulverized coal combustion study displayed similar trends. During combustion, if coalescence between clay minerals and dispersed modifier ions such as calcium occurred, the resulting ash particles readily adhered to high temperature tube surfaces. In the absence of modifier species coalescence, reduced values of ash stickiness were observed.

BACKGROUND

To properly select coals for a particular boiler, a reliable prediction of the extent of deposition is clearly desirable. Historically, many empirical indices have been employed for this purpose, but these are only reliable for a limited range of fuels under certain well-defined conditions (1,2). Much of the uncertainty associated with these indices stems from their use of *bulk* ash chemistry to describe processes which are initiated by *individual* ash particles. Fundamental laboratory studies have presented convincing evidence for the need to identify individual ash particle properties and determine how these are derived from the parent coal's mineralogy in addressing deposit initiation and growth (3,4). Although much can learned from studies conducted with pulverized coals, the importance of individual mineral and ash species may be lost in such a complex system. For this reason, studies with individual minerals have been conducted to isolate their transformations in a combustion environment, and to determine whether the resulting ash particles may contribute to inertial deposition. In previous efforts, the role of pyrite and illite have been explored (5,6) and compared to results obtained with synthetic glass particles where viscosity was identified as a key parameter in

deposit initiation. Here we extend our study to two commonly encountered clays - kaolinite and montmorillonite - and explore their role in deposit initiation.

EXPERIMENTAL APPROACH
Equipment
All experiments were conducted in an externally heated laminar flow drop tube furnace, described in detail elsewhere (5). In brief, particles were injected at the top of the reactor into premixed, preheated gases containing 0 - 3 percent O_2 in N_2. Temperatures in the reaction zone were held constant during an individual experiment in the range 1000 to 1500°C. At the exit of the reactor, particles were either (a) sampled isokinetically via a water-cooled nitrogen-quenched collection probe and deposited in a filter for subsequent analysis, or (b) inertially impacted on a deposit collection probe. In the deposit collection probe, particles accelerated through a ceramic converging section to impact uncooled 1.25-3.2 mm diameter mullite tubes oriented perpendicular to the flow. Particles which were sufficiently deformable - "sticky" - adhered to the substrate. Morphological examination of the particles was subsequently conducted by scanning electron microscopy (SEM) on an Amray Model 1820 SEM. Chemical analysis of individual particle and deposit samples was by energy-dispersive x-ray analysis (EDAX).

Sample Selection
Kaolinite and montmorillonite clay samples were obtained from the Source Clays Depository at the University of Missouri - Columbia. Samples were mined from several well-characterized locations, steam dried, pulverized in a hammer mill, remixed, and then riffled prior to shipping. No additives were used in the preparation of these clays. The well-crystallized kaolinite was taken from Washington County Georgia; the poorly crystallized kaolinite from Warren County, Georgia; and the montmorillonite, from Apache County, Arizona. Detailed analyses of these samples have been collected and published in reference (7); chemical composition analysis of each sample taken from (7) is presented in Table I (weight loss on heating is the additional term which will sum the compositions to 100%).

The San Miguel lignite presented for comparison has been discussed in detail elsewhere (3). High clay contents in the parent coal made it an ideal choice for comparison with the clays of this study. Mineralogy of the high-ash San Miguel (51% ash on a dry basis), obtained by computer-controlled SEM at the University of Kentucky, was dominated by zeolite silicates (64 weight percent of the minerals), with significant quantities of montmorillonite (16%) and quartz (12%) also present. Kaolinite levels were only 2% in this lignite, which is lower than the 6-20% levels often encountered in U.S. coals. Note that the coal sample was utilized in an as-received form, with 70% < 75 μm in size. Clay samples were dry-sieved to 38/53 μm prior to testing.

RESULTS AND DISCUSSION
Experiments were first conducted with the well-crystallized kaolinite (K-WC) to determine whether melting or vitrification occurred during combustion processing.

In Figure 1, an SEM micrograph shows typical large kaolinite crystals surrounded by a fairly high concentration of submicron-sized fine particulate. The chemical composition of the larger particles was typically 42-44% Al_2O_3, with the balance silica. Little was noted in the way of modifier ions in the untreated K-WC particles examined. Poorly crystallized kaolinite samples (K-PC) also contained a large number of fine particles in the feed material. Silica-to-alumina ratios for the individual K-PC particles examined were comparable to those observed for the K-WC sample. In contrast to the well-crystallized sample, however, low levels of titania (1-2%) were frequently observed. Silica-rich particles containing nominal 5% potassium (as oxide) were also observed as impurities in the K-PC sample.

Subsequent to reaction in 3% oxygen at 1500°C for 2.9 seconds, little change was noted in either the K-WC or the K-PC samples as shown in Figure 2. In the well-crystallized sample, titania levels of 1-2% were occasionally noted, with no apparent change in the silica-to-alumina ratio observed. For the K-PC sample, some coalescence of the submicron fines is evident upon close examination of the micrograph (Fig. 2b). The chemical composition of these particles, as determined by SEM-EDAX, was comparable to that of the parent K-PC particles. Titania was again consistently observed as an impurity at the 2-6 percent level (oxide, by weight). Iron oxide levels of ≤ 2 weight percent were noted in several particles.

Examination of the third clay in this study - montmorillonite - yielded strikingly different results. Initially the particles were similar to the raw kaolinite in that they were of angular shape as seen in Figure 3. Silica-to-alumina ratios in these particles were approximately 3.5/1, with 10% of the particle composed of the modifier ions magnesium, calcium, and iron; most particles sampled were similar in composition to the bulk composition reported in Table I. Subsequent to processing at 1500°C for one second, however, vitrification is apparent in several of the particles seen in Figure 4a. After complete processing at 1500°C for 2.9 seconds (similar to what minerals might encounter in a boiler environment), nearly complete melting was apparent (Fig. 4b).

Because of the high modifier ion content of the montmorillonite, it was expected to produce sticky ash particles prone to deposit over a fairly wide range of conditions. In contrast to this, little deposition was expected from either the K-PC or the K-WC samples. To test this, deposition experiments were conducted with all three samples at deposit impaction surface temperatures of 1275 to 1675 K. Under all conditions examined to-date, little or no deposition was noted with either kaolinite sample as shown in Figure 5. For the montmorillonite, however, capture efficiencies comparable to those of the San Miguel lignite ash previously examined were obtained. Detailed examination of the San Miguel lignite ash had indicated that calcium plus magnesium plus potassium levels of most particles were greater than 10% as oxides, by weight, yielding viscosities below the 10^8 poise believed necessary for adhesion (3). This produced particles with viscosities low enough to permit the particle to remain on the impaction surface subsequent to contact -i.e., viscosities were low enough to absorb the energy of collision. For the calcium

montmorillonite ash particles examined herein, the sum of the modifier ions calcium plus magnesium plus iron was in the range 6-12% for the individual particles studied. Note that this range is comparable to the San Miguel ash particles so similar viscosities are expected. Exact computation requires analysis for the final form of iron (ferrous v. ferric) and is currently underway.

A marked difference in deposit morphology was also noted between the kaolinite and montmorillonite samples, as expected. As Figure 6a shows, only a few glassy particles were retained on the tube surface for the K-WC sample. EDAX analysis of these particles showed them to be illitic in nature and therefore expected to adhere under the conditions of this study (cf. Figure 5). In Figure 6b, the molten adhesive nature of the montmorillonite particles at 1425°C deposition conditions is clearly evident. For this deposit, chemical composition was comparable to that noted both for the raw sample and for individual transformed particles: 20 wt% silica, 67% alumina, 5% each of magnesia and calcia, and 2.4% iron (ferric) oxide.

These results suggest that any mineral interactions which produce aluminosilicate ash particles with approximately 10% modifier ion concentration will give rise to extremely sticky ash particles, prone to deposit upon inertial impaction with wall surfaces. Kaolinite alone is of little concern because of a relative absence of modifier ions, but interactions with dispersed species such as calcium and magnesium could produce ash particles prone to adhere to tube surfaces. Ash particles derived from minerals such as illite and montmorillonite which are rich in modifier ions can deposit without the need for interaction with other species.

ACKNOWLEDGEMENTS

REFERENCES

1. Bryers, R.C., *Proc. EPRI Conf. on the Effects of Coal Quality in Power Plants*, October (1987).
2. Winegartner, E.C., *ASME Research Committee Report on Corrosion and Deposits from Combustion Gases* (1974).
3. Srinivasachar, S., Helble, J.J., and Boni, A.A., *Proc. 23rd Symposium (Int'l) on Combustion*, The Combustion Institute (in press) (1990).
4. Baxter, L.L., Hencken, K.R., and Harding, N.S., *Proc. 23rd Symposium (Int'l) on Combustion*, The Combustion Institute (in press) (1990).
5. Srinivasachar, S., Helble, J.J., and Boni, A.A., *Progr. Energy and Combust. Sci.* **16**, 281 (1990).
6. Srinivasachar, S., Helble, J.J., Boni, A.A., Shah, N., Huffman, G.P., and Huggins, F.E., *Progr. Energy and Combust. Sci.* **16**, 293 (1990).
7. Van Olphen and Fripiat, eds., Data Handbook for Clay Materials and Other Non-Metallic Minerals,, Pergamon Press, New York (1979).

Table 1. Clay Chemical Composition

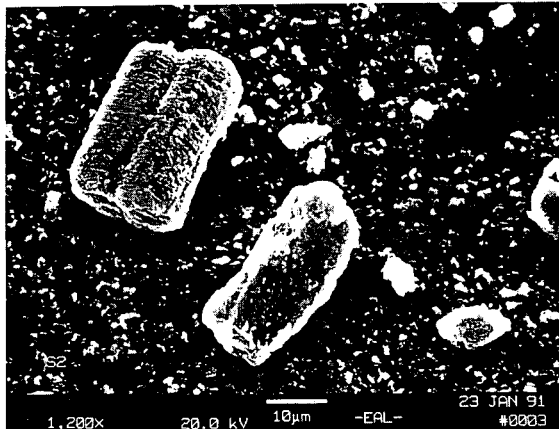|	Weight Percent								
	SiO_2	$A\ell_2O_3$	TiO_2	Fe_2O_3	FeO	MgO	CaO	Na_2O	K_2O
Kaolin-well crystallized	44.2	39.7	1.39	0.13	0.08	0.03	-	0.013	0.05
Kaolin-poorly crystallized	43.9	38.5	2.08	0.98	0.15	0.03	-	-	0.065
Ca-montmorillonite	60.4	17.6	0.24	1.42	0.08	6.46	2.82	0.063	0.19

Figure 1. Raw Sample of Well-Crystallized Kaolinite

177
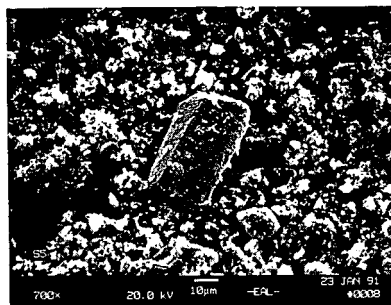
(a) Well Crystallized Kaolinite
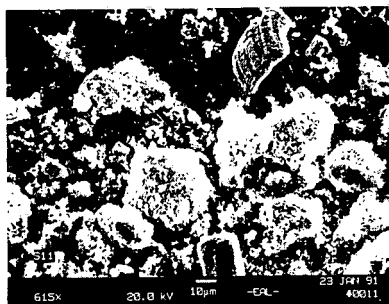
(b) Poorly Crystallized Kaolinite

Figure 2. Kaolinite Samples After Processing at 1500°C in 3 Percent O_2 for 2.9s
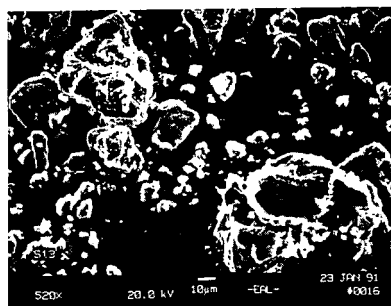
Figure 3. Raw Sample of Calcium-Montmorillonite

178
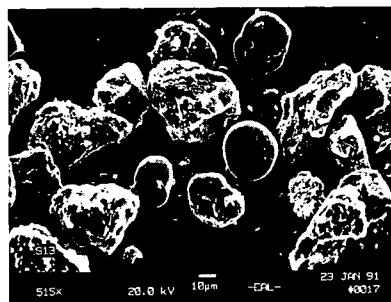
(a) 1s
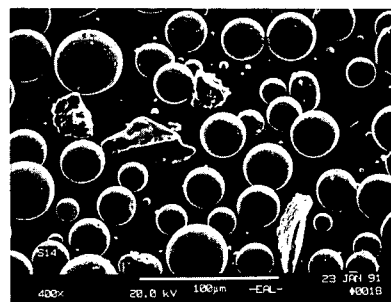
(b) 2.9s

Figure 4. Montmorillonite Samples After Processing at 1500°C in 3 Percent O_2

Figure 5. Comparison of Clay Sample Collection Efficiencies with Coal Ash Collection Efficiencies. Combustion conditions as noted

179

(a) Well Crystallized Kaolinite

(b) Ca-Montmorillonite

Figure 6.   Morphology of Initial Deposits Collected at 1425°C After Processing at
1500°C, 3 Percent O_2

Alkali/Silicate Interactions During Pulverized Coal Combustion

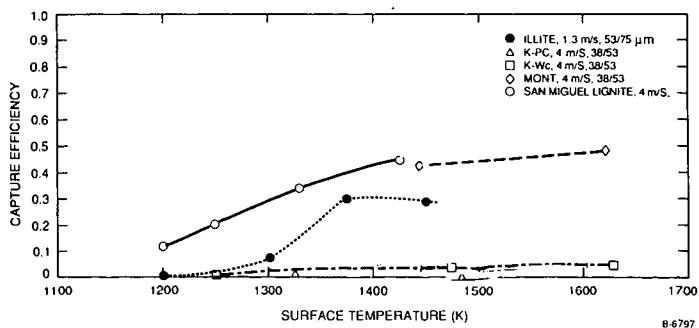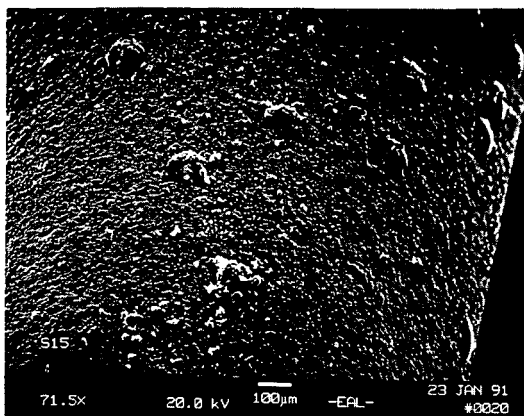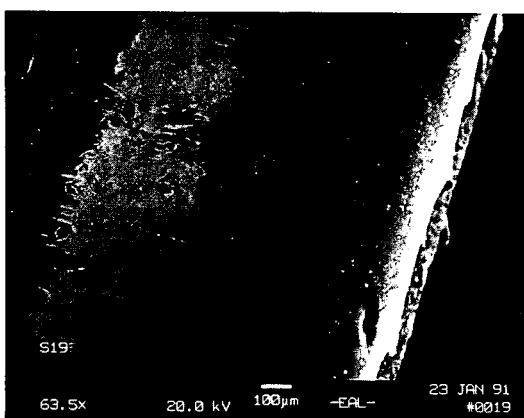Neal Gallagher, Thomas W. Peterson and Jost Wendt, Chemical Engineering Department, University of Arizona, Tucson, AZ 85721.
Keywords: coal combustion, alkali, aluminosilicates, aerosols

Introduction

During the combustion of pulverized coal, inorganic ash constituents result in the formation of submicron aerosol and large ash particles. It is evident that chemical transformations involving this mineral matter plays an important role in the ultimate size distribution and chemical composition of these particles. One such mineral matter transformation mechanism suggested by data collected in this laboratory is reaction of sodium (or sodium containing species) with aluminosilicates. This observation led to the postulated mechanism of sodium mobilization within a burning char particle reacting with inherent aluminosilicate particles. Mobile sodium which reached the surface of the char particle was assumed to escape to the bulk flue gas environment. Previous work by Lindner and Wall (1988) however suggested that sodium reaction with aluminosilicates takes place primarily after the sodium escapes the char particle. This work attempts to determine the relative importance of sodium reaction with aluminosilicates inside and external to the char particle.

Experimental Work

Experimental facilities included a 17kW down-fired pulverized coal combustor which supported premixed self-sustained flames of pulverized coal. Fly-ash samples were extracted from the combustor and diluted with quench air using an isokinetic probe. Size segregation of the fly-ash samples was accomplished using a Mark II Andersen 1 ACFM cascade impactor. Impaction substrates were 0.2 μm Flouropore filters coated with polyethylene glycol 600 and the after-filter was an uncoated Flouropore filter. The size segregated samples were subjected to atomic absorbance for bulk elemental analysis at the University of Arizona and CCSEM analysis at the University of Kentucky.

Experiments were performed using numerous pulverized coal samples. The data reported herein represent results obtained from an Australian Coal (Loy Yang) and a North Dakota Lignite (Beulah). Loy Yang was chosen since it had a relatively high sodium to aluminosilicate ratio in the original coal, but overall low aluminosilicates (see Table I). In addition to conventional combustion experiments with this coal, experiments were conducted in which an aluminosilicate additive (94 g kaolinite per kg additive-free coal) was included in the coal feed. The kaolinite had a mass mean diameter of 0.5 μm, density 2.63 g/cm^3, and aerodynamic size of 0.81 μm. The purpose of these "doped" runs was to ascertain the effect on Na behavior of the aluminosilicate materials. Table I also shows the original ash analysis in addition to the calculated ash analysis for the doped coal experiments.

The results from the Loy Yang experiments in the absence of additive can be summarized by Figure 1. Here, the fraction oxide of the major elemental species is plotted as a function of the impactor collection plate. TF represents the Total Filter analysis, AF the after-filter analysis and Plates 1 to 8 the larger to smaller particle sizes for the aerodynamic cut-off diameter.

Enrichment of sodium in the smaller sizes is apparent. The sustantial fraction of the sodium found in the smaller sizes could be due to either surface condensation or homogeneous nucleation, but it is clear in either case that the fraction of species in the smallest size range might be indicative of the amount of Na that reached the vapor phase.

When the kaolinite additive is included, a substantial shift in the Na distribution with respect to particle size is witnessed (Figure 2). Not all Na has been taken up by the kaolinite, however, as attested by the large Na fraction still found in the after-filter. This result is not surprising, since it is likely that any remaining submicron aerosols will still be dominated by those species which most easily vaporize. In examining the cumulative mass fraction of the Na that appears on each stage, about 75% of the Na was found in a size range less than 0.65μm in the absence of additive. When kaolinite was included, that fraction fell to about 12%. The additive has significantly changed the overall sodium distribution, but it is still unclear as to whether the mechanism was due to increased condensation, or chemical reaction of the Na with the aluminosilicates.

The experiments with the Loy Yang were conducted because this coal has the rather unusual property of high Na fraction and low aluminosilicate fraction in the parent ash. The Beulah Lignite coal also has relatively high Na content, but contains silicate material in the form of quartz, kaolinite, illite, montmorillonite, mixed silicates and miscellaneous silicates. The Beulah lignite contains approximately 0.065 g Na/g silicates, whereas the doped Loy Yang contained 0.052 g Na/g silicates. Previous work done here showed that the lower the sodium to silicate ratio the higher the fraction of sodium captured. The fraction of sodium not captured was taken as the fraction found on impactor plate 8 and the after-filter (less than 0.65 μm). From this argument alone it would be expected that the doped Loy Yang would exhibit a lower fraction of sodium in a size range less than 0.65 μm than the Beulah Lignite. Figure 3 compares the cumulative fraction sodium oxide as a function of impactor plate for the Beulah Lignite and the doped Loy Yang experiments. These results suggest that because a fraction of the silicate-containing materials in the Beulah Lignite is included within the char matrix (as opposed to being entirely extraneous, as is the case with the kaolinite-doped Loy Yang), there is more efficient Na capture by the silicate materials.

Further examination of the Beulah lignite data also suggests that perhaps a pure condensation mechanism may not be sufficient to explain the behavior of the Na in the presence of the silicate-containing materials. Figure 4 plots the fraction of the impactor sample that is Na oxide vs. the inverse-square of the cut-off diameter. Under pure condensation, such a plot would yield a straight line. This is true for particles in the very small size ranges, but this behavior deviates for larger particles, in spite of the fact that there is a non-negligible amount of Na in these larger particles. Examination via CCSEM (these analyses were performed at the University of Kentucky) of the composition of the individual particles on the largest impactor plate (Plate 1, Figure 5) also shows that, while many of the aluminosilicate-bearing particles had essentially no Na in them, those that did contain Na did so in a fairly narrow range of Na-Al+Si compositions.

Finally, impactor samples collected by cascade impactor from later Loy Yang runs were analyzed in such a way as to try to separate those Na species which are chemically bound to the

aluminosilicates from those which are simply surface-condensed on these particles. This was accomplished by dissolving a portion of the impactor sample in DI water (to get the surface-condensed sodium, presumably water soluble) and a portion in the standard acid reagent (to get all Na-containing species). There is some evidence that the reaction product of sodium with kaolinite (Punjak et al, 1989) is nephelite ($Na_2O \cdot Al_2O_3 \cdot 2SiO_2$). Nephelite is insoluble in cold water and decomposes in hot water. Our DI samples were never subjected to temperatures above 40 °C. Albite and jadite ($Na_2O \cdot Al_2O_3 \cdot 6SiO_2$ and $Na_2O \cdot Al_2O_3 \cdot 4SiO_2$) were also reported as insoluble. One possible product of reaction between sodium and quartz was $Na_2Si_2O_5$ as evidenced by equilibrium calculations. While this species is soluble, the amount of quartz in the Loy Yang was low overall.

The result of this analysis showed that while a large fraction of the Na captured was indeed water soluble (almost exclusively so in the smaller sizes), there was a substantial fraction of Na in the larger sizes (as high as 50% in some cases) which was water-insoluble. This certainly suggests that chemical reactions to form Na-aluminosilicates plays some role in the fate of Na during coal combustion.

Model Development

In order to mechanistically explain the varied experimental observations reported above, a model was developed to follow the release and capture of sodium species by Al and Si-bearing minerals. The model developed describes the release of sodium from a burning char particle, accounting for char particle shrinkage and sodium capture by silicate minerals, both within and outside the char particle. The assumed chemical reaction between sodium and alumino-silicates is based on work done by Punjak et. al (1989) and Uberoi et. al (1990). Additionally, chemical equilibrium calculations suggested the appropriate reaction to consider between sodium and quartz, the other form of Si considered.

Inside the char particle, species balances on the bound sodium, the "mobile" sodium and the included Si-containing species with which Na can react yield:

$$\frac{\partial C_a'}{\partial t} = D \frac{1}{r^2} \frac{\partial}{\partial r}(r^2 \frac{\partial C_a'}{\partial r}) - C_a' \sum_{i=1}^{n} \frac{\eta \, k_{ai}' S \, k_{mi}' C_i'}{\eta \, k_{ai}' S_i C_i' + k_{mi}'} + k_s' C_s' \qquad 1$$

$$C_a' = 0 \ , \ R = R_0 \quad at \ t = 0 \qquad 2$$

$$\frac{\partial C_a'}{\partial r} = 0 \qquad at \ r = 0 \qquad 3$$

$$-D\frac{\partial C_a'}{\partial r} = k_{mb}'(C_a' - C_b') \quad at \ r = R(t) \tag{4}$$

$$\frac{dC_s'}{dt} = -k_s'C_s' + \frac{C_s'R^{\cdot 3}}{(R^3 - R^{\cdot 3})}\frac{3}{R}\frac{dR}{dt} \tag{5}$$

$$C_s' = C_{s0}' \quad at \ t = 0 \tag{6}$$

$$\frac{\partial C_i'}{\partial t} = -\frac{\beta_i\eta_i k_{ai}'S_i k_{mi}'C_i'C_a'}{\eta_i k_{ai}'S_i C_i' + k_{mi}'} - \frac{C_i'}{V}\frac{dV}{dt} \tag{7}$$

$$C_i' = f_i C_{i0}' \quad at \ t = 0 \quad for \ i = 1,...,n \tag{8}$$

Once the volatile migrates to the surface of the shrinking spherical char particle it can escape to the bulk flue gas phase. The concentration in the bulk, C_b', can change due to the mobile sodium escaping the char particle, reactions of the volatile species with extraneous silicate species j, particle shrinkage and concentration changes due to temperature effects. The condition given by equation 12 describes a bulk flue gas phase that is initially sodium-free.

$$\frac{dC_b'}{dt} = k_{mb}'a_v(C_a'|_{r=R} - C_b') - C_b'\sum_{j=1}^{n}\frac{\eta_j k_{aj}'S_j k_{mj}'C_j'}{\eta_j k_{aj}'S_j C_j' + k_{mj}'}$$

$$- (C_s' + C_a'|_{r=R})\frac{dR}{dt}a_v - \frac{C_b'}{V_b}\frac{dV_b}{dT}\frac{dT}{dt} \tag{9}$$

$$C_b' = 0 \quad at \ t = 0 \tag{10}$$

Finally, a balance on the extraneous silicate species yields

$$\frac{dC_j'}{dt} = -\frac{\beta_j\eta_j k_{aj}'S_j k_{mj}'C_j'C_b'}{\eta_j k_{aj}'S_j C_j' + k_{mj}'} - \frac{C_j'}{V_b}\frac{dV_b}{dT}\frac{dT}{dt} \tag{11}$$

$$C_j' = g_j C_{j0}' \qquad at \ t = 0 \quad for \ j = 1,...,n \qquad\qquad 12$$

Parametric description of the reaction kinetics and mass transfer is accomplished with the following models:

$$k_{ai}' = A_i e^{-E_{ai}'/RT} \qquad\qquad 13$$

$$k_{mb}' = D_b/R \qquad\qquad 14$$

$$k_{mi}' = \frac{D_0 v}{R_i} \frac{4\pi R_i^2 f_i C_{i0}'}{\frac{4}{3}\pi R_i^3 \ \rho_i} = \frac{3vf_i C_{i0}'}{\rho_i} \frac{R_0^2}{R_i^2}\left(\frac{D_0}{R_0^2}\right) \qquad\qquad 15$$

$$k_s' = A_s e^{-E_{ai}'/RT} \qquad\qquad 16$$

$$\eta_{ij} = 1. \qquad\qquad 17$$

$$k_{mb}'a_v = \frac{D_{b0}v}{R}\left(a_{vo}\frac{R^2}{R_0^3 T}\right) = a_{vo}\frac{D_{b0}}{D_0}\frac{vu}{T}\left(\frac{D_0}{R_0^2}\right) \qquad\qquad 18$$

$$k_{mj}' = \frac{D_{b0}v}{R_j} \frac{4\pi R_j^2 \ g_j C_{j0}'}{\frac{4}{3}\pi R_j^3 \ \rho_j} \frac{298}{T} = \frac{D_{b0}}{D_0} \frac{3vg_j C_{j0}'}{\rho_j} \frac{R_0^2}{R_j^2} \frac{298}{T}\left(\frac{D_0}{R_0^2}\right) \qquad\qquad 19$$

$$a_v = \frac{(4\pi R^2)(feedcoal)}{(\rho_0 \frac{4}{3}\pi R_0^3)60(feedair)} \frac{298}{T} = a_{vo}\frac{R^2}{R_0^3 T} \qquad\qquad 20$$

$$a_{vo} = \frac{(feedcoal)(298)}{\rho_0(20)(feedair)} \qquad\qquad 21$$

The temperature was determined by fitting the four parameter model below to the measured temperature profile and residence time calculations.

185

$$T(t) = a_1(1 - e^{-a_2(t+a_4)})e^{-a_3(t+a_4)}$$ 22

The residence time calculation accounted for geometry and temperature effects.

The char particle radius was determined using a simple char burnout model. According to Smith (1971) the rate of burnout R_{ac} is given by:

$$R_{ac} = Ae^{-E_a/RT_p}$$ 22

Where R_{ac} is in grams of char per second per cm^2 external surface area per atmosphere oxygen. From this equation, the rate of change of particle radius is given by:

$$\frac{dR}{dt} = -\frac{P_{O_2}}{\rho_c}Ae^{-E_a/RT}$$ 23

Where R is the char particle radius, and ρ_c is the char density.

Conclusions

Experiments suggest that the Na could escape the burning char and reach the bulk flue gas phase, as observed by the enrichment of Na in the smallest size classes. For the Loy Yang, the size distribution of the Na was greatly affected by the introduction of the additive, with the fraction of Na found in the smallest sizes being reduced from approximately 75% to 12%. It was clear that, while condensed Na species were dominant in the smaller particle size ranges, Na-containing aluminosilicates were indeed present in the large size particles.

Preliminary modeling results have indicated that (1) the reaction is fast enough for the Na to be captured by the included aluminosilicates during char burnout, and (2) the extent to which this occurs depends strongly on mass transfer of the Na through the char matrix.

REFERENCES

Lindner E.R. and Wall T.F., "An Experimental Study of Sodium-Ash Reaction During combustion of Pulverized Coal", Fourth Engineering Foundation Conference on Mineral Matter and Ash Deposition from Coal, Feb. 21-26, 1988, Santa Barbara, CA.

Punjak, W.A., Uberoi, M., and Shadman, F., "High Temperature Adsorption of Alkali Vapors on Solid Sorbents", AIChE Journal, 35, 1186 (1989).

Smith, I.W., "Kinetics of Combustion of Size-Graded Pulverized Fuels in the Temperature Range 1200-2270 °K", Combustion and Flame, 17, 303-314 (1971).

Uberoi, M., Punjak, W.A., and Shadman, F., "The Kinetics and Mechanism of Alkali Removal From Flue Gases by Solid Sorbents", Prog. Energy Combust. Sci. 16, 205 (1990).

NOMENCLATURE

A_i = frequency factor for reaction of volatile with inherent silicate species i, 1/(cm² silicate i per g silicate i)/(g silicate i per cm³ char)/(s).

A_j = frequency factor for reaction of volatile with extraneous silicate species j, 1/(cm² silicate j per g silicate)/(g silicate j per cm³ flue)/(s).

A_v = frequency factor for release of bound volatile from the char matrix, (1/s).

A_v = char surface area per volume flue, (cm² char)/(cm³ flue).

A_{vo} = reference parameter for A_v, (K).

C_a' = concentration of volatile inside the char particle,(g volatile)/(cm³ char).

C_b' = concentration of volatile outside the char in the bulk flue gas phase, (g volatile)/(cm³ char).

C_i' = concentration of inherent silicate species i, (g silicate i) /(cm³ char).

C_j' = concentration of extraneous silicate species j, (g silicate j) /(cm³ flue).

C_c' = concentration of volatile bound to the char matrix, (g bound vola- tile)/(cm³ char).

C_{io}' = initial concentration of all inherent silicate species,(g silicate)/(cm³ char).

C_{jo}' = initial concentration of all extraneous silicate species, (g silicate)/(cm³ flue).

C_{co}' = initial concentration of volatile bound to the char matrix, (g bound volatile)/(cm³ char).

D = effective diffusivity of volatile inside the char particle, (cm²)/(s).

D_{ib} = diffusivity of volatile in a char particle pore, (cm²)/(s).

D_b = diffusivity of volatile in the bulk flue gas phase, (cm²)/(s).

D_{bo} = diffusivity of volatile in the bulk flue gas phase at the reference temperature T_0, (cm²)/(s).

D_0 = effective diffusivity of volatile inside the char particle at the reference temperature T_0, (cm²)/(s).

E_c = activation energy for char burning, (J/gmole).

E_{ai} = activation energy for reaction of volatile with inherent silicate species i, (J/gmole).

E_{aj} = activation energy for reaction of volatile with extraneous silicate species j, (J/gmole).

E_w = activation energy for release of bound volatile from the char matrix, (J/gmole).

f_i = fraction of inherent silicates that is species i.

g_i = fraction of extraneous silicates that is species j.

k_{ai}' = reaction rate coefficient between volatile and inherent silicate species i, 1/(cm² silicate i per g silicate i)/(g silicate i per cm³ char)/(s).

k_{aj}' = reaction rate coefficient between volatile and extraneous silicate species j, 1/(cm² silicate j per g silicate j)/(g silicate j per cm³ flue)/(s).

k_{mb}' = interphase mass transfer coefficient for transport of volatile from the char to the bulk flue gas phase, (cm)/(s).

k_{mi}' = interphase mass transfer coefficient for transport of volatile to inherent silicate species i, 1/(s).

k_{mj}' = interphase mass transfer coefficient for transport of volatile to extraneous silicate species j, 1/(s).

k_v' = reaction rate coefficient for release of volatile from the char matrix, 1/(s).

m = char particle mass, (g).

n = number of silicate species.

p_{O2} = partial pressure of oxygen, (atms).

r = radial position inside the spherical char particle, (cm).

R = char particle radius, (cm).

R_i = inherent silicate particle radius, (cm).

R_j = extraneous silicate particle radius, (cm).

R_0 = initial char particle radius, (cm).

R^* = final char particle radius (burnout complete), (cm).

S_i = specific surface area of inherent silicate species i, (cm² silicate i)/(g silicate i).

S_j = specific surface area of extraneous silicate species j, (cm² silicate j)/(g silicate j).

t = temporal variable, (s).

T = temperature, (K).

T_0 = reference temperature, (K).

V = char particle volume, (cm³ char).

V_b = bulk flue gas volume, (cm³ flue).

$\beta_{i,j}$ = stoicheometric factor, (g silicate i,j)/(g Na).

ϵ = char porosity, (cm³ void)/(cm³ char).

η_i = effectiveness factor for inherent silicate species i.

η_j = effectiveness factor for extraneous silicate species j.

ρ_i = inherent silicate density, (g)/(cm³).

ρ_j = extraneous silicate density, (g)/(cm³).

ρ_c = initial char particle density, (g)/(cm³).

feedair = air feed rate into the combustor, (slpm).

feedcoal = coal feed rate into the combustor, (kg/hr).

187

Table I. Ash analysis for doped and undoped Loy Yang.

Loy Yang oxides	undoped % AR	undoped frac oxide	doped % AR	doped frac oxide
Al$_2$O$_3$	0.04	0.036	3.36	0.404
SiO$_2$	0.16	0.132	4.02	0.483
CaO	0.06	0.047	0.05	0.006
Fe$_2$O$_3$	0.08	0.066	0.07	0.009
Na$_2$O	0.60	0.490	0.55	0.066
K$_2$O	< 0.01	0.004	< 0.01	0.001
MgO	0.28	0.225	0.25	0.030
Total	1.9	1.00	10.21	0.999

Run 39 Loy Yang Without Additive
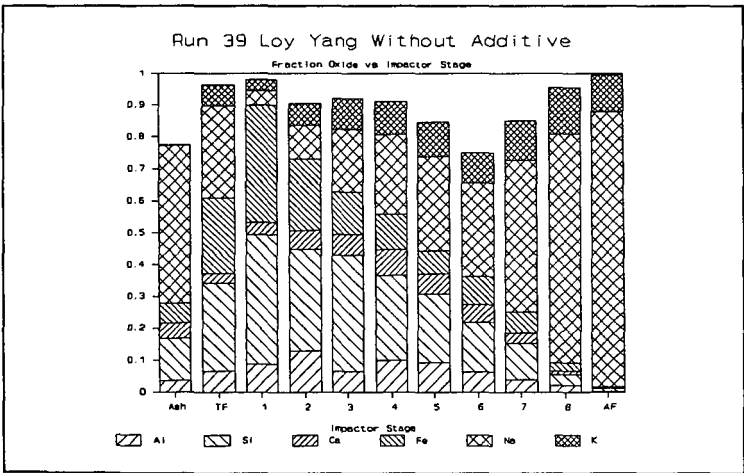Fraction Oxide vs Impactor Stage

Figure 1 Fraction Oxide vs Impactor Stage for Loy Yang Without Additive
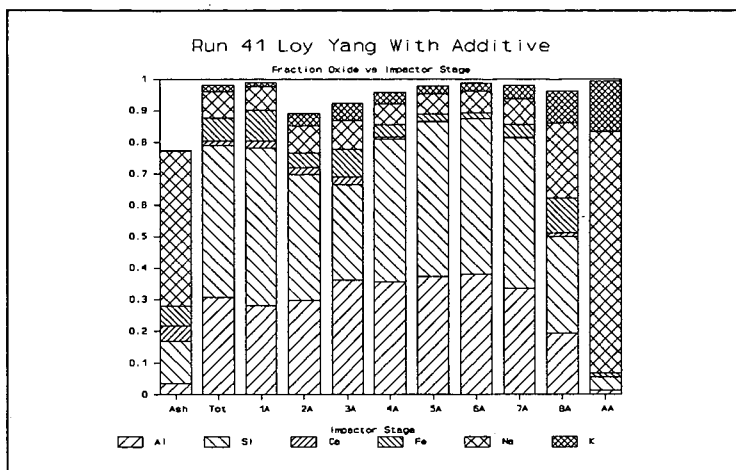
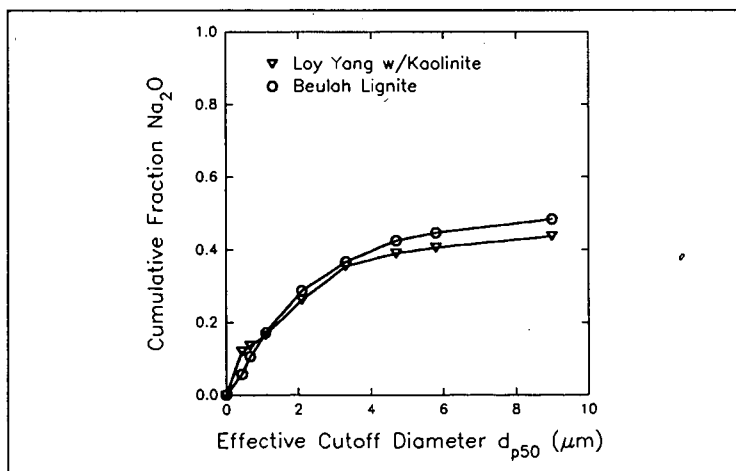**Figure 2** Fraction Oxide vs Impactor Stage for Loy Yang With Additive

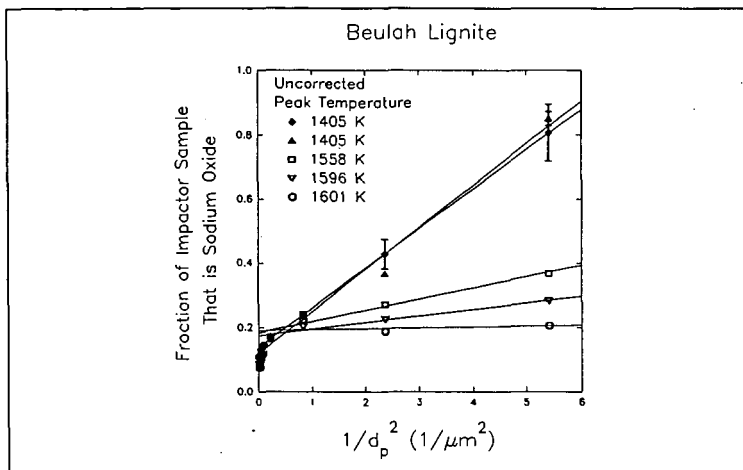**Figure 3.** Cumulative Fraction Na_2O vs d_p for Beulah Lignite and Loy Yang doped with Kaolinite
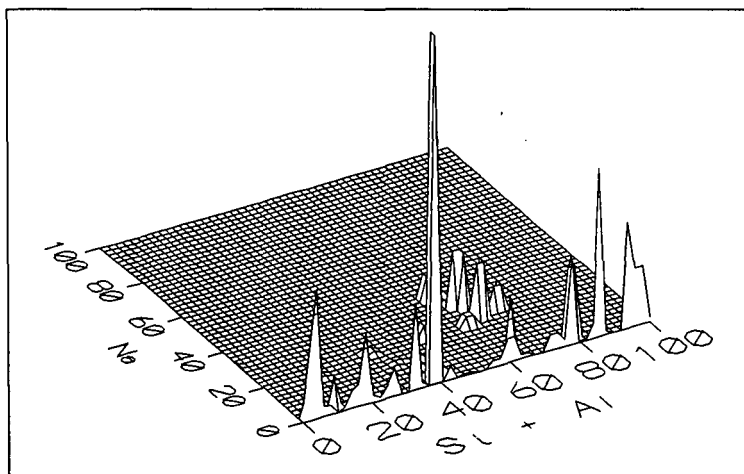
Figure 4 Fraction Na$_2$O vs 1/d$_p$^{2}.

Figure 5. Beulah Lignite Impactor Plate 1.

FRACTAL DIMENSION ANALYSIS OF
CHARS PRODUCED FROM SYNTHETIC COAL

Douglas K. Ludlow, Wendy M. Vosen, and Thomas A. Erickson
Department of Chemical Engineering
University of North Dakota
Grand Forks, North Dakota

Keywords: Fractal Dimension, Char, Combustion

ABSTRACT
The fractal dimension, a measure of surface ruggedness, of chars was measured using physisorption techniques. Coals and chars at different stages of combustion were prepared in a laminar flow (drop-tube) furnace. By adjusting the residence time of the coal and char particles in the drop tube, the particles experienced combustion conditions for various lengths of time. The particles were quickly cooled and quenched in an inert atmosphere. The samples were analyzed using a scanning electron microprobe and by using the physisorption of a series of gases. The adsorption data was used to test if the char surface was fractal and to determine the fractal dimension. Changes in the fractal dimension during combustion were quantified. As the char was burned the fractal dimension increased as the carbon matrix burned away leaving mineral moieties. As combustion continued and the carbon burned completely away leaving a mineral fly ash particle the fractal dimension decreased again. Fractal dimension information will be used to model the formation of surface moieties that occur on the char from the inorganic mineral matter dispersed within the coal (Benson et.al., 1988).

BACKGROUND
The morphology and adsorption characteristics of a char surface affect the rate of combustion and the mass transfer processes of the reactants and products involved. A recently developed experimental technique, fractal analysis using physisorption, was used to measure the development of surface morphology during combustion. The conditions at the surface of a burning coal or char particle affect the rate of combustion and the extent of conversion which, in turn, affects the formation of combustion products and unwanted by-products. A laminar flow (drop-tube) furnace was used to produce chars at various stages of combustion for this study.

Background: Physical Adsorption and Surface Area
The adsorption of gases on porous solids is used to measure the surface area of the solid by determining the amount of gas adsorbed as a function of the partial pressure of the adsorbate. Standard surface area determinations are made by adsorbing nitrogen at 77 K and calculating the surface area using the model developed by Brunauer, Emmett and Teller (1938), known as BET (Gregg and Sing, 1982). Other adsorption models can be used. The adsorption model of Dubinin-Polanyi (DP) has been used to determine the surface area of coals and chars(Gregg and Sing, 1982; Marsh and Siemieniewska, 1965). For this research the BET model gave better correlation of the adsorption data (higher correlation coefficients) and was used for all gases. The dynamic flow system was used to determine the gas adsorption isotherms for this research and will be described in the "methods" section.

Background: Fractal Analysis
Adsorption of gases other than nitrogen have been successfully used to measure surface area. Each adsorbing gas has a different molecular size and the surface area covered by an adsorbed molecule of several gases has been determined (Gregg and Sing, 1982, McClellan and Harnsberger, 1967). Mathematical strategies for describing rugged or indeterminate boundaries, known as fractal geometry, developed by Mandelbrot (1977, 1982) have recently been applied to the description of surface structure (Avnir, 1986, 1989; Avnir and Pfeifer, 1983; Avnir et.al., 1983, 1984, 1985; Delfosse et.al., 1988; Fairbridge et.al., 1986; Farin et.al., 1984, 1985a, 1985b; Fripiat et.al., 1986; Jabkhiro and Delfosse, 1988; Ludlow and Moberg, 1990; McEnaney 1988; Moberg, 1990; Ng et.al., 1987; Pfeifer, 1984; Pfeifer and Avnir, 1983; Pfeifer et.al., 1983, 1984; Van Damme and Fripiat, 1985; Van Vliet and Young, 1988; Vosen, 1990; Wilkie, 1990). Theories have been developed to determine a quantity known as the "fractal dimension," which is a measure of the ruggedness of a surface. The value of the fractal dimension varies from the topological dimension of 2 to the euclidean dimension of 3. When a molecule interacts with a surface having a fractal dimension of 2.0 it is essentially encountering a two dimensional plane. When the fractal dimension approaches 3.0, an adsorbing molecule is encountering a three dimensional surface.

Two methods to determine the fractal dimension of solids from adsorption data have been demonstrated. In the first method a single adsorbate is used, and the surface area is measured using different particle sizes of the sample. This technique requires grinding the sample, using a sonic sieve to size the particles into very tight particle ranges, and measuring particle size distribution in each range. This method has been demonstrated (Avnir et.al., 1985; Fairbridge et.al., 1986; Ng et.al., 1987) and has the major advantage that only one adsorbate is required. The disadvantages are the extensive sample preparation required and the possibility that grinding the sample may affect the fractal dimension.

The second method to determine fractal dimension is to adsorb a series of different sized molecules onto a single sample. Because the smaller molecules have access to the "finer" surface structure that the larger molecules do not, a difference in measured surface area is found. Using this difference, a scheme has been developed to determine the fractal dimension. This method has also been demonstrated (Avnir *et.al.*, 1985; Van Damme and Fripiat, 1985). The second method does not explicitly require the sonic sieve, nor the particle size analyzer, but it does require the ability to adsorb different gases onto the sample. Using a mass flow controller and a gas handling manifold, various adsorbate/helium mixtures can be used for surface analysis.

Background: Inorganics in Coal

One objective of this study is to determine the effect that temperature and residence times, found in typical industrial pulverized-coal boilers, have on the formation of char and fly ash morphology. Sodium silicates and sodium sulfates form the major inorganic constituents of coal. These inorganic constituents will affect the surface structure of the chars and fly ash being developed. Western coals contain significant quantities of sodium, sulfur, and silica. The inorganic constituents of coal pass through the combustion zone either as solids, liquids or vapor and ultimately react or condense to form fly ash particles. Some of the fly ash particles are transported to the heat exchange surfaces and form a deposit which will grow with time. As these deposits increase they insulate the heat transfer surface, decreasing the thermal efficiency of the boiler.

Sodium volatilizes upon combustion, becomes dispersed through the gas stream, and later condenses on other ash particles and on the metal surfaces. Wibberly and Wall(1982) proposed that sodium containing materials provide a binding matrix that fuses ash particles together. The mechanism of formation of such a material may be the key to understanding the deposition processes of western coals. Studies by Sondreal(1977) on low rank coals from the western U.S. revealed that the severity of ash fouling deposits correlates not only with sodium concentration but also with total ash content.

One of the major problems in studying the roles of inorganics during coal combustion is the complexity of coal. To alleviate this problem, the interaction of the three inorganic constituents were studied in a model system with use of a synthetic coal (glassy carbon) incorporated with the desired inorganics(Erickson 1988; Erickson 1990).

EXPERIMENTAL METHODS

Synthetic Coal Preparation

The purpose of a synthetic coal is to be able to study the interactions of coal combustion in a system not as complex as actual coal. The synthetic coal must have similar combustion characteristics as well as lending itself to the addition of minerals in a quantitative manner. A furfuryl alcohol polymer has been found to be such a substance(Schmitt 1976; Senior and Flagen 1984; Levendis and Flagen 1987).

The preparation of the synthetic coal was developed by Senior(1984). The technique was slightly modified for this study and is described in detail(Erickson 1990). In brief, the quartz (which had been sized to 5 mm) was added prior to the polymerization so that it would behave as an included mineral. After the polymer was cured, the synthetic coal was ground and sized. Analysis of the sized coal indicated that 0.4 weight percent sulfur was inherent in the synthetic coal polymer due to the p-toluensulfonic acid which is used as a catalyst for the polymerization. Additional sublimed sulfur was added extraneously and mixed with the ground synthetic coal so that the final composition would consist of 1% sulfur. Sodium was added using a solution of sodium benzoate in an ethanol solution. The sodium benzoate/alcohol solution was mixed with the ground coal and the alcohol evaporated. This has been found(Mills 1989) to effectively load the sodium on the coal so that it will easily volatilize.

The chemistry of the polymerization of furfuryl alcohol to form a glassy carbon has been studied extensively(Dunlop and Peters 1953; Riesz and Susman 1960; Conley and Metil 1963; Weswerka et.al 1968; Fitzer et.al 1969). For this study characterization of the synthetic coal included analysis by SEM, CCSEM, TGA, Proximate-Ultimate, Inductively Coupled Plasma (ICP) (with acid digestion and lithium boride extraction), BET surface area from nitrogen adsorption and fractal analysis using gas adsorption. By formulation and analysis the synthetic coal included 10 percent SiO_2 (quartz), 5 percent Na and 1 percent S by weight. The weight loss with respect to temperature from the TGA were in qualitative agreement with TGA results for a low rank coal. The nitrogen BET surface area of the synthetic coal is 50.3 m^2/g.

Laminar Flow Furnace

The prepared samples of synthetic coal were burned in the laminar flow furnace with 20 percent excess air (to ensure complete combustion). The laminar flow furnace is an instrument available through the University of North Dakota, Energy and Environmental Research Center(Zygarlicke *et.al.*, 1989). The pulverized and sized synthetic coal is fed to the laminar flow furnace and burned under preset conditions. The char and fly ash is collected using a water-cooled, nitrogen-quenched probe and collected on filter paper. Six different samples of char and fly ash were prepared using the laminar flow furnace. These six samples along with two samples of synthetic coal were analyzed using the scanning electron microprobe and fractal dimension analysis.

Gas Adsorption

A dynamic flow adsorption instrument is one of the most popular methods to measure gas adsorption. A mixture of adsorbate and helium passes through a thermal conductivity (TC) detector, across the sample, and then through a matched TC detector. The TC detectors are connected in a bridge circuit so that a millivolt signal, which is

192

proportional to the difference in the concentrations of the adsorbate before and after flowing through the sample, is generated. When flow across the sample is initiated, a signal will be generated from the bridged TC detectors because the concentration of the adsorbate will decrease as it is adsorbed onto the surface. A signal will not be generated by the TC detectors when equilibrium has been achieved. The amount adsorbed is determined from the area under the curve of a plot of the TC signal versus time. To accurately measure the surface area the amount adsorbed should be determined at three to five different adsorbate/helium compositions. However, due to experimental difficulty, some samples were analyzed at only two compositions.

A Micromeritics, Flowsorb 2300 II with a mass flow controller was used to obtain all gas adsorption measurements. The instrument was plumbed so that several different adsorbates (nitrogen, carbon dioxide, ethane, propane and n-butane) can be mixed with helium and used for gas adsorption.

To measure the complete isotherm, each adsorbate was adsorbed at different partial pressures. In order for physical adsorption to occur, the adsorption conditions need to be close to the boiling temperature of the adsorbate. Desorption temperatures are set at any convenient temperature above the adsorption temperature so that desorption will occur.

BET Equation

The BET adsorption model (Brunauer $et.al.$, 1938) is commonly used to determine surface area from physisorption data. The relation:

$$\frac{P}{V(P_0-P)} = \frac{1}{V_mC} + \frac{C-1}{V_mC}\frac{P}{P_o} \qquad (1)$$

is used to determine V_m, the monolayer coverage. In the equation, P is the adsorbate partial pressure (mmHg), P_0 is the saturation pressure (mmHg), and V is the volume adsorbed (cm^3 STP/g of sample). The constant C is an experimentally determined constant which is related to the heat of adsorption. The BET equation is considered valid for values of C between 10 and 110. For values of C between 2 and 10 the relationship can be applied but may be within 100% error. For C values greater than 110 the model is expected to be within 20% error. Using Equation 1 the monolayer coverage can be determined from the slope and intercept of a plot of $P/V(P_0-P)$ versus P/P_0.

Fractal Dimension Analysis

The concepts developed by Mandelbrot (1977, 1982) can be applied to the determination of surface ruggedness. Different sized molecules will have different access to surfaces that are rugged or indeterminate. This concept can be visualized in Figure 1. Avnir (1989) developed the relationship:

$$V_m \propto \sigma^{(-D/2)} \qquad (3)$$

where V_m is the monolayer coverage, σ is the cross-sectional area of the adsorbate molecule, and D is the fractal dimension. This equation can be written as:

$$V_m = k\sigma^{(-D/2)} \qquad (4)$$

where k is a prefactor which contains the necessary dimensional conversions. This term is called the lacunarity (Mandelbrot, 1982). The constant k is the monolayer value for unit σ and carries information about the connectivity and porosity of the surface (larger values of k correspond to a greater extent of porosity). The value of D is expected to have a value between 2 and 3.

Equation 4 can be linearized by taking the logarithm of both sides, which results in:

$$\log V_m = \log k - D/2 \log\sigma \qquad (5)$$

Equation 5 is the working relationship, and indicates that a plot of $\log V_m$ versus $\log\sigma$ for various adsorbates on a given adsorbent should be a straight line with slope of $-D/2$ and intercept of $\log k$.

Experimental Matrix

In order to maintain the experimental integrity of the study and to eliminate any operator bias, the order in which the various adsorptions were performed was randomized. Five sample holders for the gas adsorption unit were available so a suite of five samples were run first followed by a suite of three samples. The order in which the adsorbates were used was randomized, the order in which the various gas compositions were used was randomized, and finally the order in which the samples were analyzed at each composition was randomized. For each adsorbate composition on a given sample, four to six adsorption/desorptions were performed.

RESULTS

The synthetic coal sample was prepared and burned in the laminar flow furnace. The resulting chars and fly ash particles were collected and characterized using the SEM, CCSEM and TGA. The remaining char and fly ash particles were used for the gas adsorption analyses. Figure 2 shows a typical BET plot (nitrogen on sample 3).

Using the gas adsorption data (V_m) and McClellan and Harnsberger's (1967) cross-sectional areas, fractal plots were made for each sample. A sample plot is shown in Figure 3. The fractal dimension determined for each sample is found in Table 1.

DISCUSSION OF RESULTS

As the synthetic coal particles burn the carbon matrix is removed and the remaining mineral constituents form small beads on the char surface. There is evidence of the interaction of the sodium with the silica because the mineral

particles have rounded edges corresponding to a sodium silicate particle. At the operating temperatures, silica is not expected to be molten. However, the heat released during the combustion, may be enough to raise the particle temperature to point above the melting point of silica.

The formation of the sodium silicate moieties on the surface of the char drastically changes the surface morphology of the chars at the different stages of combustion. This was evident in the SEM micrographs. The determination of the fractal dimensions gives a quantitative description of the surface ruggedness. For the synthetic coal particles the surface fractal dimension is initially close to 2. As the particle burns and there is an increase in the ruggedness and the fractal dimension increases. Finally as the carbon matrix completely burns away and the remaining minerals coalesce, the fractal dimension decreases. This is demonstrated in Figure 4 which shows the plot of fractal dimension versus carbon loss. The lacunarity (prefactor) also gives some information about the degree of connectivity and porosity of the surface. The lacunarity also increases in the initial stages of combustion and again decreases as the mineral matter starts to coalesce. This is shown in Figure 5.

Sample Size

The results for some of the samples are less than satisfactory. The primary difficulty with these samples was that there was not enough sample produced in the laminar flow furnace. The Flowsorb II 2300 has resolution down to 0.002 cm^3 STP, however, the accuracy falls off for adsorptions below 0.2 cm^3 STP. Typical procedures for samples with a total volume adsorbed less than 0.2 cm^3 STP is to load the sample cells with more sample. Due to the prohibitive cost of producing more char and fly ash samples, it was decided to attempt the analyses with the existing samples (samples 7 and 8) which were smaller than desired. It was evident from the results that the range of the instrumentation had been exceeded for the smaller sized samples.

Sample Analysis Time

A difficulty that may prevent fractal dimension analysis from becoming a "routine" analysis is the time involved in obtaining the adsorption data. For each sample, five different adsorbates were used, and each adsorbate was adsorbed at three to five different compositions. In addition, at each composition from four to six adsorption/desorption cycles were performed. Each adsorption/desorption cycle requires from one to one and a half hours to complete. Thus the analysis time to determine the fractal dimension of a single sample takes on the order of 100 hours of instrument (operator) time.

However, due to the quantitative nature of the resulting measure of surface ruggedness, the technique still has applications with selected samples of important research applications. There is the possibility that the technique can be further refined to decrease the total analysis time required for each sample.

Cross-sectional areas

An additional difficulty with the analysis is that of determining to correct cross-sectional area of the molecules. This is a notorious problem of surface science (Farin et.al., 1985; Meyer et.al. 1986; McClellan and Harnsberger, 1967) and has yet to receive satisfactory solution. The current state of knowledge is the predictions given by McClellan and Harnsberger (1967). The difficulty with these correlations is that the predictions are based on the idea that different adsorbates should give the same surface area. This can only be true if the adsorbent has a molecularly smooth surface with a fractal dimension of 2. Since McClellan and Harnsberger's work was completed before the concept of fractal surfaces appeared in the literature, these considerations were not taken into account.

CONCLUSIONS

The surface fractal dimension of burning synthetic coal at different stages of combustion have been determined (Vosen, 1990). The experimental technique of using dynamic flow adsorption instrument to determine fractal dimension from gas adsorption data has been demonstrated (Ludlow and Moberg, 1990; Moberg, 1990; Vosen, 1990; Wilkie, 1990). Information (experience) obtained from this study will lead to further improvements of the technique. The fractal dimensions determined, for samples with sufficient sample size, corresponded well with the apparent changes in surface structure at the different stages of combustion.

ACKNOWLEDGEMENTS

REFERENCES

Avnir, D., "Fractal Aspects of Surface Science - An Interim Report," in *Better Ceramics Through Chemistry II*, Brinker, C. J., Clark, D. E., and Ulrich, D. R. (eds), Materials Research Society, Pittsburgh, PA, 321-329 (1986).

Avnir, D. ed., *The Fractal Approach to Heterogeneous Chemsitry - Surfaces, Colloids, Polymers*, John Wiley & Sons, New York, (1989).

Avnir, D., Farin, D., and Pfeifer, P., "Chemistry in Noninteger Dimensions Between Two and Three. II. Fractal Surfaces of Adsorbents, " *The Journal of Chemical Physics*, 79(7), 3566-3571 (1983).

Avnir, D., Farin, D., and Pfeifer, P., "Molecular Fractal Surfaces," *Nature*, 308(5956), 261-263 (1984).

Avnir, D., Farin, D., and Pfeifer, P., "Surface Geometric Irregularity of Particulate Materials: The Fractal Approach," *Journal of Colloid and Interface Science*, 103(1), 112-123 (1985).

Avnir, D. and Pfeifer, P., "Fractal dimension in chemistry. An intensive characteristic of surface irregularity," *Nouveau Journal De Chimie* 7(2), 71-72, (1983)

Benson, S. A., Sweeny, P. G., Abrahamson, H. B., Radonovich, L. J., Puffe, W. H., and Zygarlicke, C. J., "Combustion Inorganic Transformations," Ninth Quarterly Technical Progress Report, DOE/DE/FC21-86MC10637, July (1988).

Brunauer, S., Emmett, P. H., and Teller, E., "Adsorption of gases in multimolecular layers, " *Journal of American Chemical Society*, 60, 309-319 (1938).

Conley, R. T. and Metil, I., "An Investigation of the Structure of Furfuryl Alcohol Polycondensates with Infared Spectroscopy," *Journal of Applied Polymer Science*, 7, 37-52 (1963).

Delfosse, L., Ponsolle, L. and Jabkhiro, E.H., "The Evolution of Porosity During the Combustion of Char: The fractal Approach and the Statistic Description," In: *Twenty-Second Symposium on Combustion*, The Combustion Institute, , 39-45, (1988)

Dunlop, A. P., and Peters, F. N., *Industrial and Engineering Chemistry*, 34, 814 (1953).

Erickson, T. A. *The Fate of Flame Volatilized Sodium During the Combustion of Pulverized Coal in Reaction with Silica and Sulfur (Studied with the Aid of a Synthetic Coal)*, M.S. Thesis, University of North Dakota (1990).

Erickson, T. A. *The Role of Sodium and Sulfur in High Temperature Reaction with Silica Particles*, Senior Honors Thesis, University of North Dakota (1988).

Fairbridge, C., Ng, S. H., and Palmer, A. D., "Fractal Analysis of Gas Adsorption on Syncrude Coke," *Fuel*, 65(12), 1759-1762 (1986).

Farin, D., Avnir, D. and Pfeifer, P., "Fractal dimensions of surfaces. The use of adsorption data for the quantitative evaluation of geometric irregularity," *Particulate Science and Technology* 2, 27-35, (1984)

Farin, D., Peleg, S., Yavin, D. and Avnir, D., "Applications and limitations of boundary-line fractal analysis of irregular surfaces: Proteins, aggregates, and porous materials," *Langmuir* 1, 399-407, (1985a)

Farin, D., Volpert, A., and Avnir, D., *Journal of the American Chemical Society*, 107, 3368, 5319 (1985b).

Fitzer, E., Schaefer, W. and Yamada, S., "The Formation of Glasslike Carbon by Pyrolysis of Polyfurfuryl Alcohol and Phenolic Resin," *Carbon*, 7, 643-648 (1969).

Fripiat, J.J., Gatineau, L. and Van Damme, H., "Multilayer physical adsorption on fractal surfaces," *Langmuir* 2, 562-567, (1986)

Gregg, S. J., and Sing, K. S. W., *Adsorption, Surface Area and Porosity, 2nd Edition*, Academic Press, New York (1982).

Jabkhiro, E. H., and Delfosse, L., "The Evolution of Porosity During the Combustion of Char, The Fractal Approach and the Statistic Description," 22th International Symposium on Combustion, The Combustion Institute, Pittsburgh, PA (1988).

Levendis, Y. A. and Flagen, R. C., " Combustion of Uniformly Sized Glassy Carbon Particles," *Combustion Science and Technology*, 53, 117-136 (1987).

Ludlow, D. K. and Moberg, T. P., "Technique for Determination of Surface Fractal Dimension Using a Dynamic Flow Adsorption Instrument," *Analytical Instrumentation*, 19(2&3), 113 (1990).

Mandelbrot, B. B., *The Fractal Geometry of Nature*, W. H. Freeman & Co, New York (1982)

Mandelbrot, B. B., *Fractals - Form, Chance, and Dimension*, W. H. Freeman & Co, San Francisco (1977)

Marsh, H., and Siemieniewska, T., "The Surface Areas of Coals as Evaluated from the Adsorption Isotherms of Carbon Dioxide using the Dubinin-Polanyi Equation," *Fuel*, 44(5), 355-367 (1965).

McClellan, A. L. and Harnsberger, H. F., "Cross-sectional Areas of Molecules Adsorbed on Solid Surfaces, " *Journal of Colloid and Interface Science*, 23, 577-599 (1967).

McEnaney, B., "Adsorption and structure in Microporous carbons," *Carbon* 26(3), 267-274, (1988)

195

Meyer, A. Y., Farin, D. and Avnir, D., *Journal of the American Chemical Society*, **108**, 7897 (1986).

Mills, M.E., *Sodium Release from Solids in Flames Studied using Laser Induced Flourescence Spectroscopy*, Ph.D. Thesis, University of North Dakota (1989)

Moberg, T.P., *The Fractal Analysis of Catalytic Glass Fabrics*, M.S. Thesis, University of North Dakota, Grand Forks, ND (1990)

Ng, S. H., Fairbridge, C., Kaye, B. H., "Fractal Description of the Surface Structure of Coke Particles," Langmuir, The ACS Journal of Surface and Colloids, **3**(3), 340-345 (1987).

Pfeifer, P., "Fractal dimension as working tool for surface-roughness problems," In: *Applications of Surface Science, Vol. 18*, edited by Park, R.L., North-Holland Physics Publishing, Amsterdam, The Netherlands, 146-164, (1984)

Pfeifer, P., and Avnir, D., "Chemistry in Noninteger Dimensions between Two and Three. I. Fractal Theory of Heterogeneous Surfaces," *The Journal of Chemical Physics*, **79**(7), 3558-3565 (1983).

Pfeifer, P., Avnir, D., and Farin, D., "Ideally Irregular Surfaces, of Dimension Greater Than Two, in Theory and Practice," *Surface Science*, **126**, 569-572 (1983).

Pfeifer, P., Avnir, D., and Farin, D., "Scaling Behavior of Surface Irregularity in the Molecular Domain: From Adsorption Studies to Fractal Catalysts," *Journal of Statistical Physics*, **36**(5/6), 699-716 (1984).

Riesz, C. H. and Susman, S. *Procedings of the 4th Carbon Conference*, Pergamon Press, Oxford, 621 (1960).

Schmitt, J. L., *Carbon Molecular Sieves as Selective Catalyst Supports*, Ph.D. Thesis, Pennsylvania State University (1976).

Senior, C. L., *Submicron Aerosal Production During Combustion of Pulverized Coal*, Ph.D. Thesis, California Institute of Technology (1984).

Senior, C. L. and Flagan, R. C., "Synthetic Chars for the Study of Ash Vaporization," *Twentieth Symposium (International) on Combustion*, The Combustion Institute, 921-929 (1984).

Sondreal, E. A., Tufte, P. H., and Beckering, W., "Ash Fouling in the Combustion of Low-Rank Western U.S. Coals," *Combustion Science and Technology*, **16**, 95 (1977).

Van Damme, H.; and Fripiat, J. J., "A Fractal Analysis of Adsorption Processes by Pillared Swelling Clays," *The Journal of Chemical Physics*, **82**(6), 2785-2789 (1985).

Van Vliet, B.M. and Young, B.D., "The use of fractal dimension to quantify the effect of surface roughness on film mass transfer enhancement," *Chem. Eng. Comm.* **69**, 81-94, (1988)

Vosen, W. M. *Fractal Dimension Analysis of Fly Ash Development from Char Combustion*, Senior Honor Thesis, University of North Dakota (1990).

Weswerka, E. M., Walters, K. L. and Moore, R. H., "Differential Thermal Analysis of Furfuryl Alcohol Resin Binders," *Carbon*, **7**, 129-141 (1968).

Wibberly, L. J. and Wall, T. F., "Alkali-Ash Reactions and Deposit Formation in Pulverized-Coal-Fired Boilers: The Thermodyamic Aspects Silica, Sodium, Sulfur, and Chlorine," *FUEL*, **61**, 87-92 (1982).

Wilkie, A. M. *Fractal Dimension Analysis of Carbon Fiber Composites*, Senior Honors Thesis, University of North Dakota (1990).

Zygarlicke, C. J.; Benson, S. A.; Abrahamson, H. B.; Mills, M. E., *Department of Energy Annual Report*, DOE-DE-FC21-86MC10637 (1989)

Run	Combustion Temperature (K)	Residence Time (sec)	Sample Size (g)	Mineral[A] Diameter (mm)	Carbon[B] Loss (%)	BET Surface[C] Area (m^2/g)	Fractal Dimension D	Prefactor K (A^D cm^3 STP)
1	Synthetic Coal	-	0.6319	3.84	0.0	49.0 ± 1.6	1.89 ± 0.49	9.35 ± 2.18
2	Synthetic Coal	-	0.6576	3.84	0.0	51.5 ± 1.4	2.10 ± 0.28	10.69 ± 2.10
3	1173	0.1	0.6142	4.04	14.3	55.1 ± 1.3	2.70 ± 0.83	16.05 ± 2.31
4	1173	0.5	0.1568	4.06	66.5	124.7 ± 3.3	2.85 ± 0.30	22.67 ± 2.11
5	1173	1.5	0.1816	27.0[E]	100	121.4 ± 3.1	2.47 ± 0.72	16.86 ± 2.26
6	1773	0.1	0.3089	5.06	48.7	110.4 ± 3.0	2.81 ± 0.46	21.79 ± 2.17
7	1773	0.5	0.0253	4.20	83.5	(5.6 ± 0.5)[F]	1.98 ± 1.15	3.26 ± 2.30
8	1773	1.5	0.3071	8.50[E]	100	(0.8 ± 0.1)[F]	2.26 ± 1.84	1.78 ± 2.48

[A] Determined using CCSEM
[B] Determined using TGA
[C] Nitrogen Adsorption data at 77 K
[E] Average diameter of coalesced fly ash particles
[F] Insufficient sample size to accurately determine surface area
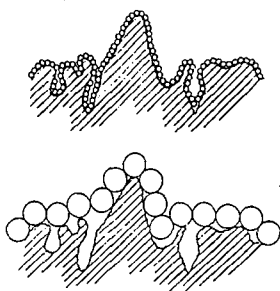
Figure 1. Pictorial representation of fractal dimension analysis.

BET Plot – Sample 3 Nitrogen
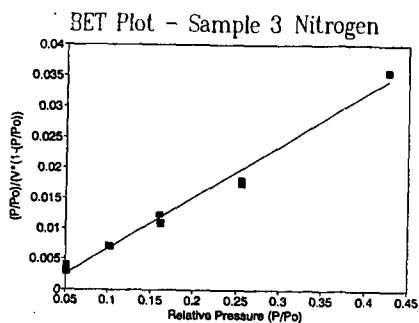
Figure 2. Example of BET plot used to determine monolayer volume adsorbed (V_m).

Synthetic Coal #2
Fractal Dimension = 2.10
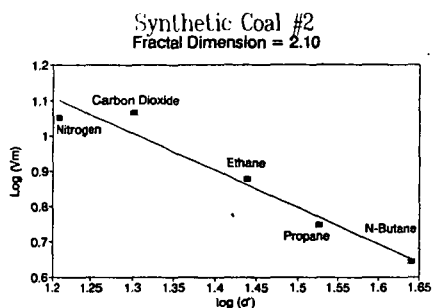
Figure 3. Example of fractal dimension plot used to determine the fractal dimension, D, and the lacunarity.

Fractal Dimension versus Carbon Loss
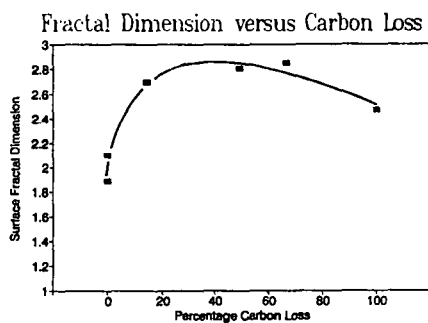
Figure 4. Surface fractal dimension versus carbon loss during char combustion.

Prefactor versus Carbon Loss
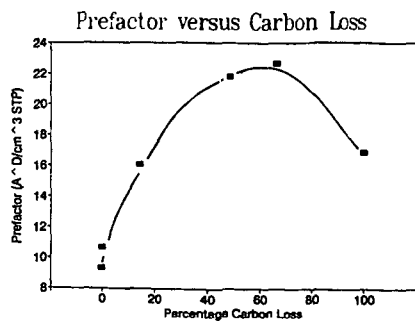
Figure 5. Lacunarity versus carbon loss during char combustion.

198

PERFORMANCE CHARACTERISTICS OF AN MHD
PILOT PLANT ELECTROSTATIC PRECIPITATOR

J. S. Lindner, P. R. Jang, W. P. Okhuysen
Diagnostic Instrumentation and Analysis Laboratory
Mississippi State University
Mississippi State, MS 39762
and
J. K. Holt
Energy Conversion Program
University of Tennessee Space Institute
Tullahoma, TN 37388

INTRODUCTION

In magnetohydrodynamic (MHD) power generation a seed material, normally K_2CO_3, is added to enhance the conductivity of the coal-fired gas stream. The plasma is passed through a magnetic field and electricity is produced by the Hall effect. Future large scale MHD facilities are expected to be more efficient than conventional coal-fired power plants not only because of the DC electricity produced but also from increased heat recovery owing to the large (3000 K) combustion temperatures employed.

There is, however, a finite cost for the seed material and the resulting K_2SO_4 particles (SO_2 emissions are minimized by combination with seed potassium) must be collected, converted back to K_2CO_3 or KCO_2H, and recycled back to the combustor. Although estimates vary it is well recognized that a large portion ($\geq 95\%$) of the spent seed must be recycled for viable economic operation.[1]

The performance characteristics of the MHD electrostatic precipitator (ESP) are therefore of interest. As an added condition recent experimental and theoretical studies of K_2SO_4 homogeneous nucleation[2] have indicated that these particles grow to Sauter diameters of between 1 and 1.2 μm. These sizes are in a range where ESP performance may be degraded.[3]

In this work, we describe Mie scattering and electric field measurements on an MHD pilot scale ESP located at the Coal Fire Flow Facility (CFFF) at the University of Tennessee Space Institute. Results are reported for the determination of near-real-time collection efficiencies, the variation of the ESP performance with seed percentage, and initial studies on the extent of particle re-entrainment.

EXPERIMENTAL

The theoretical framework for determination of the Sauter mean diameter, D_{32}, using two-color laser transmissometry has been reported previously.[4,5] Briefly, transmissions ($T = I/I_o$) measured at two well-separated monochromatic wavelengths (λ_1, λ_2) are related to an extinction efficiency ratio which is proportional to D_{32}

$$\frac{\ln T(\lambda_2)}{\ln T(\lambda_1)} = \frac{\overline{Q}_2}{\overline{Q}_1} \sim D_{32} \tag{1}$$

Mie theory is used to calculate the variation of $\overline{Q}_2/\overline{Q}_1$ (bars indicate averages over a distribution) on D_{32}. For the case of a polydisperse particle size distribution (PSD) $\overline{Q}$ is expressed in terms of an effective extinction cross section, $\overline{\sigma}_e$ and an assumed distribution

199

$$\overline{Q} = \int_o^\infty \overline{\sigma}_e fn(r)dr/\pi \int_o^\infty r^2 fn(r)dr \qquad (2)$$

where $\overline{\sigma}_e$ is calculated from the theory with knowledge of the complex refractive index, m.

The theoretical response curve used to interpolate D_{32} from the measured transmissions (insert Figure-1) is generated by scaling the assumed PSD. Each distribution corresponds to a unique D_{32} value. The effect of the PSD shape on D_{32} has been determined by sensitivity studies[6] to be within -2% or +9% of the integrated D_{32} value. This result is consistent with the fact that D_{32} is, by definition, a z-average quantity.

Studies have also been carried out on the effect of the complex refractive index on D_{32}[6]. Using the reported values[4] of m for Illinois #6 and Montana Rosebud with and without spent seed (K_2SO_4) and the m value for K_2SO_4 it was determined the D_{32} varies by $\pm 0.1\mu m$. The above result has some implications on the work reported here as the chemical composition of the particles[7] entering the CFFF ESP are about 85% K_2SO_4 with the remainder flyash. Thus the use of the complex refractive index for K_2SO_4 is not expected to have a significant effect on the Sauter diameters determined.

Although the primary observable in two-color extinction measurements is D_{32} additional information concerning mass and number loading can be obtained. Number densities, C_n values, are available from Beer's law

$$T(\lambda) = \exp(-l\overline{\sigma}_\lambda C_n) \qquad (3)$$

where 1 is the effective optical path length. The mass density C_m is related to C_n through the chemical density, d, of the particles and the volume density, C_v

$$C_m = dC_v = (d 4\pi r_{32}^3 C_n)/3 \qquad (4)$$

Electron micrographs of particles collected downstream of the CFFF superheater indicate spherical shape.[7]

The optical configuration of one of the two-color laser transmissometer (TCLT) units is shown in Figure 1. The second optical unit is similar to that shown with the exception that only two lasers, an argon ion ($\lambda = 0.488$ or $0.5145\mu m$) and a helium-neon ($\lambda = 3.39\mu m$) are used. For the efficiency measurements both units were interfaced to the microprocessor unit. Because of a small but finite time delay of 100 ms (the processor collects raw intensities from one optical unit followed by the intensities from the second unit) the measurements reported here are classified as nearly simultaneous. For the experiments on rapid temporal response the microprocessor unit was replaced by an IBM PC/AT type microcomputer with an analog to digital board.

Electric field meter (EFM) measurements were performed using a laboratory built unit similar to that reported by Castle et al.[8] The field was sensed by four circular electrodes whose signals were modulated using a 4-hole chopper wheel powered by an air motor. Laboratory experiments indicated that the output of the meter was constant to within ± 1 mv over the frequency range from 220 to 270 hr. Initially the meter was calibrated[9] using parallel plates where

$$E = V/D \qquad (5)$$

Here E is the electric field, V the applied plate voltage and D the distance between the meter and the charged plate. Knowledge of the duct geometry permits the solution of Poisson's equation for the space charge density, ρ. Expressions for E in terms of ρ for cylindrical[8] and rectangular[10] ducts have been reported. Calculations for the trapezoidal exit duct of the CFFF ESP have not yet been performed; consequently, only raw voltages are reported here. These data are, however, directly related to ρ which is usually expressed in C/m^3 units. Each particle exiting the ESP will carry some charge, q, thus ρ/q yields a measure of number concentration. Results from the EFM are then comparable to the scattering method but also provide the charge density which is an important parameter in models of electrostatic precipitation.[11]

Location of the TCLT units and the EFM with respect to the CFFF ESP is given in Figure - 2. Experiments reported here correspond to facility tests LMF4-N, LMF4-S and LMF4-U. Near-real-time collection efficiencies determined during LMF4-N were calculated from the penetration, P

$$P = \left(\frac{Cn(out)}{fCn(in)} \right) (100) \qquad (6a)$$

$$Efficiency = 100 - P \qquad (6b)$$

in the above equation f is that fraction of the total flow diverted to the ESP. The values of f were taken from the CFFF records where information on the electrical conditions of the ESP, temperatures, vibrator and plate-rapping frequencies and other pertinent conditions are collected.

RESULTS AND DISCUSSION

As stated previously, the behavior of the MHD ESP is critical to the successful economic operation of the facility. The three studies below represent only a fraction of the results collected to date. The data on efficiency and the performance of the ESP as a function of the ratio K_2/S have practical bearing on future commercial scale facilities. The final study concerns our initial efforts to characterize rapid temporal variations of ESP performance and the application of the field meter.

Near - Real - Time Efficiency Measurements - Average Sauter diameters determined upstream of the ESP are collected in Figure - 3. An average of 1.2 μm was calculated. Measurements on May 6 and 7 yielded D_{32} values of 1.18 and 1.25 μm respectively. Average number densities were 5.6, 4.8 and 4.2 x 10^6 cm^{-3}.

Extinction measurements downstream of the ESP permit the application of Eq. 6. Corresponding efficiency values are presented in Figure - 4. To our knowledge this data represents the first reported determination of near - real - time efficiencies for an electrostatic precipitator. In this regard it should be noted that the application of standard sample extraction methods can only provide an estimate of the efficiency since the sampling times before and downstream of the ESP will not be the same. Additionally, any changes in facility operation cannot be quantified rapidly.

Although some scatter is observed in Fig. 4 the majority of efficiencies lie above 90% with many values larger than 95%. The radical decrease in efficiency between 1348 and 1408 hours corresponds to a baghouse cleaning cycle. During this process the flow normally partitioned to the fabric filter device was diverted to the ESP, thereby increasing the flow by approximately 5000 cfm. The decrease in efficiency, albeit of short duration, indicates that the ESP cannot completely

adjust to the additional mass loading. This result is expected based on the flow entering the device, 16,400 cfm compared to the design set point of about 8600 cfm.[12]

Some comments are required concerning the factor f appearing in Eqs. 6. Using C_n values of 2.5 x 10^5 (outlet) and 5.98 x 10^6 cm^{-3} (inlet) it is possible to determine the effect of errors in the mass flow on the efficiency. For the data in Fig. 4 (excluding the cleaning cycle) the flow to the ESP was measured as 11,000 cfm. The flow to the baghouse was 5400 cfm and the calculated efficiency was 94.3%. Assuming flows to the ESP of 9000 and 13,000 cfm yielded efficiencies ranging from 93 - 95.2% or a difference of slightly larger than 2%. So long as the flow rate to the ESP is known to within 20% the calculation of the efficiency is adequate.

Effect of the Ratio K_2/S - Initially feed rates to the MHD combustor were controlled to provide sufficient K atoms for plasma enhancement and the total conversion of SO_2 to K_2SO_4. Recently it has been noted that generator power levels could be increased by overseeding.[13] This practice led to variations in the performance of downstream components as noted by increased bridging in the platen superheater and decreased ESP performance[14] presumably due to K_2CO_3 or other K species.

Measurements of the particle size and loading downstream of the CFFF ESP were conducted at different K_2/S (molar ratio of K in seed to S in coal) ratios during facility test LMF4-S. Figure - 5 illustrates Sauter diameters for time periods corresponding to different K_2/S ratios. Clearly, as the K_2CO_3 percentage decreases the D_{32} values increase.

During these measurements the facility conditions such as gas stream temperatures, soot blowing frequency, total coal flow and combustion stoichiometry, etc. were reasonably constant. The mass flow rates to the ESP were approximately 6000 cfm for the data in panels A and B and 7800 cfm in panel C. The previous efficiency results indicate that as the mass loading is increased (i.e. fabric filter cleaning cycles) the efficiency decreases. This corresponds to an increase in C_N (or a decrease in D_{32}, Eqs. 1 and 3) at the downstream location. The fact that D_{32} is increased at the K_2/S ratio of 1.04 (Fig. 5 panel C) indicates that the excess K_2CO_3 (panels A and B) has a significant effect on ESP performance.

The decreased ESP performance at large K_2/S ratios may indicate that the K_2CO_3 particles are nucleating to smaller particle diameters than K_2SO_4. Changes in particle resistivity do not appear to be responsible for the observed behavior. Further studies are in progress.

Initial Studies of ESP Temporal Performance - The standard means of characterizing ESP operation involves the extraction of sample, preferably isokinetically, from the gas stream. The extraction requires some time and, thus, events occurring over periods of seconds or even minutes cannot be quantified. Such events are thought to be those due to collection plate rapping and the vibration of the wire racks. Experiments were initiated to evaluate the extent of particle re-entrainment from the CFFF ESP.

For these experiments conducted during test LMF4-U the electric field meter (EFM) was installed at the exit duct of the ESP and the TCLT was located slightly downstream. The K_2/S ratio was held constant at 1.0. Figure 6 illustrates the average Sauter diameters (top trace) and the raw EFM signal (lower trace) over a typical collection period. The average particle size is similar to that observed in panel C of Fig. - 5. Of interest in Fig. 6 is the increase in field meter voltage and the decrease in D_{32} observed at approximately 1217. The locations of the peaks are shifted relative to one another owing to the fact that the computer clocks were not synchronized (the residence time between the instrument locations has been calculated at 1 sec.).

Examination of the facility data records led to the assignment of the increase in C_N to the vibration of the field 4 wire rack. Although there could be similar information on the effects of the vibrators for fields 1, 2 and 3 as well as on plate rapping the noise in the data precludes unequivocable assignment. The apparent lack of particle re-entrainment from rapping may arise from the 2 min. frequency for this process. Further studies wherein the frequency of rapping and wire rack vibrating are varied are in progress.

CONCLUSIONS

Our studies of the CFFF pilot plant ESP have yielded some valuable information concerning the performance of the component under different MHD facility operating conditions. To our knowledge, this is the first report of the determination of ESP efficiency in near-real-time. Studies on the ratio K_2/S indicate that ESP performance degrades as the ratio is increased. Work is in progress to further quantify this effect and to establish the conditions for efficient ESP operation at overseeding conditions. Initial temporal studies conducted downstream of the ESP indicate that particle re-entrainment from vibration of the wire racks is more pronounced than increased emission from collection plate rapping.

ACKNOWLEDGEMENTS

REFERENCES

1. Petrick, M.; et al., in Open Cycle Magnetohydrodynamic Electrical Power Generation, M. Petrick and B. Ya Shumyatsky, eds. Argonne National Laboratory, Argonne, IL (1978).
2. Wang, C. and Lindner, J. S., J. Prop. Pow. 6, 552 (1990).
3. ASHRAE Handbook - Equipment, American Society of Heating, Refrigerating and Air Conditioning Engineers Atlanta, GA (1988).
4. Ariessohn, P. C., HTGL Report No. 119, Stanford University, Stanford CA(1980).
5. Dobbins, R. A. and Jizmagian, G. S., J. Opt. Soc. Am. 56, 10 (1966).
6. Lindner, J. S.; et al., Proceedings of the 27th Symposium on the Engineering Aspects of Magnetohydrodynamics p. 8.5.1 Reno NV. (1988)
7. Holt, J. K. et al., Proceedings of the 25th Symposium on the Engineering Aspects of Magnetohydrodynamics p. 8.2.1, Bethesda, MD (1986).
8. Castle, G. S. P.; et al. IEEE Trans. Ind. Appl. 24, 702 (1988).
9. Blitshteyn, M. Eval. Eng. p. 70 Nov. (1984).
10. Carruthers, J. A. and Wigley, K. J., J. Inst. Pet. 48, 180 (1962).
11. Lawless, P. A. and Sparks, L. E., IEEE Trans. Ind. Appl. 24, 922 (1988).
12. Morehead, B. K. and Foote, J. P., Proceedings of the 23rd Symposium on the Engineering Aspects of Magnetohydrodynamics p. 585 Somerset, PA (1984).
13. Stepan, I. E.; et al., Proceedings of the 28th Symposium on the Engineering Aspects of Magnetohydrodynamics p. 1.1-1, Chicago IL (1990).
14. Attig, R. C.; et al., Proceedings of the 27th Symposium on the Engineering Aspects of Magnetohydrodynamics p. 1.2-1 Reno NV (1989).
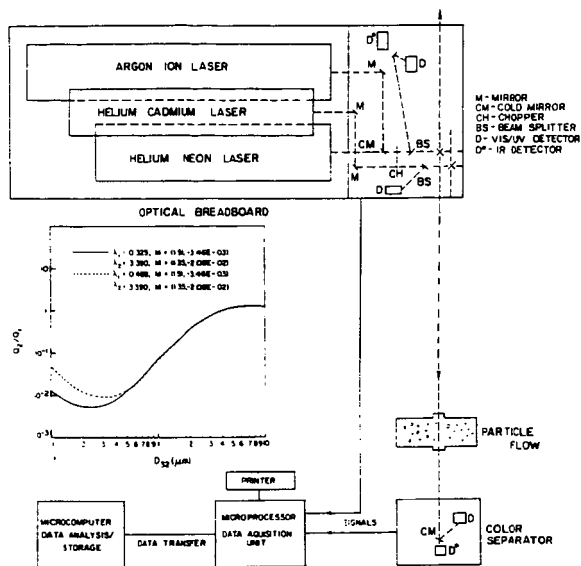
Figure 1. Experimental configuration and theoretical response curve
for the Two-Color Laser Transmissometer.
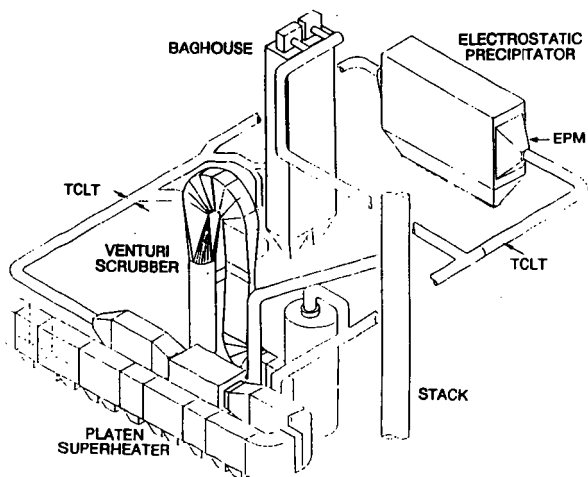
Figure 2. Instrument locations with respect to the downstream facility
components of the Coal-Fired Flow Facility.
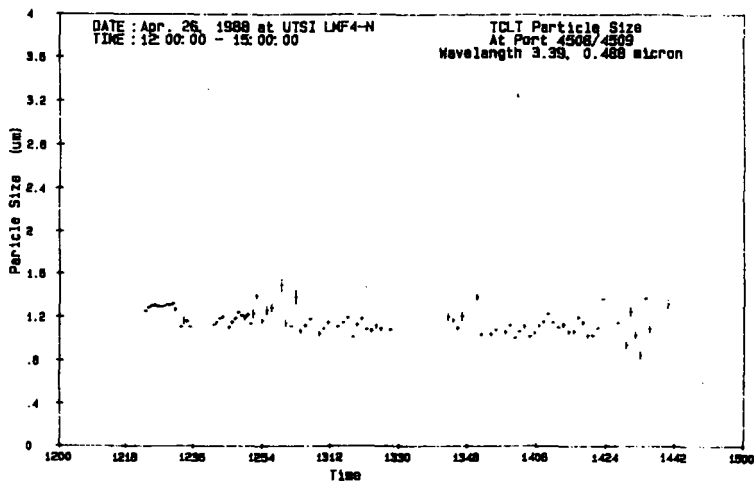
Figure 3. Average particle sizes (D_{32} values) at the baghouse/ESP inlet.
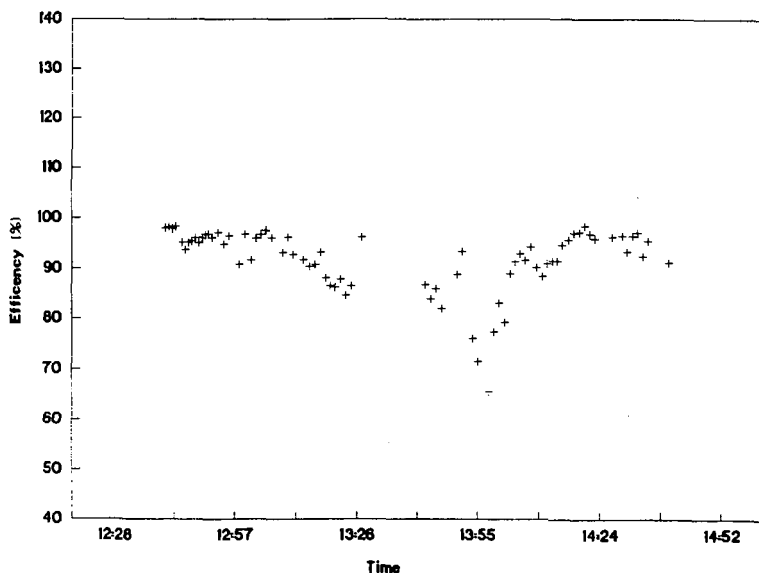
Figure 4. Near-real-time ESP efficiencies measured during LMF4-N. The decrease in efficiency around 1355 corresponds to a baghouse cleaning cycle with all flow diverted to the ESP.

205
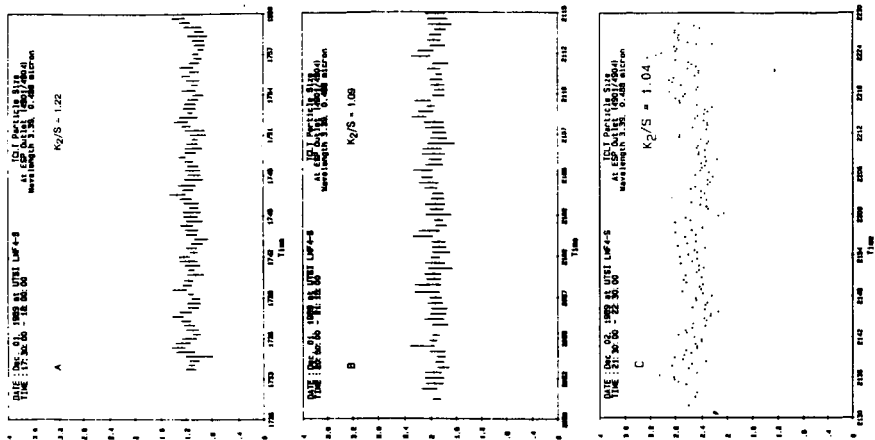
Figure 5. Average Sauter diameters measured at the outlet of the ESP during
facility test LMF4-S. Values of the ratio K_2/S decrease
in going from panel A to panel C.
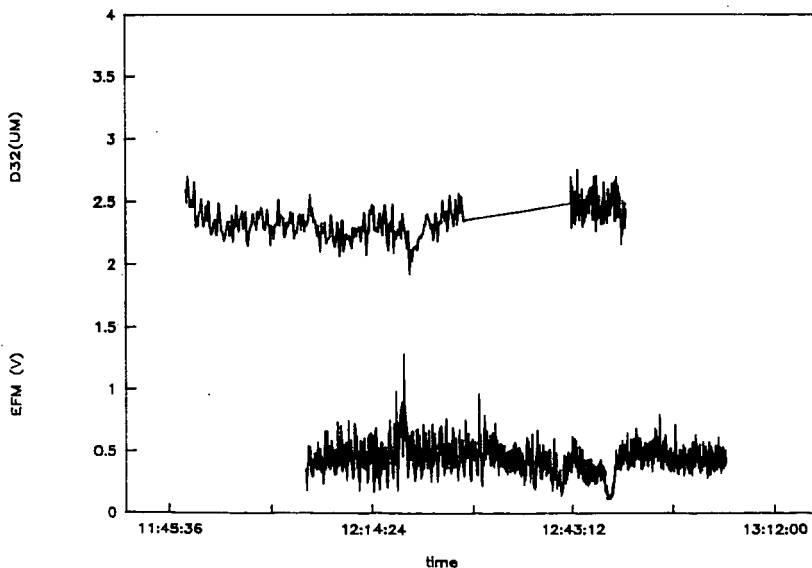
Figure 6. Average Sauter diameter (top trace) and EFM voltage measured during
facility test LMF4-U. The decrease in D_{32} and increase in EFM voltage
corresponds to particle re-entrainment originating from
vibration of the field 4 wire racks.

206

CHEMICAL PHASES IN PETROLEUM COKE GASIFICATION SLAG

John C. Groen and James R. Craig
Department of Geological Sciences, Virginia Polytechnic Institute & State University,
Blacksburg, VA 24061-0420

Mitri S. Najjar
Texaco Research Center, Box 509, Beacon, NY 12508

ABSTRACT

The gasification of petroleum coke results in the generation of complex slags. The broad variability in the physical and chemical properties of these slags will be described. The slags were examined primarily by means of reflected light optics using standard polished sections. These sections were also used directly for electron microprobe analysis where quantitative data on elemental distribution and partitioning was gathered and will be presented. Scanning electron microscopy (SEM) techniques were also used to characterize the presence of numerous phases including spinels of variable composition, glass droplets of variable composition, iron sulfide/oxide intergrowths often with tiny Fe-Ni alloy grains, and calcium silicates.

INTRODUCTION

The Texaco partial oxidation gasification process makes use of petroleum coke to produce a synthesis gas for use as a fuel for power generation or process heat, a chemical feedstock, or as a reducing gas. The petroleum coke feedstock is reacted with a controlled, sub-stoichiometric quantity of oxygen in a fuel rich, exothermic reaction. The process is carried out in a pressurized reaction chamber at 2200-2600°F (1200-1450°C), which promotes efficient reaction and facilitates the formation of a partially to wholly molten slag by controlling the feed rates of the reactants. The feeds are introduced together, through the top of the gasifier, and pass through it concurrently with the product gases transporting the solids, making it an entrained flow gasifier. The slags that form in the gasifiers result from the accumulation of residual, noncombustible elements either on the refractory linings of the gasifiers, or as droplets that fall into water quench baths.

The slags produced during the high temperature gasification of petroleum coke can be generally characterized into three principal types: 1.- relatively fluid homogeneous silicate melts that solidify on cooling to brownish-black glass with minor to significant amounts of sulfide droplets, spinel crystals $(Fe,Mg,Ni)^{2+}(Fe,Al,V,Cr)_2^{3+}O_4$, plus other minor phases; 2.- sulfide dominant slag of generally troilitic composition (FeS), frequently but not always symplectically intergrown with wüstite (FeO), and usually containing smaller amounts of native Fe-Ni alloy grains, spinels (as above), glass droplets, and other phases; 3.- highly viscous slags comprised of masses of coarse interlocking vanadium-oxide-rich crystals, with major amounts of CaV_2O_6, $(Fe,Ca)VO_4$ or $CaFeV_2O_7$, VO_2, spinels (as above), glass droplets, plus other minor phases. These generalized compositions are shown in Table 1, which also lists in more detail the specific nature of some of the minor phases observed.

CHEMICAL PHASES

Spinels are both the most ubiquitous and the most compositionally variable crystalline phase. Hence it is instructive to consider the potential structural site occupancies and the degree of partitioning that the spinels exhibit with coexisting phases. The most apparent spinel compositional trend, as shown in Figure 1, is that which exists among spinels hosted by Ca-Fe-V oxides. Most of these spinels lie in the Ni to Mg, Al-V-(Fe^{3+}+Cr) prism, and cluster toward the Al-rich corner. These spinels commonly contain more than 20 mol% Ni in the 2+ site, and some contain more than 80%. In contrast, the spinels in sulfide-rich slags tend to be Ni-poor; the Ni in such slags concentrates in the Fe-Ni-S monosulfide solid solution and in the Fe-Ni alloy.

The spinels in FeS-FeO-rich, glassy, and Ca-Fe silicate-rich slags are in general considerably more V-rich (Fig. 2) than are the spinels in Ca-Fe-V oxide-rich slags where the V is more highly partitioned into the host phases. The lower V contents of the spinels in Figure 1 is compensated by increases in the Al and Fe^{3+}+Cr contents. The scarcity of Fe^{2+} in these spinels implies that the oxidation potential at the time of slag generation was high enough to keep most of the iron in the Fe^{3+}

state; this is also supported by the observation that the vanadium in the coexisting Ca-Fe-V oxides is all present as V^{4+} and V^{5+}.

Spinels that occur in the sulfide rich slags (Fig.'s 2a-c) exhibit a fairly tight clustering of compositions that are relatively Fe^{2+} and V-rich and Al-poor. The enrichment of these spinels in Fe^{2+} is obviously due to the abundant available reduced iron in the Fe-S-O melt. Vanadium, as a general rule, partitions out of Fe-S-O melts, however, residual V that is present, clearly prefers filling 3+ sites, and then 2+ sites in spinel to forming V-sulfides. Strong verificaton of this phenomenon comes from the common observation of V-bearing spinels occurring in V-deficient Fe-Ni sulfides. The efficacy of V-partitioning into spinels is so strong, in fact, that even when present as V^{2+}, the V ions still enter spinel structures preferentially to forming sulfides as analyzed in several samples. Furthermore, only one sample of slag was found to contain V-rich sulfides, and in that sample, the euhedral spinels had already been virtually saturated with V, such that their compositions were essentially that of the pure endmember V_3O_4 (unplottable in Figure 2, and unknown as a mineral), leaving no oxygen for the additional V to react with, instead only sulfur. The oxidation state present during the formation of this slag must have been unusually low to facilitate the formation of V-sulfides. The low Al content of many of the spinels in the sulfide-rich slags (Fig. 2b), no doubt results from the virtually complete exclusion of Al from Fe-S-O melts. The relative deficiency of Mg in these spinels (Fig. 2c), can most likely be explained by a similar argument. The sulfide-rich slags also contain an interesting spinel with a rather unique composition approaching that of the mineral coulsonite (FeV_2O_4).

Glass-rich chunks of slag contain variable to large quantities of sulfide droplets, and thus form a continuum of slag types between sulfide-rich and glass-rich. This is probably the main reason that the spinels within glass hosts are compositionally similar to spinels within sulfide hosts. The primary compositional difference between these two groups is the Al-content (Fig. 2b), which is considerably higher in the glass-hosted spinels. Such a variation would be expected, because of the relatively high Al-content of the glasses, where Al substitutes for Si. The analyses of glass-hosted spinels that plot on or near the V - Fe^{3+}+Cr join, are of spinels in sulfide-droplet-rich glassy slags (as described above), suggesting that these spinels experience compositional influences from both sources. The "ideal" glass hosted spinel composition, therefore, appears to be represented by the higher Al-content points shown in Figure 2b. The anomalous, isolated group of V-poor, and Fe^{3+}+Cr-rich spinels in the glass-hosted family are unusually Cr-rich, and are interpreted to result from reaction with the refractory brick in the gasifiers.

Only a few pieces of slag have been found which contain significant quantities of crystalline Ca-Fe silicates; hence any discussion of the composition of their associated spinels is very preliminary. The highly variable V-content of all the spinels (and probably of the slags in general) most likely reflects the variable nature of the source petroleum for the feed cokes. Many crude oils are naturally enriched in V (carried as organic porphyrin complexes), as a result of the type of source materials and source rocks from which the oil was derived. Ni is another common element in petroleum and is also carried in large part as porphyrin complexes; hence its abundance in the slags may also be largely a function of its source crude. The Fe, Al, Si, Mg, Ca, Na, and S found in the slags are derived primarily by residual accumulation of minute entrained mineral particles (such as clays, Fe-oxides, Fe-sulfides, etc.) and hence tend not to vary considerably from slag to slag because of the common, but variable occurrence of these minerals. Chromium contents of petroleum are very low, hence, most of the Cr found in the slags probably originates from reaction of the molten slag with the Cr-rich refractory brick lining the gasifiers. The elemental Cr-content of most of the spinels is generally less than 15 mol%; and as of yet has not been found to show any relationship to host slag type.

The dominant sulfide phase found in the petroleum coke gasification slags is troilite (FeS). This composition may, however, grade from pure FeS to that of hexagonal pyrrhotite ($Fe_{1-x}S$, 0.0<x≤~0.125) as shown in Figure 3. Distinguishing the compositions of these phases by means of electron microprobe analysis is quite difficult, and is better accomplished (if sufficient quantities exist), by X-ray diffraction, TEM, or other such techniques. The iron-sulfide often occurs as a very fine symplectic intergrowth with iron oxide (presumably wüstite, FeO), that can barely be resolved by optical techniques. These intergrowths appear to be the result of the rapid cooling of an initially homogeneous Fe-S-O melt; such melts cannot be quenched to glasses. Nickel can substitute for iron in pyrrhotite in minor amounts, but may also form a discrete Ni-sulfide phase (Heazlewoodite, Ni_3S_2) and an Fe-Ni-sulfide phase (Pentlandite, $(Fe,Ni)_9S_8$). The crystals/grains of free metal (F.M.) that form in the sulfide matrix generally contain iron plus 10 to 28 atomic percent Ni but have been found to range from pure Fe to more than 70 atomic percent Ni (Fig. 3). In addition to the Fe-monoxide wüstite phase observed in the sulfide bearing slags, NiO (bunsenite) has also been found as well as a few grains of mixed (Fe,Ni)O composition.

Vanadium oxide rich slags have been found to contain at least five distinct V-bearing phases. One

208

is CaV_2O_6 which is not known as a mineral but has been synthesized in phase equilibria studies. Euhedral Na-V-oxide crystals of apparent stoichiometry equal to NaV_6O_{15} occur with CaV_2O_6 crystals, and correspond well with a ß-solid solution phase along the experimental Na_2O-V_2O_5 join. This experimental ß-solid solution phase has been found to be in equilibrium with CaV_2O_6 at 650°. A third phase, which occurs with the two phases above, has an apparent chemical formula of $NaCaV_8O_{20}$; this phase, however, does not correspond to any phases known from the literature. A fourth V-phase which is quite common, is problematic in that it is most favorably represented as a Ca-bearing variety of the synthetic $FeVO_4$ phase, from charge balance considerations; yet it is conceptually difficult to imagine a Ca ion substituting for Fe^{3+} in the structure. Alternatively, this phase might be a hypothetical $CaFeV_2O_7$ phase extrapolated from such known phases as $Ca_2V_2O_7$ and $Ni_2V_2O_7$; however, $CaFeV_2O_7$ does not charge balance well, and, the coexistence of Fe^{2+} and V^{5+} in the same structure may be unlikely. A fifth and less common V-phase is VO_2. VO_2 is known as the mineral paramontroseite, however, this mineral forms as a metastable, low temperature oxidation product of the mineral montroseite and is a polymorph of synthetic VO_2. The euhedral VO_2 crystals we observe in the slags grew at high temperatures and are therefore most likely not paramontroseite, but instead equivalent to its synthetic, high temperature polymorph. Spinels and variable composition glasses are the other main constituents of this type of slag; many additional minor phases occur in this type of slag as listed in Table 1.

The sulfide-dominant slags occasionally contain pieces of slag which have several different euhedral Ca,Mg,Fe ± Na silicates worth noting. Though still in need of further verification, some of the phases have tentatively been identified as Akermanite ($MgCa_2Si_2O_7$, observed= $(Mg,Fe)Ca_2(Si,Al)_2O_7$), Fayalite (Fe_2SiO_4, observed=$(Fe,Mg,Ca,Na)_2(Si,Al)O_4$), and Pigeonite ($(Mg,Fe,Ca)(Mg,Fe)Si_2O_6$, observed=$(Ca,Fe,Mg,Na)(Mg,Fe)(Si,Al)_2O_6$). These phases are well known in geological realms and should be useful for estimating the conditions under which crystallization occurred.

TABLE 1.

SLAG TYPE	COMMOM PHASES	MINOR PHASES
Glassy	* Glasses of variable composition * Spinels of variable composition (Fig.'s 1&2) ● Droplets of Fe sulfide and/or Fe sulfide/oxide intergrowths, often with tiny Fe-Ni alloy grains (Fig. 3)	* Al_2SiO_5: Andalusite or silliman-ite, needs crystal structure work * Corundum: Al_2O_3, needles * Eskolaite: Cr_2O_3, exsolution lamellae in Cr-rich spinels * Karelianite: V_2O_3, crust on sulfide bleb * Hematite: Fe_2O_3, irreg. chunk
Sulfide rich . . .	* Fe-sulfide: ~FeS, and/or FeS/FeO intergrowths, often with tiny Fe-Ni alloy inclusions (Fig. 3) * Spinels of variable composition (Fig.'s 1&2) * Glass droplets of variable composition * FeO dendritic crystals and blebs	* long acicular sulfide crystals of unknown phase, need crystal structure analysis to identify) * ~1 μm blocky sulfide crystals ? * Pentlandite: $(Fe,Ni)_9S_8$ or monosulfide solid solution (?) * $(Fe,Ni,Cr)VS_2$: not a known mineral * Unknown euhedral CaFeMg-silicate phase * Hercynite: $FeAl_2O_4$, or (?) $FeAlO_3$: (not a known mineral) ▾ V_3O_4: (not a known mineral)
CaFeMg-silicate rich subgroup of sulfide rich slags:	* CaFeMg-rich glasses * Akermanite: $Ca_2MgSi_2O_7$, with Fe and Al partially substituting for Mg * Pigeonite: $(Mg,Fe,Ca)(Mg,Fe)Si_2O_6$, with minor Na substituting for Ca and minor Al substituting for Si * Fayalite: Fe_2SiO_4, with Mg,Ca and Na partially substituting for Fe and minor Al substituting for Si * Unknown euhedral CaFeMg-silicate phase * Spinels of variable composition (Fig.'s 1&2) * Droplets of Fe-sulfide and/or Fe-sulfide/oxide inter-growths, often with tiny Fe-Ni alloy grains (Fig. 3)	
V-oxide rich . . .	* CaV_2O_6: not a known mineral * NaV_6O_{15}: not a known mineral * $NaCaV_8O_{20}$: not a known mineral * $FeCaV_2O_7$ or $(Fe,Ca)VO_4$: need crystal structure analysis to determine actual phase * VO_2: Paramontroseite polymorph * Spinels of variable composition (Fig.'s 1&2) * Glass droplets of variable composition	* Hematite: Fe_2O_3, with Al & V partially substituting for Fe * Corundum: Al_2O_3, with an unknown element partially substituting for Al * Sarcolite: $(Ca,Na)_4Al_3(Al,Si)_3Si_3O_{24}$ with Mn(?) partially substituting for Ca * Heazlewoodite: Ni_3S_2 * Bunsenite: NiO * FeV_2O_6: not a known mineral * unidentifiable submicroscopic V-oxide bearing crystals

Petroleum Coke
Slag Spinels

Axes in mol %

MgV2O4

NiV2O4

Ca-Fe-V Oxide Host

MgAl2O4
Spinel

NiAl2O4

Mg(Cr,Fe)2O4

Magnesiochromite MgCr2O4
& Magnesioferrite MgFe2O4

Nichromite
(Ni,Co,Fe)(Cr,Al)2O4
& Trevorite NiFe2O4

Ni(Cr,Fe)2O4

(side view of Ni to Mg compositional prism)

NiV2O4

Ca-Fe-V Oxide Host

MgV2O4

NiAl2O4
& Ni(Cr,Fe)2O4

MgAl2O4
& Mg(Cr,Fe)2O4

Axes in mol %

(end view of Ni to Mg
compositional prism)

Axes in mol %

V

Ca-Fe-V Oxide Host

Al

Fe^{3+}
+ Cr

FIGURE 1.

FIGURE 2a.

FIGURE 2b.

(end view of Fe^{2+} to
Mg compositional prism)

V

Al   Fe^{3+}
                                       + Cr

Glass Hosted Spinels

(end view of Fe^{2+} to
Mg compositional prism)

V

Al   Fe^{3+}
                                       + Cr

FeS-FeO-F.M. Hosted Spinels

(end view of Fe^{2+} to
Mg compositional prism)

V

Al   Fe^{3+}
                                       + Cr

Ca-Fe-V Oxide Hosted Spinels

(end view of Fe^{2+} to
Mg compositional prism)

V

Al   Fe^{3+}
                                       + Cr

Ca-Fe Silicate Hosted Spinels

213

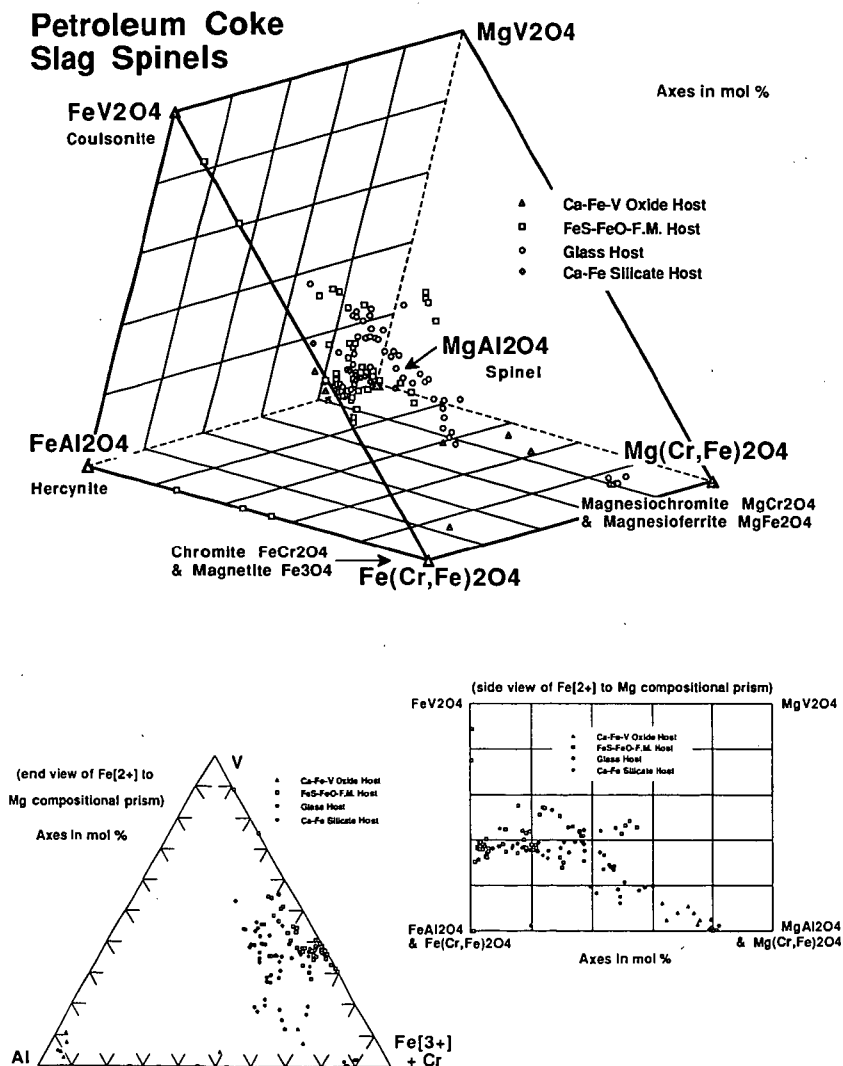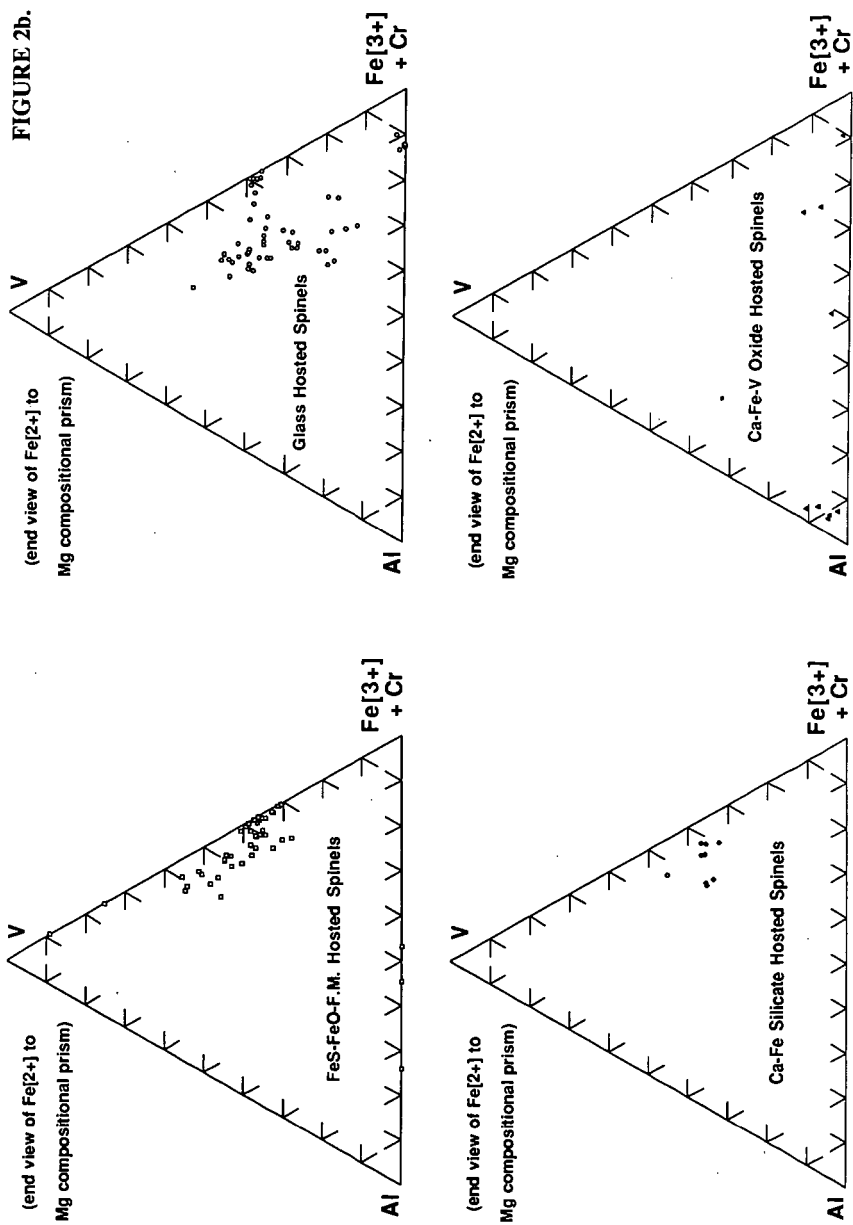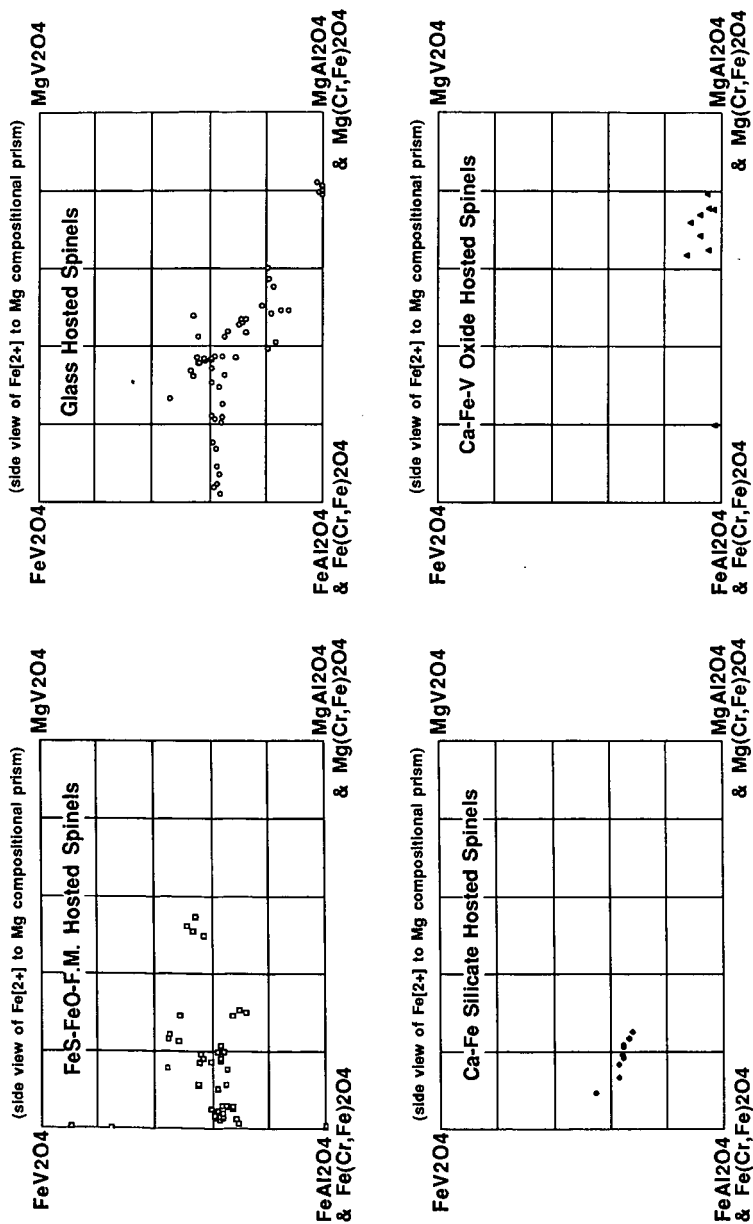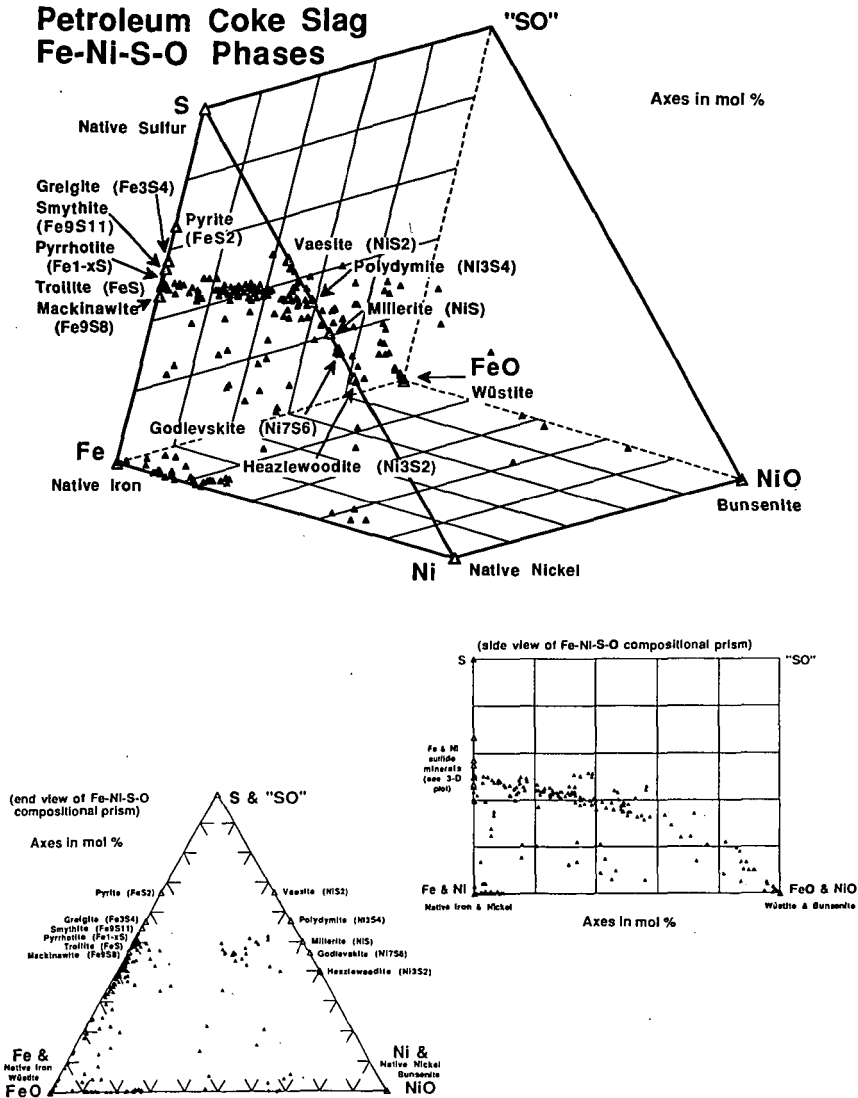FIGURE 2c.

214

Petroleum Coke Slag
Fe-Ni-S-O Phases

FIGURE 3.

AUTOMATED IMAGE ANALYSIS OF THE ASSOCIATION OF ASH-FORMING MINERAL MATTER WITH COAL PARTICLES

Warren E. Straszheim and Richard Markuszewski

Fossil Energy Program, Ames Laboratory,
Iowa State University, Ames, IA 50011.

ABSTRACT

Scanning electron microscopy (SEM), energy-dispersive x-ray spectroscopy (EDS) and automated image analysis (AIA) techniques were used for the characterization of the association of ash-forming mineral particles with coal particles. Mineral matter can be found as grains free from the coal matrix or embedded within particles of coal in various proportions and in a range of compositions of the mineral phases. Such mixtures will influence the chemistry of the ash particles generated from the coal, so that the behavior of the ash can be quite different from the behavior predicted by the bulk ash chemistry. ·SEM-based AIA conducted for several thousand composite coal and mineral particles provides data which can be used to predict the range of ash particles that will be produced from a coal. Results of analyses are reported for a number of bituminous coals.

INTRODUCTION

Over the years, changing practices in coal combustion have led to a need for more detailed characterization of the ash-forming mineral matter in coal. Traditional characterization methods have been performed on bulk samples of ash derived from burning off the coal at relatively large particle sizes (1). That ash is compacted during fusibility tests, so that there is considerable opportunity for interaction of the ash particles and so the ash may be expected to behave in accordance with its average chemistry. Such a test is suited to the ash environment in a stoker-fired boiler where the ash particles do have extensive contact with other ash particles. However, in many modern pulverized coal boilers, ash particles are more likely to result from single particles of coal and remain relatively unaffected by other ash particles. Thus, ash behavior might be expected to be more dependent on the mineral/ash chemistry of individual particles rather than on the bulk ash chemistry. This hypothesis appears to be born out by operating experience where coals of similar bulk ash chemistry can lead to significantly different ash behaviors (2).

Scanning electron microscopy (SEM) along with energy-dispersive x-ray spectroscopy (EDS) offer many insights into coal and mineral particles which should be helpful in predicting ash behavior. These techniques are able to characterize samples for size and elemental composition on a scale appropriate for determining particle ash chemistry. In conjunction with automated image analysis (AIA) techniques, the above analyses can be automated to provide statistical significance in the results.

For the past few years, methodologies have been developed and applied at the Ames Laboratory and elsewhere for the characterization of mineral grains in coal (3,4,5). In much of that work, attention was focused on the fundamentals of measuring particle size and determining a mineral particle's identity from its x-ray spectrum. Less work has been directed toward determining the association of the minerals grains with the coal. Moza et al. (3) reported rather interesting efforts to measure the average elemental content of composite coal and mineral particles. However, there were certain limitations to their approach and the work was not followed up. At the Ames Laboratory, we have continued to develop AIA methodology for the determination of the association of

216

mineral grains with coal. Work has focused on determining the weight fraction of the mineral and coal phases within the particles. The results have been used primarily in the field of coal preparation to predict the partitioning of phases during physical cleaning (6). However, the data on particle mineral content could just as well be presented in a manner suitable for predicting the nature of the resulting ash particles based on information about their mineral precursors.

METHODOLOGY

Coal samples were prepared for analysis by embedding approximately 2 g of coal in 10 g of carnauba wax according to procedures described elsewhere (7). Samples were embedded at the particle size of interest (i.e., approximately 80% passing 200 mesh for pulverized coal). The ground coal was mixed with molten carnauba wax and the mixture was poured into a cylindrical mold where it was allowed to cool and harden under pressure. The cylindrical pellet was cut vertically along its axis to expose a section through the coal and mineral particles. The exposed section was polished using standard petrographic procedures and then coated with 150 Å of carbon to provide electrical conductivity during SEM examination.

Samples were characterized with an image analysis system consisting of a JEOL JSM-840A electron microscope, a KEVEX model DELTA V energy-dispersive x-ray analyzer, and a LeMont Scientific model DB-10 automated image analyzer. Samples were imaged using the backscattered electron (BSE) signal at magnifications of 100, 200, and 500 times, and with a resolution of 512 pixels (i.e., sampling points) across the field of view. The multiple magnifications were used to provide sufficient resolution across the range of particle sizes present in the sample. Coal and mineral particles were identified, based on the brightness of their BSE signal, and were then characterized for particle area, diameter, perimeter, and other basic parameters. The electron beam was then returned to the center of each mineral particle and the x-ray analyzer was used to collect an x-ray spectrum (2 to 4 seconds acquisition time). The integrated intensities were determined for 20 common mineral-forming elements ranging from oxygen to zinc, and those intensities were compared with up to 20 sets of mineral definitions based on the relative abundance of the elements to identify the mineral phase (4,5). Minerals were identified as the first phase with elemental definitions matching the measured intensities.

The size and elemental data for each coal and mineral phase were recorded on magnetic disk for later data reduction. Significantly, the LeMont Scientific image analysis software recorded the data for associated coal and mineral particles together in such a manner that it was possible to determine the association of particles. For a composite assemblage, the measured areas of each of the phases present were used in conjunction with tables of densities of the phases to calculate the weight fraction of each phase within the particle.

The above measurements were made for thousands of composite coal-mineral particles in order to achieve a measure of statistical reliability. It then remained to tabulate the particle data in a format that was of technological interest.

For this paper, 200-mesh samples of Upper Freeport and Pittsburgh No. 8 coals were used to illustrate the capabilities of the AIA measurements. The general characteristics of these coals are summarized in Table 1. Both coals are bituminous coals with about 15% mineral matter. The amount of pyritic sulfur varied and thus the pyrite fraction of the mineral matter was considerably different between the two coals.

217

Table 1. General characteristics of the Upper Freeport and Pittsburgh No. 8
coals (results are on a dry basis unless otherwise noted).

	Upper Freeport	Pittsburgh No. 8
Moisture[a]	1.74	3.50
Total S	2.36	4.27
Pyritic S	1.98	3.15
Sulfate S	0.02	0.12
Organic S	0.36	1.00
Ash	12.4	11.4
Mineral Matter[b]	14.9	14.4

[a] As-received basis

[b] From modified Parr formula MM=1.13(Ash)+0.47(Pyr.S) (ref. 8, in which
MM = mineral matter)

RESULTS AND DISCUSSION

Typical measurements available using the current technology are shown in
Table 2 for some selected coal-mineral particles. The identity of each phase is
given along with its area, average diameter, and significant x-ray signals.
These results were used to calculate the abundance of phases within the particle
as shown in Table 3. The total area of each phase was multiplied by that
phase's density to estimate its weight contribution. These tables illustrate
that a wide range of particles are encountered in coal, including nearly pure
coal particles with very small, isolated mineral particles, coal particles with
a large amount of a single mineral phase, and coal particles with a mixture of
two and more minerals in a wide range of relative abundances.

The particles can be classified in any number of ways depending on the
characteristics of interest. Currently, particles are tabulated according to
the weight fraction of the combined minerals within them. This results in
distributions as shown in Table 4 and in Figures 1 and 2. Such distributions
indicate significant differences between these coals regarding the closeness of
association of the mineral phases with coal. Minerals are more closely
associated with the coal matrix in the Pittsburgh sample than they are in the
Upper Freeport sample. Also, relatively more of the mineral matter in the
Pittsburgh coal is pyrite which is somewhat more closely associated with the
coal than it is in the Upper Freeport coal. Relatively more of the mineral
matter in the Pittsburgh sample consists of quartz, clays, and other silicates.

These formats were developed with utility for density-based coal cleaning
in mind. The particle density can readily be calculated, given the mineral
composition of each particle. Predictions can then be made about the amount of
sample and which phases and particles are likely to report to the clean coal
stream.

However, weight fractions calculated from AIA results could also be used to
calculate the overall elemental composition for the particles. Such
compositions could then be used in conjunction with ash modeling efforts to
predict ash particle characteristics.

For the prediction of ash characteristics, the particles may be treated in
two ways. One model of ash formation assumes that each mineral grain will

Table 2. Typical SEM-AIA measurements for selected particles of Upper Freeport coal.

Phase	Area (μm^2)	Avg. Diam. (μm)	X-ray elemental intensities (as % of all x-rays)
Coal	561	26.7	none
Coal	1650	45.8	none
Pyrite	89	10.6	S=81, Fe=19
Coal	11	3.8	none
Quartz	30	6.2	O=4, Si=93, K=3
Illite	36	10.5	O=4, Al=33, Si=49, K=14
Coal	17	4.7	none
Coal	362	22	none
Misc.	10	3.7	O=5, Al=95
Quartz	62	8.9	O=3, Si=97
-----	----	----	
Total	2267	53.7	
Coal	1320	41.0	none
Kaolinite	20	5.1	O=7, Al=43, Si=50
-----	----	----	
Total	1340	41.3	
Coal	181	15.2	none
Iron Sulfate	157	14.2	O=9, Al=7, S=68, Fe=16
Quartz	24	5.6	O=5, Si=95
Coal	347	21.0	none
-----	----	----	
Total	709	30.0	
Coal	59	8.7	none
Coal	81	10.2	none
Iron Sulfate	821	32.3	O=12, S=62, Fe=26
-----	----	----	
Total	961	35.0	

Table 3. Abundance of coal and mineral phases for the particles shown above in Table 2 (as weight % of particle).

	Identified Phase and its Density (g/cm^3)						
	Coal 1.30	Pyrite 5.00	Fe Sulfate 3.00	Quartz 2.65	Kaolinite 2.65	Illite 2.75	Other 2.50
Particle 1	100.0	---	---	---	---	---	---
Particle 2	78.9	13.2	---	7.2	---	2.9	0.7
Particle 3	97.0	---	---	---	3.0	---	---
Particle 4	56.0	---	38.6	5.4	---	---	---
Particle 5	6.9	---	93.1	---	---	---	---

Table 4. Association of coal and ash-forming minerals in Upper Freeport coal as a function of particle mineral content.

Category	0	1-20	21-40	41-60	61-80	81-100	Sum
			Mineral content %				
Coal	55.05	22.42	5.42	2.53	1.37	0.33	87.10
Mineral Matter[a]	0.00	1.87	2.23	2.38	3.09	3.33	12.90
Total	55.05	24.29	7.64	4.91	4.46	3.66	100.00

[a] Where "Mineral Matter" includes:

	0	1-20	21-40	41-60	61-80	81-100	Sum
Pyrite	0.00	0.32	0.66	0.87	0.91	1.96	4.73
Fe⁻sulfate	0.00	0.04	0.06	0.06	0.04	0.15	0.35
Kaolinite	0.00	0.30	0.28	0.38	0.18	0.11	1.24
Illite	0.00	0.25	0.28	0.40	0.44	0.16	1.53
Quartz	0.00	0.20	0.30	0.13	0.68	0.46	1.77
Silicates	0.00	0.52	0.47	0.46	0.67	0.39	2.51
Other	0.00	0.25	0.17	0.07	0.18	0.10	0.76

produce one mineral particle, while another model assumes that all of the mineral grains in a single coal particle coalesce to form a single ash particle. For either model, AIA results could be used to predict the overall composition and mass/size distributions of the ash particles. The appropriate phase diagrams could then be used to help predict the character of the ash particles. For example, some particles may contain clay particles along with pyrite. The iron could serve as a flux and lead to a low melting point (i.e., sticky) ash particle, whereas clay particles associated with quartz or with no other minerals could lead to more refractory ash particles.

Or again, predictions could be made using both scenarios. First, each mineral particle could be assumed to follow a known transformation during combustion, apart from the influence or contribution of other mineral grains in the same composite. For example, quartz by itself would be relatively unaltered during combustion, while pyrite would lose its sulfur and form a particle of iron oxide, Fe_2O_3. Secondly, for each composite particle, the mineral grains could be assumed to interact. The iron from pyrite might be expected to serve as a flux for clay particles and lead to a low melting point mixture when both are present in the same composite.

However, we are not currently involved in developing models of mineral transformations during combustion. Instead, we are involved in developing the unique capabilities of SEM-based AIA to provide the necessary data for those who are interested in modeling mineral transformations to ash. We leave it to other researchers to determine the relative importance of the various modes of production of ash particles, whether they are produced one per mineral grain, are produced one per composite particle, or are produced as a result of ash particles agglomerating during combustion. We do seek to provide reliable data as input for those models.

CONCLUSIONS

AIA is able to provide detailed characterization of ash-forming mineral particles which can be used as input to models of ash formation and behavior. Significant differences have been observed in the distribution of mineral particles in different coals in the areas of mineral abundance, mineral size distributions, and the extent of association of mineral particles with coal.

Since such differences exist, it is not surprising that coals behave in markedly different ways even though they have the same nominal ash chemistry.

Further development of AIA applications for the prediction of ash behavior is necessary. Particularly, more work needs to be done on preparing the results into formats that are directly applicable to ash modeling efforts. Perhaps elements of the ash models can be incorporated into the AIA programs to directly provide the desired results. Much work also needs to be done to validate results and predictions based on AIA results. There is nearly always concern over how well two-dimensional AIA measurements can represent three-dimensional reality. And the accuracy of the ash models themselves will need to be determined. Nevertheless, the combination of detailed AIA characterization and ash modeling should provide a much improved indicator of ash behavior than older methods of ash characterization which are less than appropriate in view of current combustion technology.

REFERENCES

1. "Fusibility of Coal and Coke Ash", Standard D-1857, Annual Book of ASTM Standards, American Society of Testing and Materials, Philadephia, PA, 1989.

2. W.A. Sleiger and J.H. Singletary, "How Reliable are Correlations Between Coal Ash Chemistry and Ash Fusibilities", in Mineral Matter and Ash Deposition from Coal, R.W. Bryers and K.S. Vorres, eds., Engineering Foundation, New York, 1990, pp. 137-146.

3. A.K. Moza and L.G. Austin, "Analysis of Pulverized Coal Particles (10-100 μm) for Fe, S, Ca, Si, and Al on a Particle-by-Particle Basis", Fuel 62 1468-1473, (1983).

4. F.E. Huggins, G.P. Huffman, and R.J. Lee, "Scanning Electron Microscope-based Automated Image Analysis (SEM-AIA) and Mossbauer Spectroscopy", in Coal and Coal Products: Analytical Characterization Techniques, E.L. Fuller, Jr. ed., Am. Chem. Soc., Washington, D.C., 1982, pp. 239-258.

5. W.E. Straszheim, J.G. Yousling, and R. Markuszewski, "Analysis of Ash-Forming Mineral Matter in Raw and Supercleaned Coals by Automated Image Analysis-Scanning Electron Microscopy", in Mineral Matter and Ash in Coal, K.S. Vorres, ed., Am. Chem. Soc., Washington, D.C., 1986, pp. 449-461.

6. W.E. Straszheim and R. Markuszewski, "Evaluation of Physical Coal Beneficiation Using Computerized Microscopy", in Process Mineralogy IX, W. Petruk, D. Hausen, R. Hagni, and S. Pignolet-Brandom (eds.), TMS-AIME, Warrendale, PA, 1990, pp. 155-166.

7. W.E. Straszheim, K.A. Younkin, R.T. Greer, and R. Markuszewski, "Mounting Materials for SEM-based Automated Image Analysis of Coals", Scanning Microscopy, 2(3), 1257-1264, (1988).

8. P.H. Given and R.F. Yarzab, "Analysis of the Organic Substance of Coals: Problems Posed by the Presence of Mineral Matter", In Analytical Methods for Coal and Coal Products, Vol. II, C. Karr, Jr., ed., Academic Press, New York, 1978, pp. 3-41.
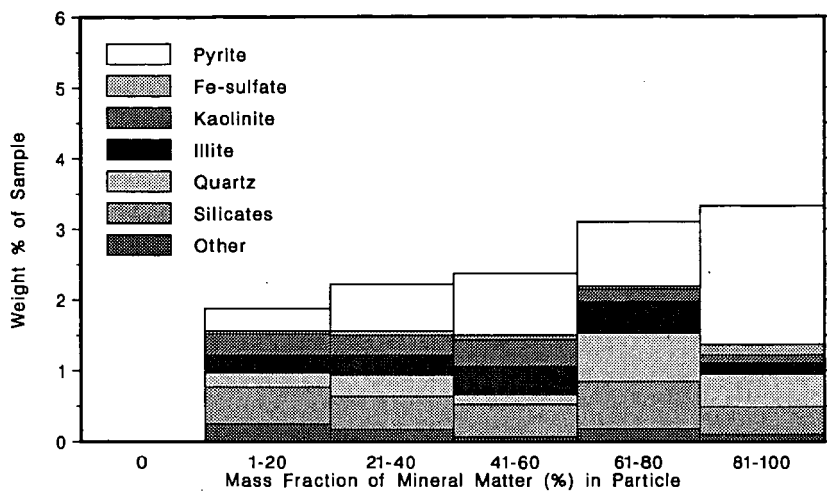
Figure 1. Distribution of ash-forming minerals in Upper Freeport coal as a function of particle mineral content.
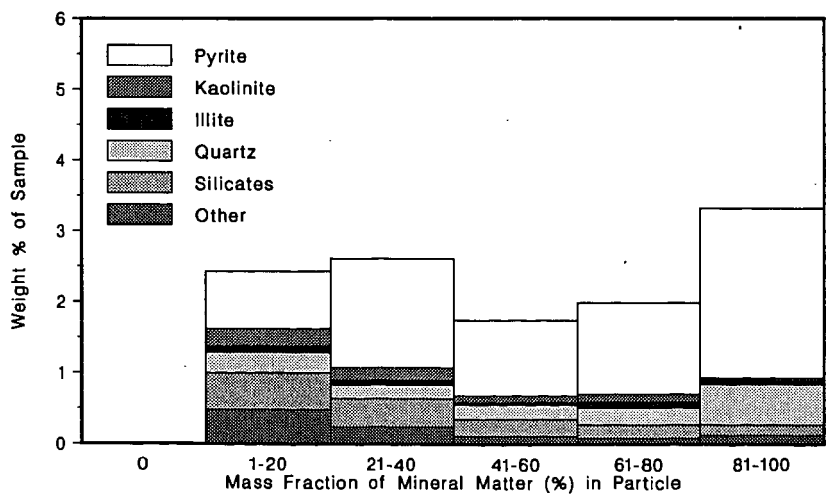

Figure 2. Distribution of ash-forming minerals in Pittsburgh No. 8 coal as a function of particle mineral content.

THERMAL PROPERTIES OF COAL ASHES

RAMONA LEDESMA AND L.L. ISAACS
The City College of CUNY, Dept. of Chemical Engineering, New
York, New York 10031

ABSTRACT

The applicability of differential thermal analysis to
determine the fusibility behavior of coal ashes was
investigated. The technique proved useful to obtain four
specific temperature points. These are: the minimum sintering
temperature, the softening point, the point of complete
fluidity and the reaction temperature which is tentatively
identified as a phase boundary crossing or eutectic
temperature.

INTRODUCTION

There is an abundance of coal in the United States, much
of which is used for power generation. It is envisioned that
in the future coal will be converted to "synfuel" as a
replacement for crude oil. Coal in itself is a complex mixture
of organic and inorganic components, together with large
quantities of physically and/or chemically bound water. The
inorganic component, which may amount to 15 to 20% by weight of
the coal, is a complex mixture of quartz, pyrite, calcite, and
silicates. Trace quantities of many metals are present. In
the combustion process the coal is converted to ash, steam and
other vapors.

Kiss and King [1] consider that the ash forming
constituents should be classified into two groups: inorganics
and minerals. The inorganic are relatively evenly distributed
through the coal, while the minerals occur as discreet
particles throughout the coal seam. The minerals are converted
to ash via a pathway that includes dehydration, dehydroxylation
and gas/solid phase reactions. The inorganics, which are the
major ash forming species, are converted to ash via a pathway
that includes coal devolatilization, burning of the solid
residue (char), reduction of metal oxides, release of fly ash,
sulfur, and other species, nucleation and growth of solid
particles, gas phase reactions and condensation, and gas/solid
phase reactions. Thus the ash material is likely to be a
heterogeneous mixture of oxides, phosphates and sulfates.

In an industrial combustion process, a portion of the ash
will be carried along with the stack gases. This "fly ash" may
differ in composition and/or structure from the remaining
"bottom ash". Ash formation is a by-product in reactions such
as coal liquification. The inorganic phase itself may

223

influence the kinetics and the products distribution of various reactions and may have a strong bearing on the service life of the process equipment.

The ash must be removed from the process and disposed of in a safe and economic manner. Intensive research efforts are underway to find uses for ashes of various kind and to overcome the contamination of the environment by leaching from landfills and through the escape of fly ash into the atmosphere.

The efficient design of coal combustors, coal processing reactors, and ash removal systems mandates that the designer has information available on the thermal characteristics of the ash. The data base needed include: Ash fusion characteristics, heat capacities, and thermal conductivities.

The standard test to determine the fusibility behavior of coal ashes is the ASTM D-1857 "Fusibility of Coal and Coke Ash" procedure. It prescribes a preparation and measurement scheme which yields four "call" points which presumably describe the fusing process. The points are empirically defined and bear tenuous relations to actual physical phenomena.

Sintering of a powder leads to the reduction of volume and surface energy. Thus the onset of sintering, i.e. the minimum sintering or agglomeration temperature, can be determined either by dilatometry or by a technique such as differential thermal analysis (DTA).

In dilatometric experiments [2] the powder to be tested is placed into a quartz tube and piston assembly, and the sample is compressed by an adjustable load. The experimental assembly is then heated at some preselected rate and the expansion or contraction of the sample is detected by a linear variable differential transducer and recorded as a function of temperature. In general, the powder dilates on heating due to thermal expansion. Eventually, a temperature is reached where the surface of the particles begin to deform due to viscous flattening and/or sintering at the intergrandular contact points resulting in contraction of the sample. The temperature at which this phenomenon occurs is the minimum sintering temperature, Ts. Ts is a characteristic for each powder and the point where particle agglomeration will first occur.

DTA indicates the onset temperature of change and the direction of change in the internal energy of a material due to heating. Reduction of surface energy is a exothermic event and will show up as such in the DTA signal. Fusion on the other hand is an endothermic event and will manifest itself as such in the DTA signal. Chemical reactions and non-ideal dissolution phenomena will show up as either increases or decreases or as slope changes in the DTA signal. In principle, besides yielding minimum sintering temperatures DTA should provide further fusibility information on ash powders. DTA experiments were performed on a set of coal ashes prepared from coals of the Argonne Premium Coal Bank and are reported here.

EXPERIMENTAL TECHNIQUE

     Ashes were prepared from eight coals. These were obtained
from the Argonne Premium Coal Sample Bank [3]. In Table I the
rank of the original coals and their mineral contents are
listed. The ashes were prepared by combustion of 100 mesh size
particles at 700°C in a muffle furnace. Part of the ashes were
used for DTA measurements and elemental analysis. The rest was
heated to 1000°C in a muffle furnace before being used for
experiments in the DTA. Elemental analysis was performed using
the inductively coupled plasma technique. Results of the
elemental analysis are given in Table II. The fusion behavior
of the ash powders was investigated with the use of DTA [4]. A
DuPont 2100 Thermal Analyzer with a high temperature (1600°C)
DTA cell was employed. The samples were heated from 300K to
1900K at the rate of 20°C/min in nitrogen flow. The instrument
was calibrated using zinc and gold as standard materials.

RESULTS AND DISCUSSION

     The results of the DTA experiments on the ashes derived
from the Pittsburgh #8 coal are shown in figure 1. The
ordinate of the graph   represents the temperature deviation
of the ash sample from a baseline which corresponds to the
temperature evolution of a sample not undergoing a physical or
chemical transformation process.
     This set of results is indicative of the results obtained
for the other ashes with some variation in details. As was
expected, several characteristic temperatures at which
significant events occur may be identified. These points of
interest, starting with the lowest temperature, are the:
.   Onset of particle agglomeration (sintering), Ts.
.   Onset of fusion (ash softening), Ti.
.   Point of discontinuous change in   , Tr.
.   Point of complete fluidity, Tf.

     In Table III we tabulate these temperature points for all
the ashes. One should note that for a given origin ash there
is only a relatively small variation in the characteristic
temperatures for the ash powders prepared at different
temperatures.

The Minimum Sintering Temperature

     We previously reported [2] minimum sintering temperatures
for a number of coal ashes spanning the same geographic
spectrum as those reported here. The method of detection
employed in the prior work was dilatometry. In general, the Ts
value detected by dilatometry was approximately 100K larger
than that detected by DTA. We attribute much of this
discrepancy to the way the DTA method was employed in these
experiments. However it is important to note that both of
these techniques yield a minimum sintering temperature

225

substantially lower than the initial deformation temperature (IDT) of the ASTM procedure. Rhinehart and Attar [5] have proposed a model for the ash fusion temperatures based on the freezing point depression equation for ideal binary solutions. They used a data base of 263 ashes to perform a seven-parameter correlation analysis. Six of the parameters are statistically determined "pseudo" heats of fusion for the assumed ash components, and the seventh is a fusion temperature for the "average composition" ash. The calculated average ash IDT is 1411K. Experimentally determined IDT's for the Argonne ashes range upwards from 1340K in a reducing atmosphere and upwards from 1445K in an oxidizing atmosphere [3]. It is clear that the IDT temperature is not a measure of the onset of agglomeration.

The Fusion Phenomenon

Melting is a first order phase transition phenomenon accompanied by a discontinuous increase in the enthalpy for pure homogeneous compounds. For dilute solutions the freezing point depression expression may be used to estimate the initial decrease in the freezing point of the solvent due to the addition of the non-volatile solute. Ashes are heterogeneous mixtures and certainly do not act as dilute solutions. The individual compounds which make up the ash mixture each have melting points which are higher than the most of the observed initial softening temperatures, T_i. In the sintering process melting of the powder surface occurs hence several oxides can dissolve in each other. These oxide solutions have substantially lower melting temperatures than the individual oxides. For example the melting point of an iron oxide-silica slag of composition $Fe_2S_iO_4$ has the melting point of 1450K. Thus the initial softening temperature Ti may be considered as the melting point of the lowest melting "component" in the system. The molten component then acts as a solvent and dissolves some of the remaining solid. The dissolution process, unlikely to be ideal (i.e. $H_{sol} = 0$), is accompanied by an enthalpy change. Completion of dissolution is marked by the fluidity temperature Tf. During the dissolution process one reaches eventually a point where the solution composition passes a phase boundary. Such a boundary crossing may be associated with a latent heat or may be athermal. It is our conjecture that the sharp change in   at the temperature which we call Tr indicates such an event. It is to be noted that in the vicinity of Tr we have the greatest variability in the nature of the DTA curves.

The Initial Softening temperature

The softening temperature as evaluated by Rhinehart and Attar is 1478K for the average ash. Values for the Argonne ashes, range upwards from 1365K depending on the particular ash and on the furnace atmosphere [3]. For the ash illustrated in Figure 1 we estimate that in an inert atmosphere the initial

deformation temperature, the spherical softening point and the hemispherical softening points are 1520K, 1550K, and 1580K respectively. From the Ti values as defined, we estimate that the initial softening point for a 850°C ash (ashing temperature for the ASTM test) is approximately 1375K.

The Discontinuous Change Temperature

Of the sixteen ashes examined, eight show only a discontinuous endothermic change in   , seven show exothermic behavior in   prior to the endothermic discontinuity and one ash shows no discontinuity (hence no Tr) of any kind. Tr ranges from 1490K to 1680K. It is likely that Tr is very sensitive to both ash composition and to ashing temperature.

The Fluidity Temperature.

The ASTM test for fusibility defines the fluidity temperature, Tf, as the point where the test sample height has decreased to approximately 10% of its original value. We consider it to be the temperature where there is a final change in   indicating the melting (or dissolution) of the last bit of solid ash. The fluidity temperature for the average ash according to the Rhinehart correlation is 1581K (1609 for low Calcium ashes). For the Pittsburgh #8 ash the measured ASTM fluidity point is 1600K in a reducing atmosphere and 1705K in an oxidizing atmosphere. The DTA Tf point is 1720K for this ash.

CONCLUSION

.   The DTA technique to determine the fusion behavior of ashes is convenient and yields a set of physically meaningful parameters.
.   An accurate model describing the fusion behavior of ashes, based on composition, ashing temperature, and physical structure might be possible once a more extensive experimental data set is collected.

ACKNOWLEDGEMENTS

227

REFERENCES

1. L.T. Kiss and N.T. King, Fuel <u>56</u>, 340 (1977)
    Fuel 58, 547 (1979).

2. R. Ledesma, P. Compo and L.L. Isaacs in <u>Fly Ash and Coal</u>
    <u>Conversion Byproducts: Characterization, Utilization and</u>
    <u>Disposal III</u>, edited by G.J. McCarty, F.P. Glasser, D.M.
    Roy and S. Diamond (Mat. Res. Soc. Proc. <u>86</u>, Pittsburgh,
    PA 1987) pp.127-136.

3. <u>Users Handbook for the Argonne Premium Coal Sample</u>
    <u>Program</u>, ANL/PCSP - 89/1. Karl S. Vorres, ed.

4. <u>Thermal Analysis</u> by W.W. Wendland (3rd Ed., J. Wiley and
    Sons) 1986.

5. R.R. Rhinehart and A.A. Attar, J. of Energy Resources
    Technology <u>109</u>, 124 (1987).

6. R. Ledesma and L.L. Isaacs, a <u>Fly Ash and Coal Conversion</u>
    <u>Byproducts: Characterization, Utilization and Disposal</u> VI,
    edited by R.L. Day and F.P. Glasser (Mat. Res. Soc. Proc.
    <u>178</u>, Pittsburgh, PA 1990) pp. 35-43.

228

TABLE I - Mineral Composition of the Coals (from [2])

COAL	RANK	MINERAL MATTER Wt % DRY COAL	MINERAL CONTENT (as % of mineral matter)			
			QUARTZ	PYRITE	CALCITE	TOTAL CLAY
UF	HVB	15.53	10	22	7	61
WY	SUBB	8.7	23	1	5	71
ILL	HVB	18.1	19	30	10	41
PITT	HVB	10.9	16	22	5	57
POC	LVB	5.5	5	2	31	62
UT	HVB	5.3	15	9	24	52
WV	HVB	21.6	12	1	1	86
ND	LGN.	8.7	7	3	20	70

TABLE II - Elemental Composition (wt. %) of the Ashes (a)

	UF	WY	ILL	PITT	POC	UT	WV	ND
Ca	1.2	11.3	1.8	1.0	3.1	2.3	0.3	9.4
Mg	0.6	2.4	0.4	0.4	0.8	0.4	0.4	3.2
Na	0.2	1.3	0.6	0.4	1.5	2.9	0.2	5.4
Al	12.3	6.7	7.0	11.4	9.5	6.1	16.1	3.0
Fe	14.7	4.4	17.2	15.2	10.8	6.6	2.1	4.9
Si	21.9	13.9	20.0	24.1	16.7	21.9	28.0	7.9
Ti	0.6	0.7	0.4	0.7	0.8	0.5	1.2	0.2
trace (b)	0.3	1.1	0.4	0.4	0.4	0.2	0.3	1.2
S (c)	1.6	8.8	2.7	0.8	5.0	3.9	0.8	12.0
K (c)	2.2	0.7	2.4	1.7	0.5	1.0	0.8	0.8

(a) Elemental analysis was done using the inductively coupled plasma technique, courtesy of DuPont's Jackson Laboratories.

(b) Trace includes; P, Sr, V, Zn, Ba, Cr, Cu, Mn, Ni and Zr

(c) K and S were calculated from SO_3 and K_2O values reported in the Argonne User's Handbook, sect 3.2, or estimated by interpolation.

TABLE III - Fusion Temperatures (K) for the Ashes

| Ashing T	Onset of Aggl. (Ts)		Onset of Fusion (Ti)		Endotherm. Drop (Tr)		Fluidity (Tf)	
	700°C	1000°C	700°C	1000°C	700°C	1000°C	700°C	1000°C
UF	900	1150	1250	1380	1675	1650	1725	1580
WY	950	950	1350	1400	1500	1490	1675	1675
ILL	950	950	1280	1440	1520	1620	1700	1540
PIT	925	950	1130	1450	1680	1660	1700	1740
POC	875	975	1350	1450	1525	1600	1650	1650
UT	975	1000	1400	1380	1620	--	1700	1650
WV	1000	1100	1400	1480	1600	--	1800	1800
ND	950	1150	1325	1375	1590	1625	1650	1640
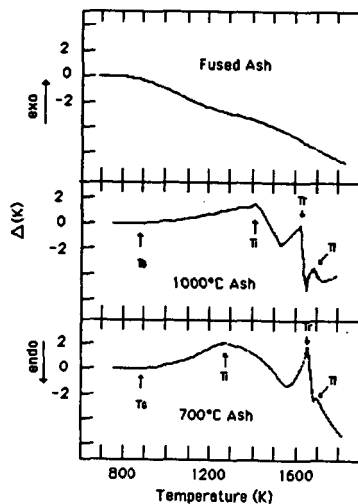
Figure 1 Differential Thermal Analysis
of Pittsburgh #8 Ash

230

THE USE OF AQUEOUS BORON TRIFLOURIDE IN DEASHING
ORGANIC RICH ROCKS AND SEDIMENTS.

T. L. Robl and B. H. Davis
Center for Applied Energy Research
University of Kentucky
3572 Iron Works Pike
Lexington, KY 40511.

Introduction.

The study of the organic matter in coal and other organic-rich rocks such as oil shale and petroleum source rocks often requires the isolation of the organic matter. The common approach is to macerate the inorganic fraction of the rock by attack with HF. This unique reagent reacts with the silicates to form SiF_4, a volatile gas, and leaves the organic matter largely unaltered.

Unfortunately HF also reacts with other inorganic components to form fluoride salts, the most pernicious being CaF_2, which is very insoluble. Thus HF is usually used in combination with HCl, which is used first as a pretreatment step to remove calcium carbonates, and then in combination with HF solutions in the final deashing step to prevent additional fluoride formation.

The use of HCl is undesirable, however, as it is a stronger acid than HF and has a stronger affect on the organic matter.[1] (See also Robinson and Saxby for further discussion on the affects of reagents on organic matter).[2,3] Also chlorination reactions are possible and undesirable. The HCl is not needed to dissolve carbonates as the HF is normally used in sufficiently high concentration to dissolve them.

The approach taken in this work is to selectively dissolve neo-formed fluorides in a two step demineralizing process, by reaction with BF_3, which is a highly water soluble gas. The BF_3 is generated by the reaction of H_3BO_3 with HF,

1. $H_3BO_3 + 3HF \rightleftharpoons BF_3 + 3H_2O$

and it then reacts with neo-formed fluoride salts, such as fluorite, to form water soluble fluoroborates.

Methods.

<u>Samples and Sample Preparation.</u> Four oil shales including the Stuart from Australia, the Green River from the U.S. (Rock Springs, Wyoming), the Irati from Brazil (Sao Mateus do Sul) and a sample of the Israeli Rotem (or E'fe) oil shale were used as test materials. The Stuart and Irati are silicates and the Israeli and Green River are carbonate shales. Two coal

samples, obtained from the Argonne National Laboratory (ANL) premium sample bank, were used in the experiments; these are the North Dakota lignite (Beulah-Zap Seam) and the Wyoming subbituminous coal (Wyodak-Anderson Seam).[4]

The oil shale was crushed to approximately -1/4" in a jaw crusher. The -100 mesh material was sieved out and the remainder of the sample passed through a Rieche mill equipped with a 100 mesh screen. The samples were then re-homogenized. The samples of lignite and subbituminous coal from ANL were used as received (-100 mesh).

HF-HCl Demineralization Procedure. For comparison purpose a fraction of the test samples were processed using a typical HCl-HF procedure.[1] Approximately 20 g of sample was stirred for 24 hours at room temperature in a sealed 1 liter heavy duty centrifuge bottle filled with 6 N HCl. The sample was then centrifuged and the residual acid decanted off through 0.45 micron filters. Material trapped on the filters was washed back into the sample containers. The sample was washed by completely resuspending it in distilled-deionized water and centrifuging. Approximately 900 ml of a 1:1 (v/v) solution of 6 N HCL and 48% HF mixture was then added to the sample, which was capped and left at room temperature overnight on a magnetic stirrer. The sample was then centrifuged and washed 5 to 6 times with distilled-deionized water, decanting each time through a 0.45 micron filter and rinsing the filtrate back to the sample. The sample was dried in a vacuum oven at 60°C overnight and disaggregated by crushing with a mortar and pestle.

Boron Trifluoride Procedure. Twenty g of sample was placed in heavy duty 1 liter centrifuge bottles and 800 ml of 1:1 v/v 48% reagent grade HF added. For samples which contained carbonates, the acid was initially added in 10 ml increments to prevent spillage from excessive foaming due to the generation of CO_2. The foaming generally ceased after approximately 40 to 50 ml of HF was added. The sample was sealed, left at room temperature and stirred overnight on magnetic stir plate. The following morning the sample was chilled in an ice bath and 250 g of boric acid was added in two 125 g increments with time left between additions for the sample to recool. The reaction of H_3BO_3 with HF is exothermic and the sample was pre-cooled to 0°C to minimize the loss of BF_3. The sample was again tightly capped and left at room temperature to stir overnight. The following day the sample was centrifuged, the supernate poured through a 0.45 micron filter and washed back to the sample. The sample was each washed 5 to 6 time by completely resuspending it in distilled-deionized water and centrifuging. It was then dried in a vacuum oven at °60 overnight.

Discussion.

The demineralized samples are composed of concentrated organic matter and residual ash which, for the most part, consist of sulfides (pyrite and marcasite). Based upon previous experience rutile and zircon are also expected to be present.[5] The total ash in the test samples varied from ~0.1% in the Wyoming subbituminous and North Dakota lignite samples to ~29% in the Irati oil shale samples. A comparison of the residual ash for sample processed by the two techniques indicate no substantive differences, with the HF-BF$_3$ technique producing slightly lower ash (Table 1).

Based upon the comparison of FTIR spectra, the organic matter in the samples processed with the HF-BF$_3$ technique does not appear to be altered more than that processed by the HF-HCl technique. Although additional analysis is needed, the currently level of data suggests that the HF-BF$_3$ procedure actual results in less organic mater alteration than the

HF-HCL procedure.

The mechanism of the BF_3-fluoride salt reaction is of interest. A search of the literature and consideration of the stoichiometry involve indicated that two reactions are possible,[6,7]

2. $BF_3 + CaF_2 \rightleftharpoons CaF(BF_4)$

or

3. $2BF_3 + CaF_2 \rightleftharpoons Ca(BF_4)_2$
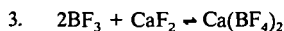
Model compound studies employing optical grade crystalline CaF_2 and $BF_3.2H_2O$ were used to explore the possible reactions. The dissolution of CaF_2 was found to depend directly upon the BF_3 concentration (Figure 1) with an equilibrium constant of 0.12. Thus, reaction 2, the formation of calcium fluoride tetraflouroborate, is indicated. During the dissolution experiments, a tan color precipitate was found to begin forming at the point where the calculated concentration of $CaF(BF_4)$ is $\sim$ 36 g/l, which we believe to be the approximate solubility of this salt.

In summary, the $HF-BF_3$ technique has certain advantageous over the more traditional approach employing HCl. Because all of the HF is converted to fluoroborates the need to handle large quantities of contaminated HF is eliminated. This approach also results in samples with as low or lower residual ash and does not alter the organic matter any more, and probably less than, more traditional techniques employing HCl.

References.

1. Durand, B. and G. Nicaise, Ch. 2, **In**, *Kerogen, Insoluble Organic Matter from Sedimentary Rocks*, B. Durand (Ed.), Editions Technip, Paris, p. 36, 1980.

2. Robinson, W.E., Ch. 6, **In**, *Organic Geochemistry*, G. Eglington and M.T.J. Murphy (Eds.), Springer Verlag, New York, 1976.

3. Saxby, J.D., **In** *Oil Shale*, Yen, T.F. and G.V. Chilingarian (Eds), Elsevier, p. 104, 1976.

4. Vorres, K.S., 1991, *Energy and Fuels*, **4**, p. 420-426.

5. Robl, T.L., D.N. Taulbee, L.S. Barron and W.C. Jones, 1987, *Energy and Fuels*, **1**, p. 507-513.

6. Paevlenko, S., *Z. anorg. allg. Chemie.*, **301**, p. 337, 1959.

7. Paevlenko, S., *Z. anorg. allg. Chemie*, **315**, p. 136, 1962.

Table 1. Comparison of Residual Ash from Demineralization of Coals and Oil Shales with HF-HCl and HF-BF$_3$ Procedures.

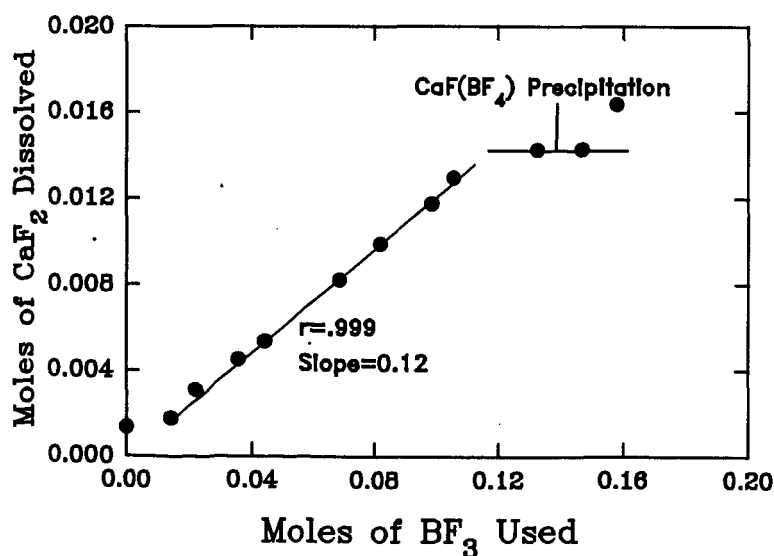| Demineralizing Procedure	HF-HCL	HF-BF$_3$
Oil Shales	%Ash	%Ash
Irati Oil Shale-Upper Bench	29.3	26.3
Israeli Oil Shale-E'fe	7.1	6.7
Green River Shale-Tipton Member	9.6	8.8
Stuart-Kerosene Creek Member	9.7	7.2
Coals		
Wyoming Subbituminous-Wyodak	<0.1	<0.1
North Dakota Lignite-Beulah Zap	<0.1	<0.1

Figure 1. Plot of CaF$_2$ dissolved versus BF$_3$ added in modal compound study.

ESTIMATION OF ASH FUSION TEMPERATURES FROM ELEMENTAL COMPOSITION:
A STRATEGY FOR REGRESSOR SELECTION

William G. Lloyd, John T. Riley, Mark A. Risen, Scott R. Gilleland,
and Rick L. Tibbitts
Department of Chemistry and Center for Coal Science
Western Kentucky University, Bowling Green, KY 42101

INTRODUCTION

Two developments within the past decade have had a major impact upon our ability
to infer useful information about ash fusion temperatures from the composition of
the ash. The emergence of fast and accurate multielement analyzers means that the
chemical composition of an ash can be determined quickly and reliably. At the same
time, the proliferation of personal computers, and of statistical software written
for them, makes it possible to rapidly estimate an ash fusion temperature, saving
the two or three days' time which would be required to determine fusion
temperatures in accordance with standard procedures.[1,2]

In order for such an estimate to be useful, a valid and reliable algorithm is
needed. Multiple linear regression (MLR) analysis has been used by a number of
workers to obtain estimates generally found to be superior to the single-term
factors used in the earlier literature.[3-10] The present work re-examines the use
of MLR analysis with particular reference to techniques for avoiding the problem
of multicollinearity.

EXPERIMENTAL

Seven source coals, of rank from lignite A to medium volatile bituminous, were
selected for study. Coal sources, proximate and ultimate analyses, and ash
compositions have been reported.[9,10] Table 1 shows the ranges of the analyses.
After reduction to -60 mesh (-0.25 mm) three blends were prepared, in the
proportions 3:1, 1:1 and 1:3, for each of the 21 binary combinations of source
coals. Ash samples from the source coals and the 63 blended coals were then
prepared in accordance with ASTM Method D 1857.[2]

Ash samples were fused with lithium tetraborate for elemental analysis by X-ray
fluorescence spectrometry, using an ORTEC Model 6141 spectrometer. Calibration and
analysis conditions have been reported elsewhere.[9,10] Cross-analyses were made by
inductively coupled plasma spectrometry, using a LECO Plasmarray ICP 500
spectrometer. It is necessary to analyze the ashes of each blend, since
composition cannot be estimated by interpolation.[10,11]

Ash fusion temperatures (reducing atmosphere) were measured in duplicate or
triplicate on ash splits using a LECO Model AF-600 ash fusibility system.
Precision for the four ash fusion temperatures is given in Table 2. Except for
fluid temperature, the average error estimate is less than 18°F (10 K).
Statistical analyses were conducted using the Statistical Analysis System.[12]

RESULTS

Ash properties cannot be adequately described by assuming a mixture of ten discrete
oxides. These components obviously interact with one another, in acid-base and in
other metathetic reactions. To take account of these, a set of crossterms can be
generated, for example, $[Na_2O]*[SO_3]$ from $[Na_2O]$ and $[SO_3]$.[4,5,7-10] For brevity these

235

oxides and their crossterms will be represented by the parent element symbols, e.g., Na and Na*S.

Limitations Imposed upon Regressor Selection.   In developing an algorithm to estimate an ash fusion temperature, the main task is that of selecting regressor terms from among the ten direct analyses and the 45 crossterms. The wealth of candidate regressors requires the use of some selection rules. There are, for example, 29 million six-term combinations of these regressors. We have chosen to focus upon the extent of collinearity among the selected regressors. When a substantial linear dependence exists between two variables, they are said to be collinear.[13]   While high collinearity between a predictive variable and the dependent variable indicates a good predictive relationship, high correlations among predictive variables are not desirable. MLR analysis is based upon the assumption of orthogonality: the distribution of values of each predictor is assumed to be independent of the distribution of values of any other predictor. That ideal condition is seldom found in real data, certainly not in coal ash compositional data. Fortunately, multiple regression can tolerate an appreciable amount of collinearity among regressors.   Nevertheless, a major hazard in MLR analysis is that in the presence of excessively high collinearities among regressors (multicollinearity) it is easy to get predictive equations which are good-looking in terms of R^2 and root mean square error of estimate (RMSE), but which are in fact useless.

Multicollinearity in a candidate regression analysis is typically detected by instabilities of regression coefficients, such as[14]

(1) large changes in values when a variable is added to or deleted from the model;
(2) large changes in values when datasets are added or dropped from the model;
(3) large standard errors associated with the coefficients of important terms.

All of these regressions are of the form:

$$AFT_{estimated} = b_0 + b_1X_1 + b_2X_2 + b_3X_3 + \ldots \qquad (1)$$

The term common to all regressions on a given AFT is the intercept term b_0. A convenient flag for multicollinearity in any particular candidate regression is the standard error of this intercept term (SEI). Since the RMSE's of the better-looking regressions are found to be about 45°F (25 K), we have adopted as a screening criterion that an acceptable regression must have an SEI value of less than 90°F (50 K).

For the following analysis Pearson's correlation coefficient R is used to express collinearity between pairs of predictor variables, while R^2 when used is the square of the multiple correlation coefficient for a given regression.

If we set the critical value of R (R_c) at 0.99, only 5 of the 55 terms (10 direct analyses and 55 crossterms) are found to have collinearities with other regressor terms for which $R > R_c$. The remaining 50 variables are free of 'significant' correlations [significant in terms of this selected value of R_c] with other predictive variables. At $R_c = 0.99$ the five collinear terms occur in a single cluster [Mg, Mg*Na, Mg*S, Mg*Si, Mg*Ti]. On the other hand, at $R_c = 0.85$, only 7 of the 55 terms are free of significant correlations with others, the other 48 occurring in three correlation clusters.

Our first approach has been to set R_c at each of several values, then for each value of R_c to generate the best available regressions which avoid combinations of regressors for which $R_{x,y} > R_c$.

When R_c is set at 0.99 there are few restrictions on regressors. For ash softening temperature we find a good four-term regression, for which R^2 = .859 and RMSE is an acceptable 58.2°F (32.3 K). When the best (by R^2) five-term regressions were examined, the first three regressions were unacceptable, all having SEI's > 200°F. For the first acceptable five-term regression R^2 = 0.885 and RMSE = 52.9°F (29.4 K). Among the next fifty regressions [the best ten (by R^2) regressions containing 6 to 10 terms] none were acceptable; all were rejected by the SEI criterion.

When R_c is set at 0.85 there are considerably more restrictions on the combinations of regressors which can be used in any particular regression. The best (by R^2) three-, four- and five-term regressions are all acceptable by the SEI criterion, but are not as powerful as those found above. For example, for the best five-term regression R^2 = 0.855 and RMSE = 59.3°F (32.9 K). There is an important difference, however, in this second family of regressions: the SEI's for all regressions are well below 90°F, and it is in fact possible to obtain good regressions with ten or more terms present. Table 3 summarizes the fits of the best regressions for these two values of R_c.

It is evident that there are major changes in the extent and complexity of regressor-regressor correlations in this range of R_c. Figures 1 and 2 illustrate the correlations among 19 regressor terms for two intermediate R_c values, 0.98 and 0.90. (Lines connecting terms indicate $R_{xy} > R_c$.) The clustering of the 55 candidate regressor terms as a function of R_c is shown in Table 4.

A Strategy for Selecting Regressors. Based upon preliminary tests, R_c was set at 0.920, and the 19 terms found to be free of correlations were taken as an initial set.

1. The best regressors were selected, by R^2 ranking, from each of the clusters of terms. The largest of these consists of ten terms (Figure 3). To illustrate this selection process with this cluster, the Ca*Ti term is found to make the greatest incremental contribution to the initial set. When this term is selected, the collinearities shown in Figure 3 require that four other terms (Ca, Ca*Na Ca*Si and K) be excluded. With these exclusions, two other terms in this cluster -- Al*Ca and Ca*S -- are isolated from collinearities and are therefore included. Upon analysis of the three remaining terms, Al*K is found to make the greatest incremental contribution to R^2 and is included; and its inclusion requires the rejection of K*Si and K*Ti. A similar R^2 testing procedure was used to select the most useful terms from each of the other clusters.

2. The best 36 regressions (with four, five and six terms) from this enlarged base were then examined, and several regressors -- which appeared in none of the best regressions -- were dropped. Three of the 36 test regressions exhibited multicollinearity. One term, [Si], appeared in all three multicollinear regressions and in none of the 33 good regressions; this term was also dropped.

3. Starting with 22 terms from the above process, steps 1 and 2 were repeated, to ensure that the most useful terms from each cluster were included. After this second iteration, a group of 23 terms remained.

4. To these final terms were added seven additional terms, selected from the pool of remaining terms on the basis of the greatest incremental improvement in overall R^2. For example, if the 24th term is Na*P, overall R^2 is incremented by 0.0063, more than by any other added term; therefore Na*P is added to the set.

237

Step 4 clearly introduces collinearities. Na*P, for example, is collinear [$R_{x,y}$ > R_c] with P*S. Among other added terms Fe*Ti is collinear with Al*Fe, and Fe and Fe*Si are collinear with both Fe*Ti and Al*Fe. The argument for inclusion of the several terms in step 4 is pragmatic: the regressions with these terms are better estimators than those without these terms, and this step still allows overall collinearity to remain at an acceptable level by the SEI criterion.

Best Predictive Regressions. The best regressions obtained under reducing atmosphere for the set of 70 ashes, following the above strategy, are given in Tables 5-8. Calculations have been carried through ten regressor terms. It is possible to generate predictive equations with even more regressors. However, the incremental improvement falls to small values as the number of terms increases. Furthermore, the probability of significance of each regressor term, which typically is > 99.9% for good regressions with as many as nine terms, falls for at least one regressor below 99% with the inclusion of the tenth term. Thus this appears to be a natural break point for these data.

Figures 4-7 show plots of estimated vs. observed fusion temperatures, using the ten-term equations of Tables 5-8. In the tables the average error is estimated using the approximation of average error for large sets:

$$E(avg) = [RMSE]*[2/pi]^{0.5} \tag{2}$$

The average observed errors of estimate are given in Figures 4-7. These are similar to but slightly lower than the estimated values.

These calculations use data from all 70 ashes. If the three most remote outliers are dropped from each calculation, the average error is decreased by an average of 3.0°F (1.7 K).

Further Testing for Multicollinearity. The most common indicators of regression fit are R^2 and the standard error of fit (RMSE). Table 9 summarizes key characteristics of four regressions on softening temperature, all with good values of R^2 and rmse. On the basis of these indicators alone, the choice would fall between the 30-term and the 55-term regressions. This choice would be unfortunate.

By the SEI criterion [acceptable regressions must have SEI's below 90°F (50 K)] only the first of these four regressions is acceptable, the other three showing SEI's of 800°F and above, indicating excessively high collinearity.

An additional test for multicollinearity is examination of the precision of the regression coefficients. Virtually all regression programs provide an estimate of the standard error associated with each coefficient. We calculate precision as a relative percentage:

$$P (\%) = 100 * [S.E. \text{ of coefficient}]/[\text{value of coefficient}] \tag{3}$$

Coefficients in multiple linear regressions are seldom obtained in high precision, since a moderate displacement in the value of any one coefficient can be balanced by slight shifts in the values of others. For good regressions, precision as defined in Eqn. 3 is typically in the range 5-30%. Table 9 shows the average precision calculated for the ten coefficients of the first regression, and for the first ten coefficients of each of the other regressions. The average error increases tenfold in going to the 20-term regression, and over a hundredfold in going to the 55-term regression.

Another test of the goodness of a regression is made by adding or deleting a dummy variable (a regressor which itself has no predictive power). Instability of a coefficient can then be calculated as:

$$I = [C_{MODIFIED} / C_{ORIGINAL} - 1] * 100 \% \qquad\qquad (4)$$

where $C_{ORIGINAL}$ and $C_{MODIFIED}$ are the regressor coefficients before and after addition/deletion of the dummy variable.

A two-digit random number term was added to each of these regressions, taking the first 70 random numbers listed in a standard statistical reference.[15] For a good regression this dummy variable should have very little effect upon the coefficients of the 'real' regressors. For the 10-term regression in Table 9 the average instability is 0.01%. However, the average instabilities for the first ten terms of the other three regressions are from two to four orders of magnitude larger.

Perhaps the most practical test of the stability of regression coefficients is that of adding or deleting cases from the dataset. If a regression is to have any useful predictive power, it must be reasonably resistant to fluctuation of coefficient values when cases are added or removed. Roughly, variations may be expected to be of the order of magnitude of the precisions of estimate of the coefficients, that is, typically 5-30% for good regressions.

Stability of coefficients to removal of cases was tested by deleting every fifth case in the 70-case dataset, producing a reduced dataset of 56 cases. (This deletion pattern was selected to avoid introduction of systematic bias.) Coefficient instabilities were calculated by Eqn. (4). For the 10-term regression of Table 9 the average instability is 14.1%, consistent with the average coefficient precision of 15.8%. For each of the other regressions in Table 9 the average average instabilities are well over 100%.

These three tests lend support to the use of a critical value of SEI as a convenient indicator of excessive collinearity. The most practical and persuasive showing of the utility of a good regression, however, is to demonstrate its ability to predict from a subset of cases the AFT's of "new" cases. We have taken the coefficients obtained with good ten-term regressions using the reduced set of 56 cases, and have applied them to the 14 excluded cases, treating these as "new" cases. Figure 8 shows the estimated and actual values of softening temperatures for these "new" cases. The average error of estimate is 36.8°F (20.4 K). A similar estimation of hemispherical temperatures yields an average error of estimate of 34.1°F (18.9 K).

DISCUSSION

Gray[7] has recently reviewed various British, American, Australian and international standards for ash fusion temperature determinations. Repeatability (within a laboratory) is 30-40 K for initial deformation temperature, 30 K for hemispherical temperature and 30-50 K for fluid temperature. Tolerated reproducibility (between laboratories) is generally in the range 50-80 K. The repeatability of instrumental ash fusion temperature in this work (Table 2) is considerably tighter than these figures. The average observed error of estimate for the four ash fusion temperatures (Figures 4-7) is 15-18 K. This error includes contributions from coal and ash inhomogeneities, splitting, chemical analysis and AFT determinations, as well as inadequacies of the fitting equations. This approach therefore appears to provide estimates of satisfactory precision.

In the better regressions for estimating softening and hemispherical temperatures certain terms are encountered repeatedly. In softening temperature regressions Al*Ca, Ca*Fe, Na*P and P often occur, always with positive coefficients; Ca*Si, P*S and P*Si also occur frequently, and always with negative coefficients. In hemispherical temperature regressions Al*Ca, Ca*Fe, and Na*P often occur, again always with positive coefficients; Ca*Si, Fe*S and P*S often occur, and always with negative coefficients. Across the ten best ten-term regressions for each AFT the

239

coefficients in the different regressions are fairly constant, exhibiting standard deviations of 10-20% relative. For example, in ten regressions on hemispherical temperature the coefficients of the common terms and their standard deviations are: Ca*Fe 41,910 +/- 4810, Ca*Si -11,740 +/- 940, Fe*S -47,610 +/- 8300, P*S -411,100 +/- 31,500.

Simple sensitivity analysis calculations have been made to determine, for various regression models, the effect of an analytical error of 1% relative upon the estimated AFT. For the best 10-term regression on softening temperature the average sensitivity for the ten ashes analyzed is 4.0°F per % relative error. The most sensitive analyte is SiO_2, for which a 1% relative analytical error produces an error of estimation of 18°F (10 K). This may be unacceptable for laboratories using atomic absorption analysis, for which repeatability for SiO_2 is 2% absolute or about 5% relative.[16] Using the second best regression (with a loss in RMSE of only 0.1°F) the average sensitivity is 2.9°F per % relative error, and that for SiO_2 is reduced from 18° to 9.8°F. The best ten-term regression on hemispherical temperature shows an average sensitivity of 2.6°F per % relative error, and a sensitivity of 9.2°F per % relative error in SiO_2 determination. The eighth best regression (which gives away 0.4°F in RMSE) shows an average sensitivity of 2.1°F/% and for SiO_2 a sensitivity of 5.2°F/%. As a practical matter it is obviously sensible to determine not only the best valid regression but also a group of regressions, perhaps the ten best valid regressions. The most useful of these can then be selected on the basis of estimated analytical errors and sensitivity analysis for each candidate regression.

ACKNOWLEDGMENT

REFERENCES

1. Method of Preparing Coal Samples for Analysis, ASTM Method D 2013, Annual Book of ASTM Standards, Vol. 5.05, American Society for Testing and Materials, Philadelphia, PA (published annually).

2. Test Method for Fusibility of Coal and Coke Ash, ASTM Method D 1857 [ISO 540], in reference 1.

3. Rees, O. W., Composition of the Ash of Illinois Coals, Circular 356, Illinois State Geol. Survey, Urbana, IL, 1964.

4. Sondreal, E. A.; Ellman, R. C., Fusibility of Ash from Lignite and its Correlation with Ash Composition, USBM Rept. GFERC/RI-75-1, Pittsburgh, PA, 1975.

5. Winegartner, E. C.; Rhodes, B. T., J. Eng. Power 1975, 97, 395.

6. Vorres, K. W., J. Eng. Power 1979, 101, 497.

7. Gray, V. R., Fuel 1987, 66, 1230.

8. Slegeir, W. A.; Singletary, J. H.; Kohut, J. F., J. Coal Quality 1988, 7, 48.

9. Riley, J. T.; Lloyd, W. G.; Risen, M. A.; Gilleland, S. R.; Tibbitts, R. L., Proc. Intl. Coal Test. Conf. 1989, 7, 58.

10. Lloyd, W. G.; Riley, J. T.; Risen, M. A.; Gilleland, S. R.; Tibbitts, R. L., Energy & Fuels 1990, 4, 360.

11. Riley, J. T.; Gilleland, S. R.; Forsythe, R. F.; Graham, H. D., Jr.; Hayes, F. J., Proc. Intl. Coal Test. Conf. 1989, 7, 32.

12. The Statistical Analysis System, SAS Institute, Inc., Cary, NC 27512.

13. Mason, R. L.; Gunst, R. F.; Hess, J. L., Statistical Design and Analysis of Experiments, Wiley, New York, 1989, p. 490.

14. Chatterjee, S.; Price, B., Regression Analysis by Example, Wiley, New York, 1977, pp 155ff.

15. Arkin, H.; Colton, R. R., Tables for Statisticians, Barnes & Noble, Inc., New York, 2nd ed., 1963, p. 158.

16. Standard Test Method for Major and Minor Elements in Coal and Coke Ash by Atomic Absorption, ASTM Method D 3682, in reference 1.

Table 1

Ranges of Properties of Coals and Ashes[a]

Coals	Low	Mean	High
rank	ligA	---	mvb
moisture	1.1%	10.9%	18.4%
% ash[b]	5.8%	11.4%	18.9%
% volatile matter[b]	25.3%	38.2%	44.1%
% carbon[b]	55.3%	67.5%	84.4%
% hydrogen[b]	3.33%	4.19%	5.06%
% nitrogen[b]	0.38%	1.04%	1.57%
% sulfur[b]	0.34%	1.08%	3.78%
Btu/lb[b]	8,770	11,500	14,700
MJ/kg[b]	20.4	26.7	34.1
Hardgrove Index	34	47	90
Free Swelling Index	0	2	9
Ash Composition			
SiO_2	33.1%	40.1%	50.4%
Al_2O_3	14.7%	22.2%	24.7%
CaO	0.55%	10.6%	26.9%
Fe_2O_3	3.49%	8.8%	24.1%
SO_3	0.72%	7.8%	10.5%
MgO	1.06%	2.28%	4.59%
K_2O	0.16%	1.37%	2.63%
P_2O_5	0.01%	0.77%	2.36%
TiO_2	0.82%	1.11%	1.66%
Na_2O	0.51%	0.91%	1.20%

[a] Coal data are from the seven source coals; ash data are from the suite of 70 ashes. [b] Calculated on a dry, ash-included basis.

Table 2

Precision of Ash Fusion Temperature Determinations[a]

Fusion Temperature, °F	DF	Std dev, °F	Avg Error, °F[b]
Initial Deformation	94	20.2	16.1
	(89)	(16.1)	(12.9)
Softening	95	13.4	10.7
	(91)	(11.1)	(8.9)
Hemispherical	94	21.8	17.4
	(89)	(19.1)	(15.3)
Fluid	93	42.0	33.5
	(89)	(35.5)	(28.3)

[a] First figures are obtained with all 70 ashes. Figures in parentheses are obtained after rejection of three outlier ashes.

[b] Estimated by Eqn. (2).

Table 3

Best Regression Fits at Two Values of R(critical)[a]

terms	R(critical) = 0.99		R(critical) = 0.85	
	R^2	RMSE, °F	R^2	RMSE, °F
3	.825	64.2°	.766	74.2°
4	.859	58.2	.804	68.5
5	.885	52.9[b]	.855	59.3
6	---	[c]	.879	54.5
7	---	[c]	.895	51.2
8	---	[c]	.908	48.5
9	---	[c]	.914	47.2
10	---	[c]	.921	45.5

----

[a] Regressions meeting the criterion that SEI < 90°F [< 50 K].

[b] Fourth best regression ranked by R^2; SEI's of first three regressions > 200°F.

[c] None of the first ten regressions ranked by R^2 have SEI's below 90°F.

Table 4

Correlation Clusters of Regressors at Various Levels of $R_{critical}$

$R_{critical}$	terms in clusters	total terms in clusters	total free terms
0.99	5	5	50
0.98	6, 4, 3, 2, 2, 2	19	36
0.95	7, 6, 5, 4, 4, 3, 2	31	24
0.92	10, 7, 7, 5, 5	36	19
0.90	19, 8, 7, 5	39	16
0.88	27, 7, 5	41	14
0.85	40, 5, 3	48	7

Table 5

Best Regressions on Initial Deformation Temperature

Intcpt.°F	Terms and Coefficients					SEI.°F	R²	RMSE.°F	average error.°F
1,863°F	S*Si -8.01E3	K*P 1.26E6	Ca*Fe 1.61E4	Al*Na 1.40E5		36.4	.803	72.1	57.5
1,822	Na*Si 5.60E4	Fe*S -5.08E4	Ca*Ti -3.49E5	Ca*Fe 7.85E4	Al*Na 1.43E5	34.3	.844	64.8	51.7
2,093	P 1.66E4	S*Si -1.82E4	Ca*Ti -2.50E5	Ca*Fe 6.26E4	Fe*Na -3.99E5	37.1	.877	58.0	46.3
	Al*Na 2.96E5								
2,138	P 1.37E4	Mg*P 1.09E5	S*Si -1.94E4	Ca*Ti -2.87E5	Ca*Fe 6.63E4	41.1	.886	56.1	44.8
	Fe*Na -4.54E5	Al*Na 3.20E5							
2,080	P 1.46E5	S*Si -1.81E4	P*Si -2.49E5	P*S -3.50E5	Ca*Ti -3.23E5	50.4	.9058	51.5	41.1
	Ca*Fe 6.28E4	Fe*Na -4.43E5	Al*Na 3.50E5						
1,654	P 1.95E5	P*Si -3.08E5	K*S -1.55E5	P*S -6.17E5	Fe*K 1.21E5	68.8	.9147	49.5	39.5
	Ca*Ti -3.90E5	Ca*Fe 7.68E4	Fe*Na -7.73E5	Al*Na 3.71E5					
1,609	P 1.94E5	P*Si -3.21E5	K*S -1.63E5	P*S -5.82E5	K*Ti 7.69E5	69.8	.9212	47.9	38.2
	Fe*K 9.03E4	Ca*Ti -3.54E5	Ca*Fe 7.40E4	Fe*Na -7.30E5	Al*Na 3.50E5				

Table 6

Best Regressions on Softening Temperature

Intcpt.°F	Terms and Coefficients					SEI.°F	R²	RMSE.°F	average error.°F
2,004°F	P*S -3.76E5	K*P 6.92E5	Na*P 3.15E6	Al*Na 7.30E4		27.5	.852	59.5	47.5
1,896	Ca*Si -5.34E3	P*S -5.52E5	Al*K 4.09E4	Al*Ca 1.48E4	Na*P 5.64E6	54.4	.882	53.5	42.7
2,344	Ca*Si -9.04E3	Fe*Si -5.86E3	K*S -5.50E5	K*Na 7.07E6	Ca*Fe 5.80E4	55.8	.9047	48.5	38.7
	Fe*Na -3.62E5								
1,827	P 1.23E5	Ca*Si -9.31E5	P*Si -2.20E5	P*S -8.26E5	Al*K 5.21E4	47.9	.9240	43.6	34.8
	Al*Ca 2.23E4	Na*P 4.64E6							
2,212	Ca*Si -1.09E4	Fe*Si -2.73E4	P*S -4.27E5	Fe*S -4.33E4	K*Na 1.69E6	65.3	.9286	42.7	34.0
	Ca*Fe 5.15E4	Al*Ca 8.48E3	Na*P 4.20E6						
1,806	Ti 1.33E5	Fe*Mg -1.75E4	Si*Ti -2.89E5	K*S -3.03E5	P*S -5.48E5	53.5	.9356	40.9	32.6
	K*Na 2.62E6	Fe*K -7.48E4	Al*K 1.10E5	Na*P 4.64E6					
2,248	Fe 2.97E3	Mg*P 2.29E5	Fe*Mg -8.57E4	Al*Fe -2.67E4	S 1.37E4	46.8	.9420	39.1	31.2
	S*Si -5.80E4	Al*K 7.69E4	Ca*Na -2.28E5	Ca*Fe 4.65E4	Al*Na 3.28E5				

Table 7

Best Regressions on Hemispherical Temperature

Intcpt.°F	Terms and Coefficients	SEI.°F	R^2	RMSE.°F	average error.°F
2,078	P*S -3.53E5, K*P 7.93E6, Na*P 2.77E6, Al*Na 6.21E4	25.2	.872	54.6	43.6
1,897	Ca*Si -5.35E3, P*S -4.80E5, K*Ti 1.09E6, Al*Ca 1.61E4, Na*P 4.75E6	69.3	.896	49.7	39.6
2,070	Ca*Si -4.41E3, P*S -1.09E5, Fe*S -3.62E4, K*P 1.29E6, Ca*Fe 4.14E4, Al*Na 1.18E5	25.8	.9127	45.9	36.6
2,195	Ca*Si -1.18E4, K*S 1.34E5, P*S -5.72E5, Fe*S -4.28E4, Ca*Fe 4.01E4, Al*Ca 1.46E4, Na*P 5.60E6	23.1	.9287	41.8	33.4
2,066	P 1.81E4, Ca*Si -1.16E4, P*S -3.61E5, Fe*S -3.04E4, K*Na 1.14E6, Ca*Fe 3.42E4, Al*Ca 1.73E4, Na*P 2.22E6	36.7	.9379	39.3	31.4
2,192	Fe 6.54E3, Ca*Si -1.11E4, Fe*Si -1.62E4, P*S -4.65E5, Fe*S -4.26E4, Al*K 5.33E4, Ca*Fe 3.34E4, Al*Ca 1.43E4, Na*P 4.55E6	66.2	.9446	37.5	29.9
2,256	P 9.71E5, Fe 4.53E3, Ca*Si -1.21E4, Fe*Si -1.16E4, P*S -3.88E5, Fe*S -4.82E4, K*Na 1.40E6, Ca*Fe 4.31E4, Al*Ca 1.22E4, Na*P 2.98E6	74.6	.9477	36.7	29.3

Table 8

Best Regressions on Fluid Temperature

Intcpt.°F	Terms and Coefficients	SEI.°F	R^2	RMSE.°F	average error.°F
2,185°F	S*Si -8.74E3, P*S -6.09E4, K*P 1.00E6, Al*Na 1.73E5	24.9	.892	53.1°F	42.3°F
2,171	Mg*P 9.97E4, S*Si -8.52E3, P*S -1.06E5, K*P 1.06E6, Al*Na 1.78E5	24.6	.9010	51.2	40.8
2,319	S*Si -1.88E4, K*P 6.33E5, Ca*Ti -1.11E5, Ca*Fe 3.30E4, Fe*Na -2.48E5, Al*Na 2.90E5	34.0	.9172	47.1	37.6
2,155	Mg*P 2.19E5, Fe*Mg -3.45E4, S*Si -1.29E4, P*S -1.39E5, K*P 9.50E5, Ca*Fe 1.27E4, Al*Na 2.40E5	23.2	.9266	44.8	35.7
2,203	Ti 6.66E4, Mg*P 2.33E5, Fe*Mg -3.91E4, S*Si -1.45E4, Si*Ti -1.40E5, P*S -2.05E5, K*P 1.10E6, Al*Na 2.44E5	55.3	.9313	43.7	34.8
2,204	Ti 5.02E4, Mg*P 2.35E5, Fe*Mg -4.41E4, S*Si -1.57E4, Si*Ti -1.10E5, P*S -1.89E5, K*P 1.11E6, Ca*Fe 7.83E3, Al*Na 2.57E5	54.1	.9355	42.7	34.0
2,283	Ti 6.36E4, Mg*P 2.35E5, Fe*Mg -5.13E4, S*Si -1.15E4, P*Si 5.66E4, Si*Ti -2.28E5, P*S -2.81E5, K*Na -2.01E6, K*Ti 2.21E6, Al*Na 3.14E5	79.9	.9391	41.8	33.3

Indicators of Multicollinearity in Softening Temperature Regressions

	10 terms[a]	20 terms[b]	30 terms[b]	55 terms
R^2 (uncorrected)	.942	.9547	.9667	.9770
rmse	39.1°F	37.9°F	36.4°F	50.5°F
	21.7 K	21.1 K	20.2 K	28.1 K
SEI	46.8°F	813°F	>2120°F	>21,000°F
	26.0 K	452 K	>1170 K	>11,600 K
Avg precision of first 10 coefficients[c]	15.8 %	159 %	272 %	>2,400 %
Avg instability of first 10 coefficients to a dummy variable[d]	0.01%	4.6 %	32.1%	400 %
Avg instability of first 10 coefficients to removal of 14 cases[e]	14.1 %	111 %	449 %	>1,500 %

[a] Best regression from Table 6.

[b] Selected by forward selection procedure.

[c] [S.E. of coefficient]/[coefficient] * 100%.

[d] Average shift in value of coefficients upon introduction of a random number variable (see text).

[e] Average shift in value of coefficients upon deletion of every fifth case in the dataset.
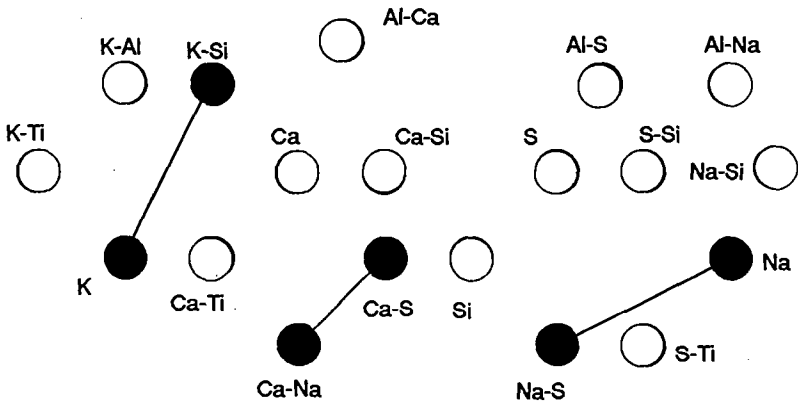
FIGURE 1

CORRELATIONS AMONG 19 TERMS

R(crit) = 0.98
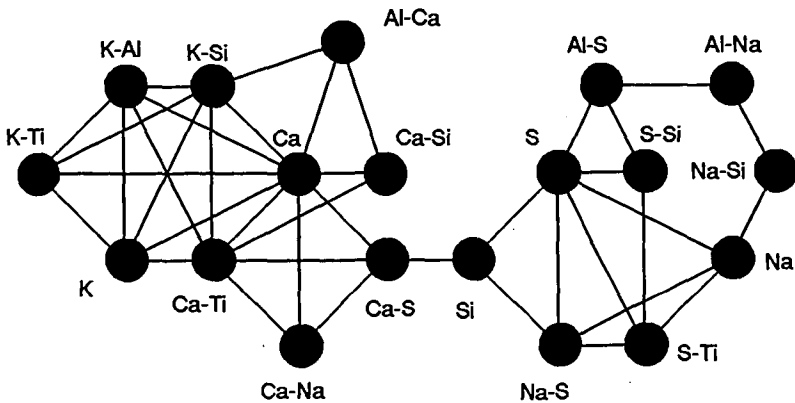
FIGURE 2

CORRELATIONS AMONG 19 TERMS

R(crit) = 0.90
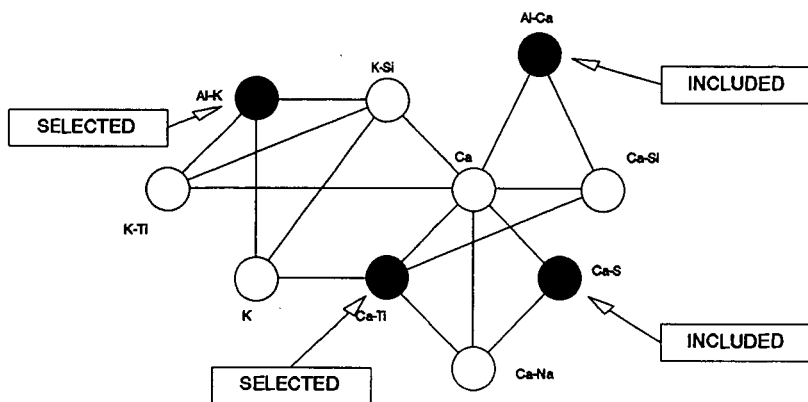
247

FIGURE 3
SELECTION TO AVOID COLLINEARITIES

FIGURE 4
ESTIMATE OF INITIAL DEFORMATION TEMP.
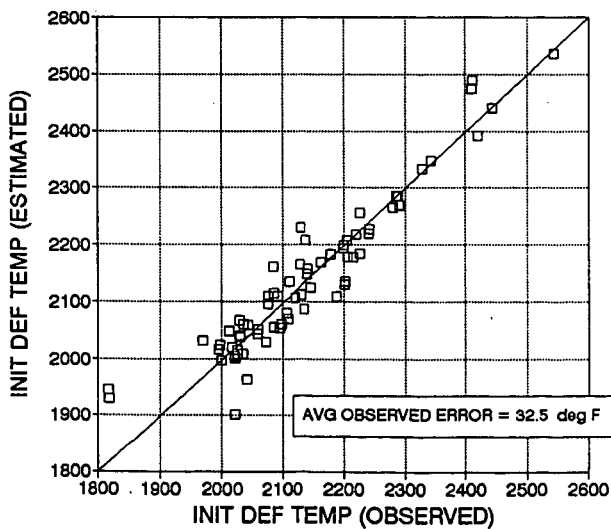### 70 CASES
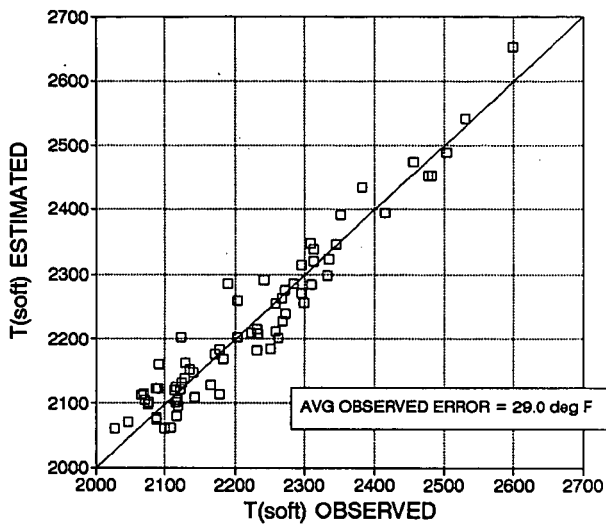
FIGURE 5
ESTIMATE OF SOFTENING TEMPERATURE
70 CASES

AVG OBSERVED ERROR = 29.0 deg F

FIGURE 6
ESTIMATE OF HEMISPHERICAL TEMPERATURE
70 CASES

AVG OBSERVED ERROR = 26.7 deg F
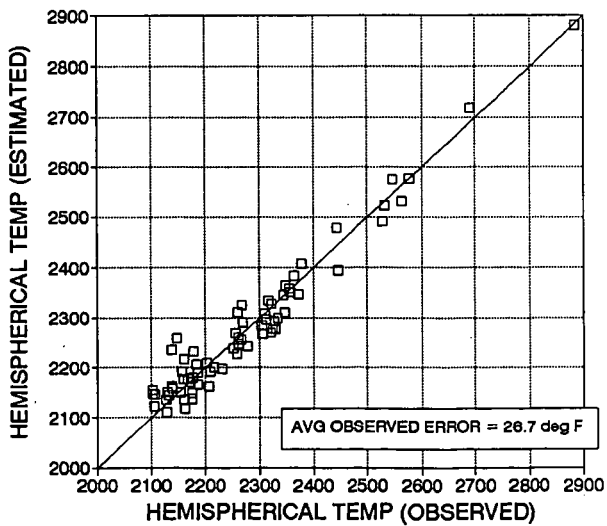
FIGURE 7
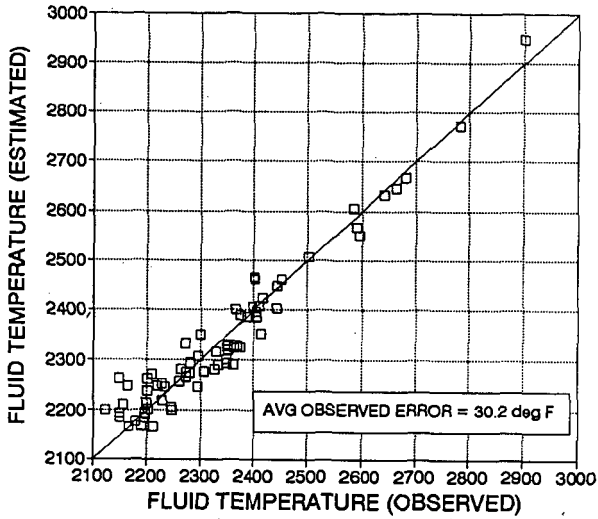
ESTIMATE OF FLUID TEMPERATURE
70 CASES

FIGURE 8

SOFTENING TEMPS OF 14 "NEW" ASHES
USING BEST SOFTENING TEMP REGRESSION

250 A